

FINAL REPORT

Air Force Office of Scientific Research
Contract No. FA-9550-04-1-0046

1 Nov 2003 - 14 Jun 2007

Advanced Technologies for Ultrahigh Resolution and Functional Optical Coherence Tomography

Principal Investigator

Prof. James G. Fujimoto
Department of Electrical Engineering and Computer Science
and Research Laboratory of Electronics
Massachusetts Institute of Technology
77 Massachusetts Avenue
Cambridge, MA 02139

| | | | | | |
|--|-------------|-----------------------|-----------------------------------|---|--|
| REPORT DOCUMENTATION PAGE | | | | <i>Form Approved OMB No. 0704-0188</i> | |
| <small>The public reporting burden for this collection of information is estimated to average 1 hour per response, including the time for reviewing instructions, searching existing data sources, gathering and maintaining the data needed, and completing and reviewing the collection of information. Send comments regarding this burden estimate or any other aspect of this collection of information, including suggestions for reducing the burden, to the Department of Defense, Executive Services and Communications Directorate (0704-0188). Respondents should be aware that notwithstanding any other provision of law, no person shall be subject to any penalty for failing to comply with a collection of information if it does not display a currently valid OMB control number.</small> | | | | | |
| PLEASE DO NOT RETURN YOUR FORM TO THE ABOVE ORGANIZATION. | | | | | |
| 1. REPORT DATE (DD-MM-YYYY) | | 2. REPORT TYPE | | 3. DATES COVERED (From - To) | |
| 4. TITLE AND SUBTITLE | | | | 5a. CONTRACT NUMBER | |
| | | | | 5b. GRANT NUMBER | |
| | | | | 5c. PROGRAM ELEMENT NUMBER | |
| 6. AUTHOR(S) | | | | 5d. PROJECT NUMBER | |
| | | | | 5e. TASK NUMBER | |
| | | | | 5f. WORK UNIT NUMBER | |
| 7. PERFORMING ORGANIZATION NAME(S) AND ADDRESS(ES) | | | | 8. PERFORMING ORGANIZATION REPORT NUMBER | |
| 9. SPONSORING/MONITORING AGENCY NAME(S) AND ADDRESS(ES) | | | | 10. SPONSOR/MONITOR'S ACRONYM(S) | |
| | | | | 11. SPONSOR/MONITOR'S REPORT NUMBER(S) | |
| 12. DISTRIBUTION/AVAILABILITY STATEMENT | | | | | |
| 13. SUPPLEMENTARY NOTES | | | | | |
| 14. ABSTRACT | | | | | |
| 15. SUBJECT TERMS | | | | | |
| 16. SECURITY CLASSIFICATION OF: | | | 17. LIMITATION OF ABSTRACT | 18. NUMBER OF PAGES | 19a. NAME OF RESPONSIBLE PERSON |
| a. REPORT | b. ABSTRACT | c. THIS PAGE | | | 19b. TELEPHONE NUMBER (Include area code) |

Air Force Office of Scientific Research

FINAL REPORT GRANT #: FA-9550-04-1-0046
P.I.: Dr. James G. Fujimoto
INSTITUTION: Massachusetts Institute of Technology
GRANT TITLE: Advanced Technologies for Ultrahigh Resolution
 and Functional Optical Coherence Tomography
AWARD PERIOD: 1 Nov 2003 - 14 Jun 2007

Objective of the Proposal

This program, entitled “Advanced Technologies for Structural and Functional Optical Coherence Tomography,” is a collaborative effort between investigators at the Massachusetts Institute of Technology, Department of Electrical Engineering and Computer Science and Research Laboratory of Electronics; Dr. David Boas, Associate Professor in Radiology, Harvard Medical School at the Massachusetts General Hospital, Martinos Center for Biomedical Imaging; and Dr. Jay Duker, Director, New England Eye Center, Professor and Chair of Ophthalmology, Tufts University School of Medicine. The objective of this program is to develop and apply advanced optical coherence tomography (OCT) technologies for ultrahigh resolution and functional imaging in biomedical applications.

Accomplishments

OCT is an emerging diagnostic imaging technology which was developed by our research group in part under this program during the 1990s. OCT generates cross-sectional images of tissue microstructure with micron scale (1-15 μm) resolution by measuring the echo time delay and magnitude of backscattered light. OCT can thus function as a type of “optical biopsy,” enabling imaging of tissue with resolution approaching conventional biopsy and histopathology, but in real time, without the need to remove and process specimens. During the past contract period, we have made significant progress in a number of areas: development of new laser technology for ultrahigh resolution, high-speed, and three-dimensional imaging; new technology and measurement techniques for functional OCT imaging in the retina and brain; in vitro imaging studies to establish the feasibility of using OCT and Optical Coherence Microscopy (OCM) for optical biopsy; and clinical studies in endoscopy and ophthalmology.

These key advances are summarized in sections entitled:

1. Optical coherence tomography (OCT) technology
2. Ophthalmic OCT
3. Endoscopic OCT studies
4. Optical Coherence Microscopy
5. Functional brain imaging with OCT

A list of publications supported under this contract is appended at the end.

1. Optical Coherence Tomography (OCT) technology

Optical coherence tomography (OCT) is an emerging imaging technology, developed by our research group and collaborators in 1991 [1]. OCT enables imaging of the cross sectional structure in biological tissues and materials by measuring the echo time delay of backscattered or backreflected light. OCT has applications in a wide range of clinical specialties [2]. OCT enables the visualization of tissue microstructure *in situ* and in real time with resolutions in the 1-10 μm range. The imaging depth of OCT in most tissues is 2-3 mm, determined by attenuation from optical scattering. OCT functions as a type of optical biopsy, enabling visualization of tissue structure without the need for excisional biopsy and histopathology [3-6].

OCT is based on low coherence interferometry and axial image resolutions are determined by the coherence length of the light source used for imaging. Clinical OCT systems often use superluminescent diodes (SLDs) that enable imaging with 10-15 μm axial resolution. These resolutions are typically insufficient for identifying neoplastic changes for cancer detection, or tissue morphological and structural features for the visualization of other pathologies. Advances in solid-state lasers and nonlinear fiber light sources have enabled the development of ultrahigh resolution and spectroscopic OCT techniques that promise to improve tissue differentiation and image contrast. Recent developments in new detection techniques based on Fourier domain detection (known as spectral OCT and swept source OCT) enable very high speed. These new techniques achieve dramatic advances in imaging speed which enable three dimensional imaging. Tissue microstructure can now be visualized and rendered using methods similar to MR imaging, except with micron scale resolution.

1.1 Ultrahigh resolution OCT

Conventional OCT imaging studies performed to date have used axial resolutions of 10-15 μm . Our group pioneered the development of ultrahigh-resolution OCT imaging, achieving axial resolutions $\sim 3 \mu\text{m}$ in the human eye and $\sim 1 \mu\text{m}$ in other applications [7-9]. The axial resolution in OCT depends on the coherence length of light and is inversely proportional to the optical bandwidth of the light source, $\lambda_0^2/\Delta\lambda$, where $\Delta\lambda$ is the bandwidth and λ_0 is the median wavelength. Ultrahigh resolution OCT continues to be an active field of research and is closely related to the development of broadband light sources [2, 10]. This is particularly the case for the spectral region between 1.0 μm and 1.5 μm . This spectral region is of great interest for OCT because optical scattering is decreased at longer wavelengths, enabling deeper image penetration depth in biological tissue. In addition, broadband light sources are essential for enabling spectroscopic OCT imaging of functional parameters such as water content and tissue oxygenation [11].

Superluminescent diode light sources are commonly used in OCT because of their compact size and low cost. However, traditional superluminescent diode light sources have limited bandwidths and axial image resolutions are typically $\sim 10 \mu\text{m}$. Femtosecond lasers are ideal light sources for ultrahigh resolution OCT because they can generate the extremely broad bandwidths necessary for ultrahigh resolution imaging. Previously, we demonstrated OCT imaging with resolutions of 1 μm at 800 nm and 5.1 μm at 1300 nm in biological tissue by using solid-state mode-locked

lasers as well as nonlinear fiber sources [8, 12, 13]. We have investigated compact, portable light sources for ultrahigh resolution OCT imaging at wavelengths of 890 nm, 1300 nm, and 1500 nm to enable more widespread ultrahigh resolution and spectroscopic OCT imaging to be performed in clinical settings. Recently, we demonstrated OCT imaging with $<5\ \mu\text{m}$ resolution in tissue at 1300 nm and $<3\ \mu\text{m}$ resolution at 800 nm using continuum generation in a single photonic crystal fiber with a parabolic dispersion profile and two closely spaced zero dispersion wavelengths [14].

1.1.1 Low-threshold Ti:Sapphire laser for Ultrahigh Resolution Ophthalmic Imaging

Kerr lens modelocked (KLM) $\text{Ti:Al}_2\text{O}_3$ lasers can generate extremely short pulse durations with broad bandwidths that are particularly useful in biomedical imaging [15]. A standard Kerr lens modelocked laser operating with a 5W pump can produce output powers of 500 mW and bandwidths in excess of 150 nm [16]. Unfortunately, the high cost of today's femtosecond lasers severely limits their widespread use. The cost of femtosecond $\text{Ti:Al}_2\text{O}_3$ lasers is strongly dependent on the pump power requirements. Diode pumped solid-state lasers capable of generating 5 W can be prohibitively expensive, while lasers generating several hundred mW are considerably more affordable.

We have developed a low-threshold, low-cost, compact laser technology. By replacing standard mirrors and prisms with 3rd generation double-chirped mirrors (DCMs), we developed a broadband, portable laser source which could be used in the clinical setting for ultrahigh resolution OCT imaging with $3\ \mu\text{m}$ axial resolution [17]. Figure 1.1 shows the spectrum and point spread function of the low-threshold source. Figure 1.2 shows a comparison between standard $10\ \mu\text{m}$ resolution (a) and ultrahigh $3\ \mu\text{m}$ resolution (b) OCT images of the normal human fovea. We developed a prototype ultrahigh resolution ophthalmic instrument which was used in the ophthalmology clinic at the New England Eye Center between 2002 and 2004 and performed studies on >1000 patients. These studies provided new insights into retinal pathologies, especially alterations in photoreceptor structure.

1.1.2 Broadband SLD for Ultrahigh Resolution Ophthalmic Imaging

While superluminescent diode sources have proven to be inexpensive and stable for use in a clinical setting, conventional SLD sources typically have limited bandwidths and output powers. Broadband SLD sources are made possible by multiplexing two or more diodes with different center wavelengths. These sources are more inexpensive and user-friendly than Ti:Sapphire sources but have lower output powers. For applications where light exposure levels are limited by safety considerations, such as retinal imaging, broadband SLD sources provide sufficient power levels for OCT imaging.

Recently, our group and others have demonstrated ophthalmic retinal imaging with broadband SLD light sources [18, 19]. These studies were performed in collaboration with investigators at Superlum Diodes, Ltd. and used a new prototype which consisted of two spectrally multiplexed, independently driven SLD diodes operating at 840 nm and 920 nm, respectively. Figure 1.3 shows individual (a) and combined (b) SLD spectra, along with the point spread function on a

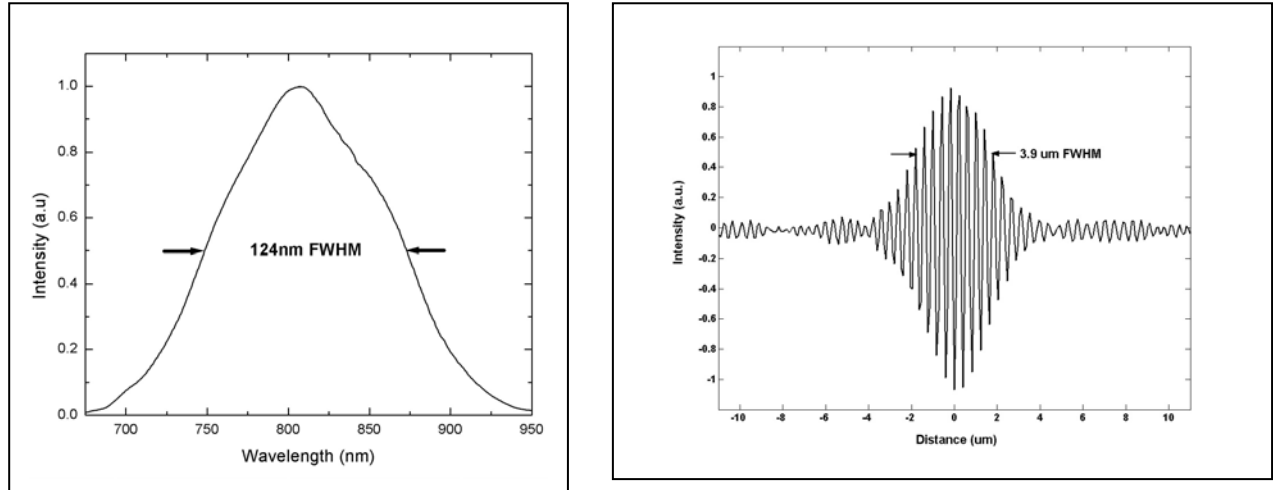


Figure 1.1. Spectrum and point spread function of the low-threshold Ti:Sapphire laser developed by our group for OCT imaging in the ophthalmology clinic.

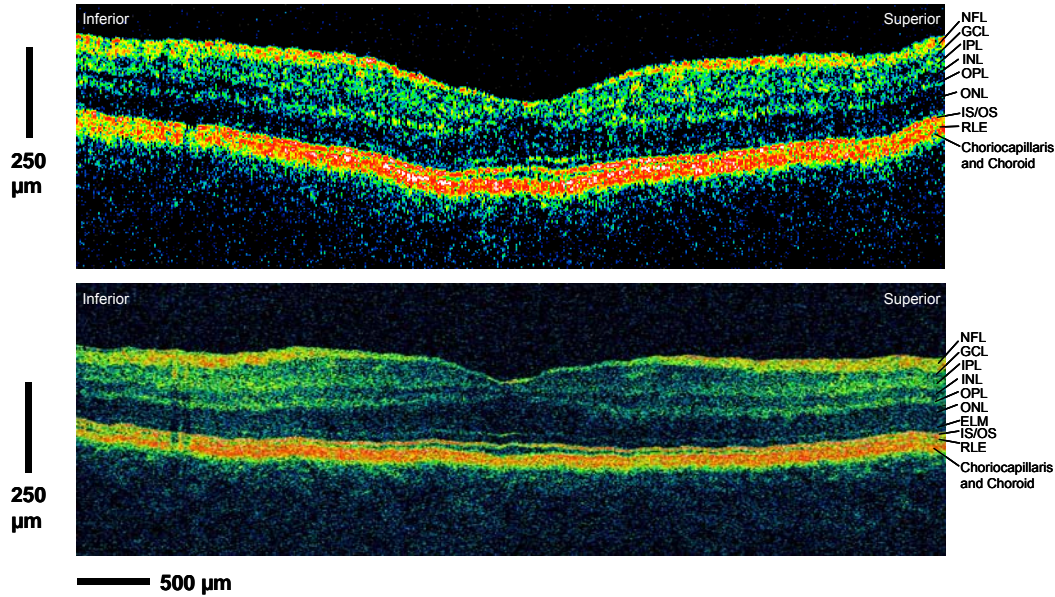


Figure 1.2. *In vivo* standard resolution OCT from the Zeiss Stratus instrument (top) and ultrahigh resolution OCT images (bottom) of a normal human fovea at approximately the same site. Resolutions were $\sim 10\text{-}15\text{ }\mu\text{m}$ axial $\times 15\text{ }\mu\text{m}$ transverse (top) and $\sim 3\text{ }\mu\text{m}$ axial $\times 15\text{ }\mu\text{m}$ transverse (bottom) respectively.

linear (c) and logarithmic (d) scale. An SLD diode based on a SQW (GaAl)As heterostructure [20] and a second recently-developed SLD diode based on a SQW (InGa)As/(AlGa)As heterostructure with graded-index waveguides [21] were used. The combined SLD output provides 155 nm of bandwidth at a center wavelength of 890 nm with $>4\text{ mW}$ of CW output power. Compared to a solid-state laser, this broadband SLD source is quite compact and has a total footprint of only 31 x 26 x 15 cm including the power supply, or 31 x 15 x 5 cm for the SLD and multiplexer package alone. The total cost of this light source is about an order of

magnitude less than that of a typical commercial Ti:Sapphire femtosecond laser. An image of the normal human macula taken with the Broadlighter source is shown in Figure 1.4. These results were significant because they enable wider spread access to ultrahigh resolution OCT for research and clinical applications.

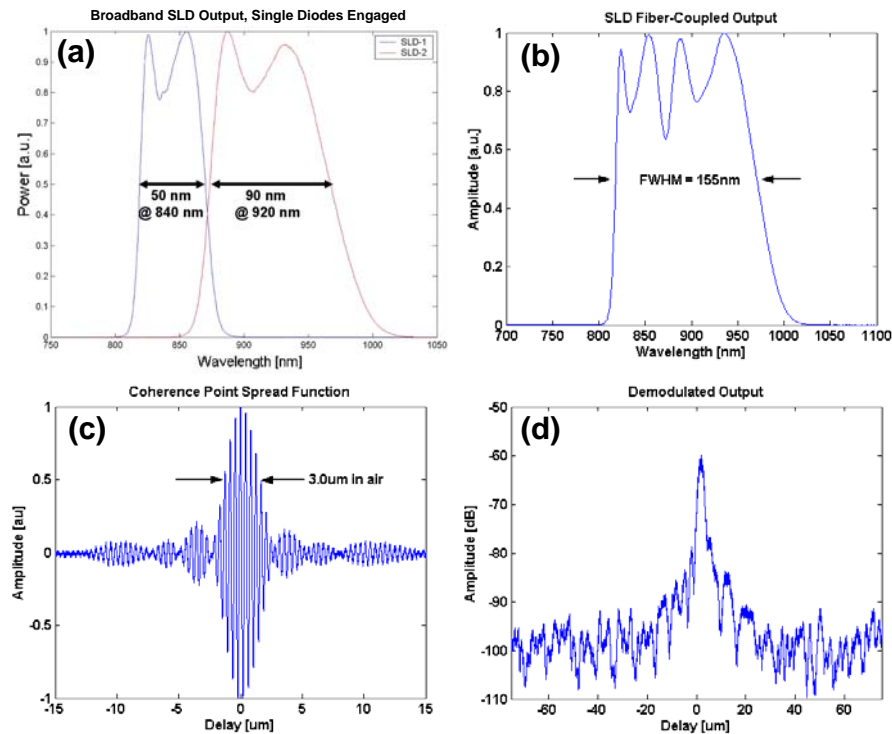


Figure 1.3. (a) Individual output spectra of the two superluminescent diodes. (b) Fiber-coupled multiplexed spectrum of the broadband SLD source. (c) Coherence point spread function of the broadband SLD source. (d) Logarithmic demodulated coherence point spread function.

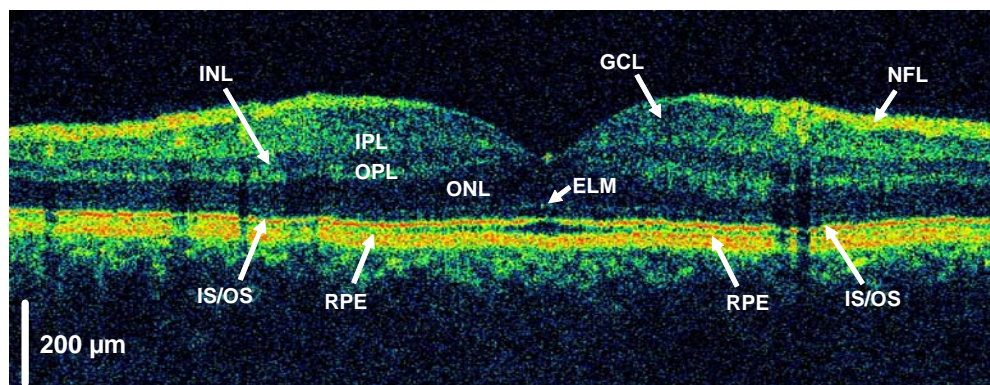


Figure 1.4. *In vivo* ultrahigh resolution OCT image of the human retina taken with a broadband SLD light source. The axial image resolution in the retina was about 3.2 μm . All the major intraretinal layers can be clearly seen in this ultrahigh resolution OCT image.

1.1.3 Cr:Forsterite for Endoscopic Imaging

Epithelial cancers of the gastrointestinal tract, reproductive tract, and the respiratory tract comprise the majority of cancers encountered in internal medicine. Many epithelial cancers are preceded by pre-malignant changes, such as dysplasia. Conventional screening methods often rely on the gross morphological characteristics of tissues. Biopsy and histopathology is the standard for the diagnosis of dysplasia or carcinoma, but can suffer from sampling errors and is cumbersome for screening and surveillance applications. OCT can function as a form of “optical biopsy” which can perform microstructural imaging of tissue morphology *in situ* without excision. The aim of this work was to perform imaging of architectural morphology of the human upper gastrointestinal tract to explore the feasibility of ultrahigh resolution OCT for the identification of morphologies characteristic of early neoplastic changes.

Working in collaboration with Prof. Franz Kaertner, at M.I.T., we developed a compact, femtosecond Cr⁴⁺:Forsterite laser combined with a nonlinear fiber in order to generate a spectral bandwidth greater than 200 nm at a center wavelength of 1250 nm. The Cr⁴⁺:Forsterite laser was similar to our previous systems [22, 23]; however, it used broadband, double-chirped mirrors [24] to compensate intra-cavity dispersion and achieve a compact, prism-less laser design. A compact Yb fiber laser was used as the pump source. Figure 1.5(a) shows the optical spectrum generated by the Cr:Forsterite laser and nonlinear fiber. The bandwidth is 210 nm FWHM. Due to bandwidth limitations in the optical circulator, shorter wavelengths were attenuated and the transmitted spectrum was reduced to 150 nm bandwidth (also shown). The measured axial point spread function shown in Figure 1.5(b) has a resolution of 5 μm in air, close to the calculated theoretical value of 4.6 μm for this transmitted bandwidth. This corresponds to an axial resolution of ~ 3.7 μm in tissue, assuming an index of refraction of ~ 1.37 , and is a three-fold improvement in resolution when compared to previous endoscopic OCT systems. The system detection sensitivity was measured to be 102 dB with 10 mW of incident power.

Previous research suggests that OCT can image features of architectural morphology which are relevant for the diagnosis and monitoring of early neoplastic tissue changes. We have performed *in vitro* surveys imaging and histopathologic correlations of normal as well as abnormal human tissue pathologies including Barrett’s esophagus, adenocarcinoma of the esophagus, ulcerative colitis, colonic dysplasia, adenomatous polyps, colorectal carcinoma, cervical intraepithelial neoplasia, cervical carcinoma, uterine dysplasia, and endometrial carcinoma in order to evaluate the ability of OCT to differentiate early neoplastic changes and other tissue abnormalities with a predisposition to malignancy. In order to validate this new technology for ultrahigh resolution endoscopic imaging we performed an *in vivo* imaging study in a rabbit animal model [25], as shown in Figure 1.6. Endoscopic OCT imaging was performed on the gastrointestinal, urinary, reproductive, and respiratory tracts and correlated with histology. We also have performed endoscopic imaging of patients with Barrett’s esophagus.

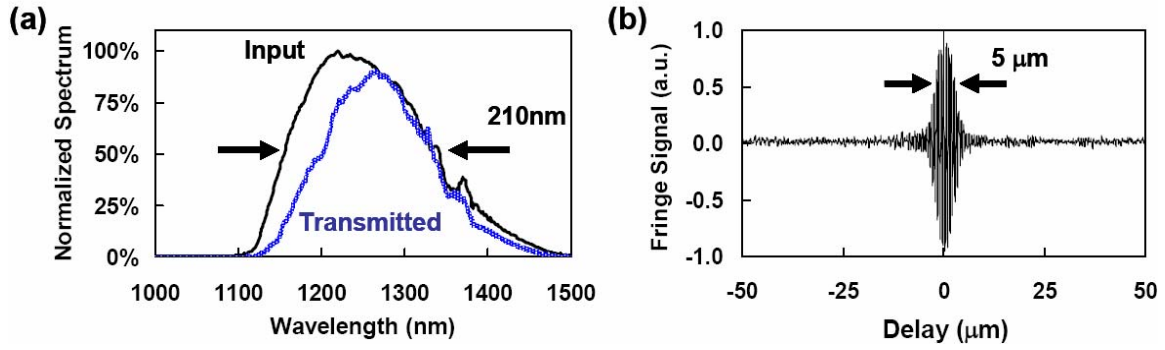


Figure 1.5. Cr⁴⁺:Forsterite laser for ultrahigh resolution OCT at 1300 nm. (a) Optical spectrum with 210 nm FWHM generated by the Cr⁴⁺:Forsterite laser and self phase modulation in a nonlinear fiber. Due to bandwidth limitations in the optical circulator, the transmitted spectrum was reduced to 150 nm bandwidth (also shown). (b) The measured axial point spread function has a resolution of 5 μm in air, close to the calculated theoretical value of 4.6 μm for the transmitted bandwidth.

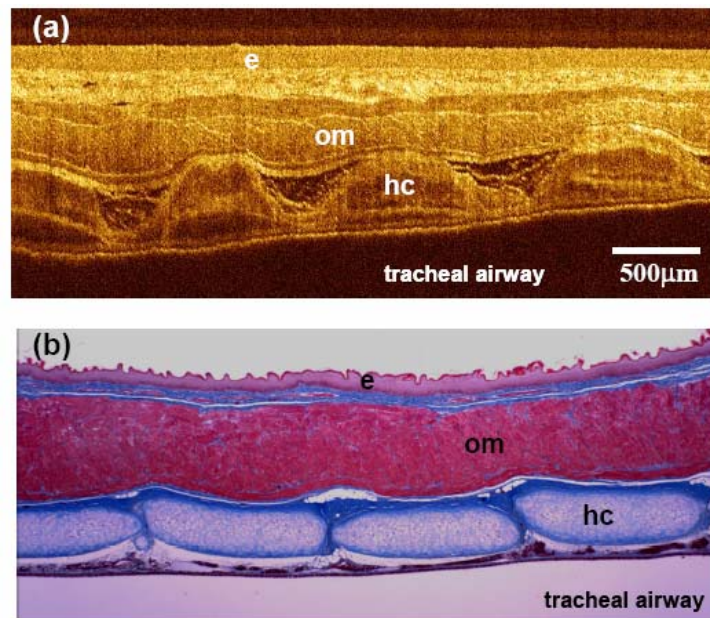


Figure 1.6. (a) *In vivo* OCT image and (b) histology of rabbit esophagus and trachea viewed intraluminally from the esophagus. Tracheal hyaline cartilage (hc) between the tracheal mucosa and trachealis muscle is well defined. The image demonstrates the ability of the endoscopic OCT system to image deeply within the tissue. Trichrome stain was used to highlight cartilage and muscle layers.

1.1.4 All-Fiber Continuous-Wave Raman Continuum Light Source

Working in collaboration with investigators from the Imperial College in London, we demonstrate a new, high performance light source for ultrahigh resolution OCT [26]. Bandwidths of 140 nm at 1300 nm center wavelength with high output powers of 330 mW were generated by an all-fiber Raman light source based on a continuous-wave Yb-fiber laser-pumped microstructure fiber. The schematic of the light source and output bandwidth are shown in Figure 1.7. The light source is compact, robust, turnkey and requires no optical alignment. In vivo, ultrahigh resolution, high-speed, time domain OCT imaging with $<5\ \mu\text{m}$ axial resolution is possible using a high-power, continuous-wave, all-fiber pump light source.

Microstructure fibers typically have been pumped with femtosecond lasers to provide the peak powers necessary to initiate nonlinear effects for continuum generation under conditions of anomalous or near-zero dispersion. However, these light sources can have spectral modulation and excess intensity noise [27]. An alternative to using high peak powers is to increase the effective nonlinear interaction length of the Raman interaction, which is governed by optical losses in the fiber and dispersive walk-off between the pump and continuum pulses. Stimulated Raman scattering has been shown to be the principle nonlinearity for continuum generation by using nanosecond-scale pump pulses [28]. Recently, the possibility of low peak power and even continuous-wave, multiwatt Raman continuum generation in highly nonlinear fibers has been demonstrated [29]. Continuous-wave pumping of nonlinear fibers can enable the development of robust and turnkey continuum light sources which require no optical alignment, enabling high-speed, ultrahigh resolution OCT imaging in a wide range of applications outside the laboratory.

The axial resolution of $<5\ \mu\text{m}$ is comparable to that achieved using much more complex femtosecond solid state sources such as the Cr:Forsterite laser. Output powers are comparable to or better than those available from femtosecond lasers, and more than one order of magnitude higher than superluminescent diode sources. Since this light source is all-fiber, it requires no alignment and provides completely turnkey operation. The source is extremely compact, measuring only 25 x 25 x 20 cm, and can easily be integrated into portable OCT systems. Excess noise is relatively high, but can be reduced using dual-balanced detection. Further reduction in noise should be possible by reducing parasitic feedback effects in the fiber splices and by techniques such as active seeding of the Raman process. Broader output bandwidths should be achievable using higher pump power Yb-fiber lasers and different fiber geometries. The bandwidth will ultimately be limited by the water absorption of microstructure fibers which reduces the effective interaction length of the Raman scattering. Rendering and segmentation of sweat ducts in the human fingerpad are shown in Figure 1.8.

The current cost of the source is still relatively high due to the cost of the microstructure fiber. However, since demand for microstructure fiber is increasing, the price of these fibers is decreasing and can be expected to approach that of other specialty fibers. The cost of continuous-wave Yb-fiber lasers has also dramatically decreased in recent years. The cost of fiber Raman continuum light sources will therefore be significantly lower than that of bulk solid-state femtosecond laser-based light sources. The high performance and ease of use of the fiber Raman continuum source promises to enable a wide range of new ultrahigh resolution, high-speed, OCT imaging applications.

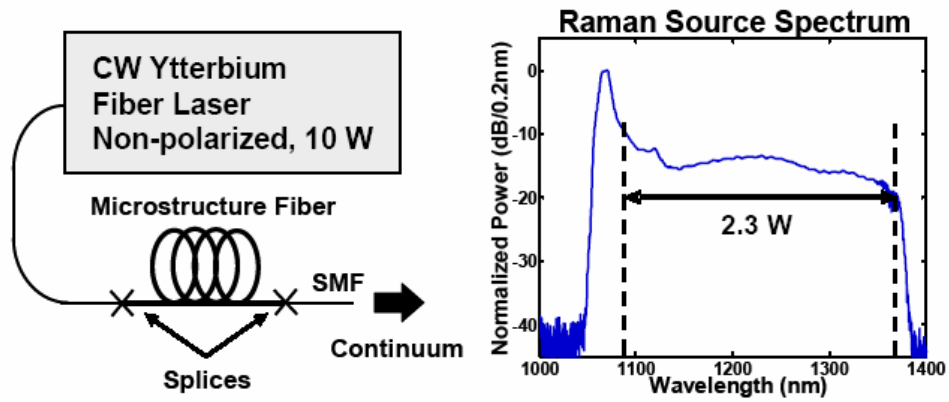


Figure 1.7. Left: Schematic of Raman continuum light source. SMF: Single-mode fiber. Right: Output spectrum. The output was 5.5W total, with 2.3 W in the spectral range from 1090 to 1370 nm. The output was filtered using a special WDM coupler to remove the pump wavelength and shape the spectrum.

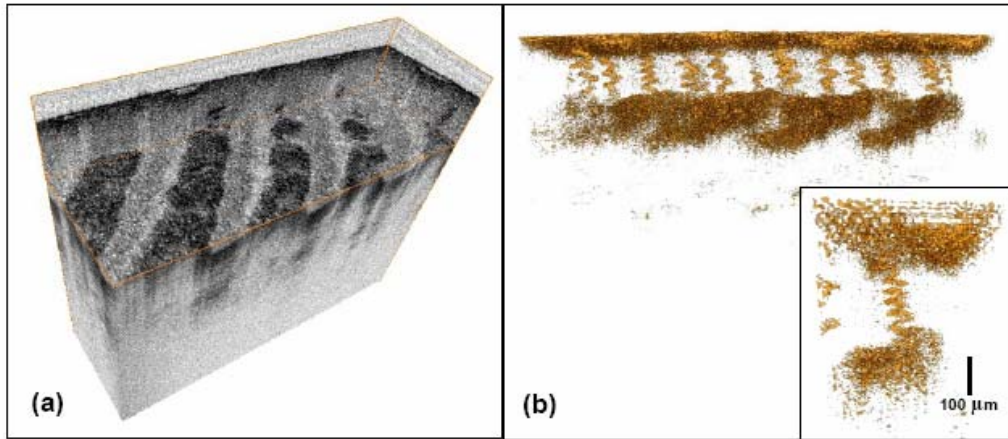


Figure 1.8. (a) Rendering showing *en face* slice of human fingerpad created from cross-sectional images. Spiraling sweat ducts are seen along the fingerpad ridges (2.25 x 0.75 x 1.8 mm). (b) 3D rendering and segmentation of sweat ducts. Duct density as well as individual ducts can be assessed.

1.1.5 Femtosecond Nd:Glass Laser Light Source

High nonlinearity, air-silica microstructure fibers or tapered fibers can generate a broadband continuum that spans the visible to the near infrared using femtosecond pulses. These fibers have enhanced nonlinearity because of dispersion characteristics of these fibers, which shift the zero dispersion to shorter wavelengths, and the small core diameters, which provide tight mode confinement. High numerical aperture fibers also have been used with femtosecond Ti:Sapphire lasers to achieve bandwidths of up to 200 nm [30]. Continuum generation from a femtosecond Ti:Sapphire laser with air-silica microstructured photonic crystal fibers was demonstrated to achieve OCT image resolutions of 2.5 μm in the spectral region 1.2 μm to 1.5 μm [13], resolutions of 1.3 μm in the spectral region 800 nm to 1400 nm, [31] and resolution <1 μm in the spectral region of 550 nm to 950 nm [32]. While high resolution imaging was demonstrated, femtosecond Ti:Sapphire lasers are generally expensive and bulky.

In this study, we demonstrated ultrahigh resolution, real time OCT imaging using a commercially available, compact femtosecond Nd:Glass laser that is spectrally broadened in a high numerical aperture single mode fiber [33]. Ultrahigh resolution, high speed OCT imaging was demonstrated at 1 μm center wavelength with <5 μm axial resolution in free space (or ~ 4 μm in tissue) and 93 dB sensitivity. Figure 1.9 shows the spectrum (a) and point spread function (b). This system is compact and well suited for *in vivo* ultrahigh resolution OCT imaging studies. The 1 μm wavelength is important because it has improved image penetration depths when compared to 800 nm and ultrahigh resolution imaging requires less bandwidth than at 1.3 μm wavelengths [34]. Figure 1.10 shows ultrahigh resolution images of the hamster cheek pouch with the Nd:Glass laser as the light source.

1.1.6 All-Fiber Femtosecond Fiber Laser Continuum Generation

The wavelength region around 1.4-1.6 μm is of interest for the characterization of optical devices or spectroscopic OCT applications measuring water absorption. We investigated the use of femtosecond fiber lasers for real-time, high-resolution OCT imaging in the 1.4-1.7 μm wavelength region [35]. The femtosecond fiber laser used a ring cavity with an Er fiber gain medium and passive modelocking using nonlinear polarization rotation as shown in Figure 1.11. A low-noise supercontinuum with 38 mW of power and a 180-nm bandwidth is generated by use of a high-power, stretched-pulse, passively mode-locked fiber laser and highly nonlinear fiber. The spectrum of the fiber laser and the high-nonlinearity fiber are shown in Figure 1.12. Figure 1.12 also shows the results of imaging human skin. *In vivo* imaging of human skin is demonstrated with the supercontinuum source and a high-speed OCT system. The measured axial resolution was 7.4 μm full-width-at-half-maximum (FWHM) in air, which corresponds to 5.6 μm in tissue. This light source is stable, compact, and self-starting and should be useful for a wide range of ultrahigh resolution, high-speed OCT imaging applications.

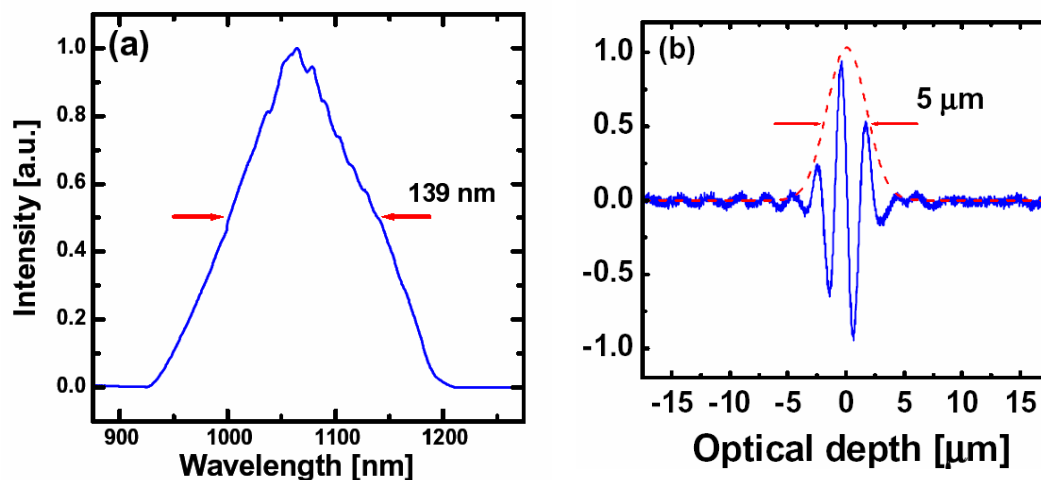


Figure 1.9. (a) Spectrum of the femtosecond Nd:Glass laser output broadened in the high numerical aperture (NA) single mode fiber. (b) Axial point spread function.

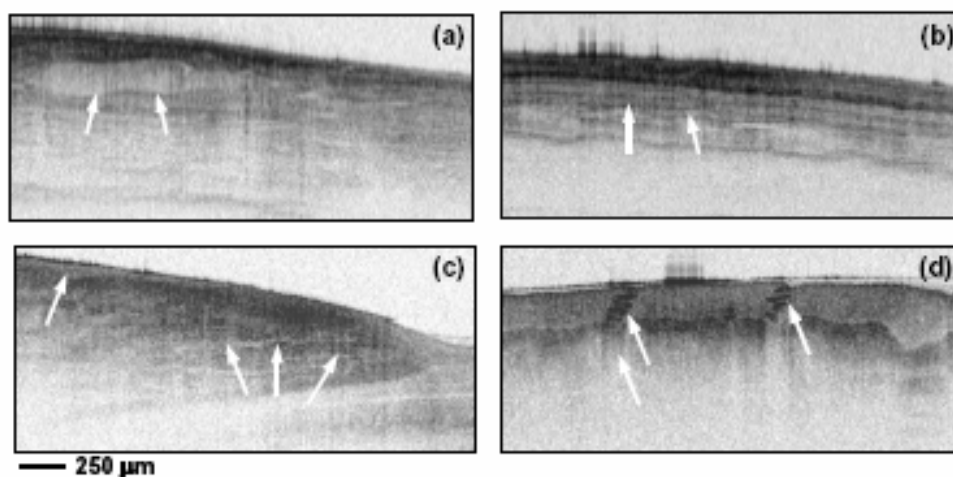


Figure 1.10. *In vivo* ultrahigh resolution OCT images at 1 μm wavelength. Images were acquired at 4 frames per second and are 2.5 mm x 1.2 mm with 11 μm x 4 μm (transverse x axial) resolution. (a, b) OCT of the hamster cheek pouch showing squamous epithelium, connective tissue and a junction between two vessels. (c) Image of the nail bed showing the stratum corneum and the junction between the epidermis and the dermis. (d) Image of human volar finger pad showing stratum corneum and sweat ducts.

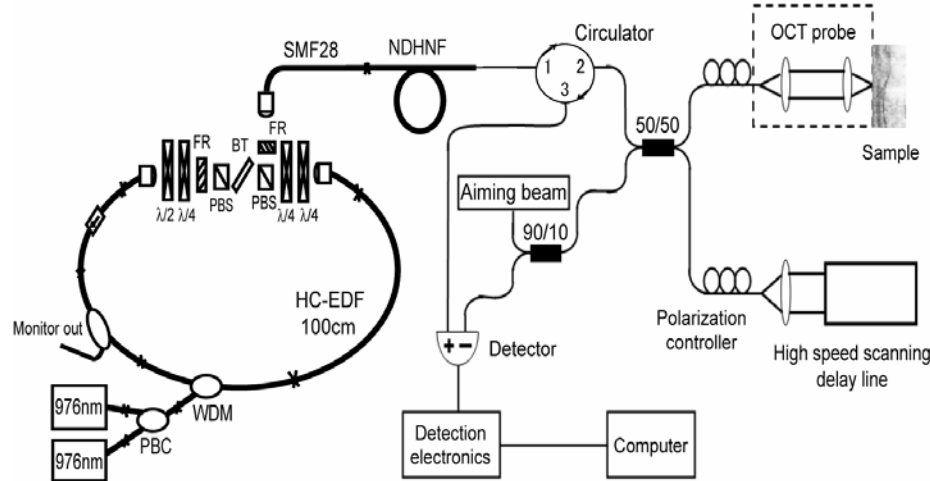


Figure 1.11. Fiber laser and nonlinear fiber for continuum generation in the 1500 nm region. The laser uses diode pumped Er doped fiber as the gain and is passively modelocked using nonlinear polarization rotation. Broadband continuum is generated in a nonlinear fiber.

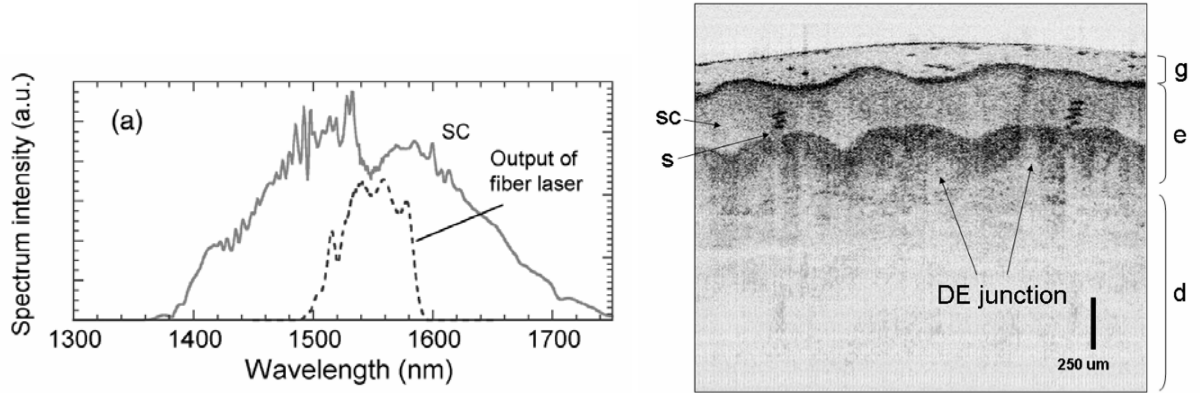


Figure 1.12. (left) Output spectrum from the fiber laser and the supercontinuum generated in a high-nonlinearity fiber. The bandwidth can be broadened from 70 to 180 nm. (right) High-speed *in vivo* OCT image of human skin. The top surface is a transparent index matching gel (g). The stratum corneum (sc), epidermis (e), sweat duct (s), and dermis (d) are clearly visible.

1.2 High speed OCT using Fourier domain detection

Conventional OCT systems perform measurements of backscattered or backreflected light by using an interferometer with a mechanically scanned optical reference path [1, 36, 37]. This means that light echoes with sequentially different delays are detected at different times as this reference path length is scanned. Hence, these systems are known as “time domain” systems. Recently, novel Fourier domain OCT detection techniques have emerged which do not require mechanical scanning and achieve very high detection sensitivities enabling OCT imaging with a

~15 to 50x increase in imaging speed over standard resolution OCT systems and ~100x over conventional ultrahigh resolution OCT systems. These Fourier domain techniques measure the echo time delay of light by Fourier transforming the interference spectrum of the light signal [38, 39]. Different echo time delays of light produce different frequencies of fringes in the interference spectrum. Fourier domain detection offers significantly improved sensitivity and imaging speed compared to time domain OCT [40-42]. Fourier domain detection can be performed in two ways: spectral OCT using broadband light source and a spectrometer with a linescan camera [38, 39, 43-45] or swept source OCT using a rapidly tunable, narrow linewidth laser source [1, 46-49].

Spectral and swept source Fourier domain OCT are especially promising for ultrahigh resolution ophthalmic imaging because they overcome imaging speed limitations of time domain OCT. Therefore, it is possible to use these techniques to acquire three-dimensional maps of the macula and optic disk [45, 50]. This also enables cross-registration of three-dimensional data sets with fundus photographs of the retina, for more accurate diagnosis of disease and evaluation of treatment. In addition, Fourier domain OCT has the advantage of providing direct access to the spectral fringe pattern, enabling a wide range of novel applications. Fourier domain OCT can be used for absorption measurement [51], Doppler techniques can be used to image blood flow [52, 53], and the complex Fourier domain signal can be directly measured to double the axial measurement scan range [54, 55].

1.2.1 Spectral domain OCT

Spectral domain detection techniques measure the echo time delay of light by using an interferometer with a broadband light source and measuring the spectrum of the interferometer output [40, 43, 51, 54, 56]. Backreflections or backscattering from the tissue at different delays produces oscillations or fringes in the interference spectrum. Increasing delay differences produce higher frequency oscillations. The magnitude and delay of the light from the tissue can be measured by Fourier transforming the interference spectrum. Spectral domain detection has a sensitivity advantage proportional to the number of resolvable elements in an axial scan. This sensitivity advantage is typically ~20-30 dB, enabling dramatic increases in imaging speeds [40-42, 44, 57]. With shorter exposure times, spectral domain OCT is less sensitive to subject motion than conventional time domain OCT.

We designed and constructed a portable, high-speed, ultrahigh resolution spectral OCT system which can achieve axial image resolution of ~3 μm for imaging in the ophthalmology clinic. This high-speed UHR-OCT prototype can be operated using either a femtosecond laser or a broadband superluminescent SLD as imaging light source. In our early studies, we developed a low threshold femtosecond Ti:Sapphire laser which was used in the ophthalmology clinic for three years. However, recent advances in multiplexed SLD light sources enable image resolutions of 3.5 μm . These broadband multiplexed SLDs provide an easy to operate and relatively inexpensive light source for clinical UHR-OCT imaging. The combination of high image acquisition speed and ultrahigh OCT axial resolution yields significant improvements in the clinical utility of high-speed ultrahigh resolution OCT systems over currently available prototype and commercial OCT systems.

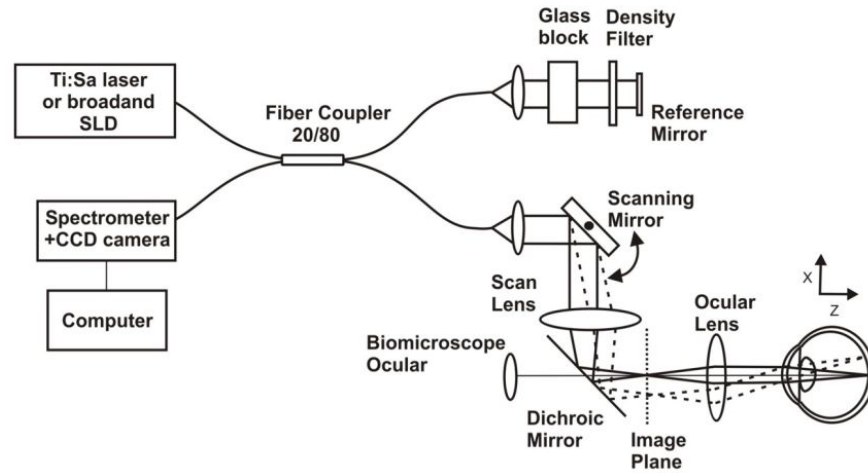


Figure 1.13. Schematic diagram of high speed ophthalmic OCT instrument using Fourier spectral domain detection. The system uses a broadband light source with an interferometer and a spectrometer. The interference spectrum is detected and Fourier transformed to obtain axial scan information.

Figure 1.13 shows a schematic of the high-speed, UHR-OCT ophthalmic system using spectral/Fourier domain detection [45]. Light from a broadband light source is split between the sample and reference arms of an interferometer. Light in the reference arm is attenuated and reflected from a stationary mirror at a fixed delay. Light in the sample arm is directed through two galvanometer-actuated steering mirrors and relay imaged through the pupil onto the retina [37]. The galvanometer actuated mirrors can scan the OCT beam across the retina in any arbitrary pattern in order to perform cross-sectional imaging. OCT image data is acquired by scanning the OCT beam on the retina under computer control. The incident light power on the eye is $750\ \mu\text{W}$, the same exposure used in commercial ophthalmic OCT systems and consistent with ANSI safety standards. The spectrum of the interferometer output is detected using a spectrometer consisting of a collimating lens, transmission grating, imaging lens, and CCD line scan camera. The interference spectrum data from the camera was transferred to computer system memory where it was rescaled from wavelength to frequency and Fourier transformed to generate axial measurements of the echo delay and magnitude of light from the retina. An example of clinical imaging using the high speed, ultrahigh resolution OCT instrument with spectral detection is shown in Figure 1.14.

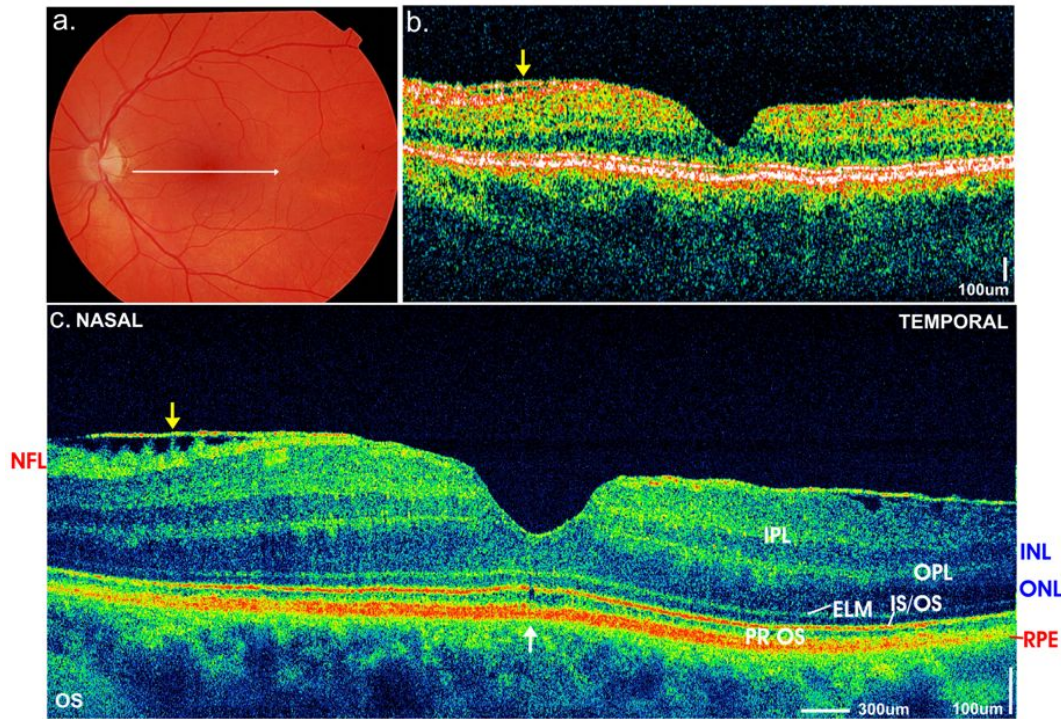


Figure 1.14. Macular hole repair: fundus photo (left top), cross-sectional image obtained by commercial instrument. Zeiss Stratus OCT (top right), cross-sectional image obtained by high speed, ultrahigh resolution OCT instrument. The high quality image consists of 8100 axial scans (transverse pixels) with 1024 points (axial pixels) per scan and was measured in 0.35 sec. NFL nerve fiber layer, IPL inner plexiform layer, INL inner nuclear layer, OPL outer plexiform layer, ONL – outer nuclear layer, ELM external limiting membrane, IS/OS inner/outer photoreceptor junction, PR OS photoreceptor outer segments, RPE retinal pigment epithelium.

Figure 1.14 shows a comparison of standard resolution (10 µm resolution image from the commercial Zeiss StratusOCT instrument) and high speed, ultrahigh resolution (from our research prototype instrument) images from a 65-year-old woman two years after the surgical repair of a full-thickness macular hole in her left eye. Visual acuity had improved to 20/25 OS. Both the standard resolution StratusOCT image (Fig 1.2b) and the high-definition, 8192 axial scan, ultrahigh resolution OCT image (Fig 1.2c) depict an epiretinal membrane (yellow arrows). However, the high-definition, ultrahigh resolution OCT image enables better visualization of the membrane thickness and separation from the retina in the nasal portion of the image. A very small central disruption of the photoreceptor IS/OS junction and foveal photoreceptor outer segments is visualized in the high-definition ultrahigh resolution OCT image (white arrow). No such disruption is apparent in the standard resolution OCT image. This abnormality in the photoreceptor signal, along with the epiretinal membrane, may explain the patient's slight decrease in visual acuity. Small photoreceptor disruptions visualized by OCT following macular hole repair have been reported previously, and may be correlated with visual acuity.

1.2.2 Swept Source OCT imaging

Although spectral/Fourier domain OCT systems can provide nearly optimal performance in low-scattering organs such as the eye, these systems are not well suited for imaging scattering tissues. Imaging epithelial tissues is of great interest since the majority of human cancers originate in epithelium that lines hollow organs such as the colon, esophagus, and breast ducts. In epithelial tissue, the high density of cellular organelles such as mitochondria, nuclei, and cellular membranes results in a highly scattering medium that limits the penetration depth of light at 800 nm wavelengths. Similarly, non-biological objects such as art samples also exhibit high optical scattering at short wavelengths. Since spectral/Fourier domain OCT systems typically employ silicon-based CCD detectors, they cannot operate at wavelengths longer than ~ 1000 nm. For OCT imaging of scattering tissues and many non-biological samples, however, operation at wavelengths of 1000 – 1300 nm is desired to reduce scattering and achieve deeper image penetration depths.

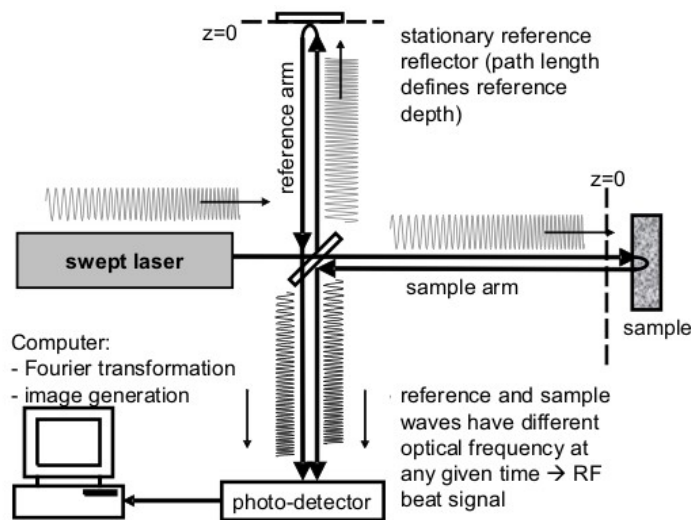


Figure 1.15 Schematic of how swept-source OCT operates. An RF beat signal is generated by interference between a sample beam and a reference beam. Optical distances within the sample are encoded into the RF beat frequencies.

Fourier domain detection approach using frequency swept lasers provides a powerful, complementary approach for spectral / Fourier domain detection using spectrometers and line scan cameras. Swept source OCT systems typically employ a broadband, frequency-swept laser source and InGaAs photodetectors to perform OCT imaging without the use of a spectrometer [41, 49, 58-64]. Figure 1.15 illustrates the concept of swept source OCT imaging using a frequency-swept laser and a Michelson interferometer. The frequency swept source light is split by a beamsplitter into reference and signal beams. One beam travels a fixed distance and reflects off of a reference mirror. The other beam strikes the sample of interest, where it is backscattered from structures at various depths. Each backscattering event produces an attenuated, time-delayed copy of the incident frequency sweep, which interferes with the reference beam. This interference is measured as a function of time using a high speed photodetector. A computer digitizes the interference fringes from the detector and performs a Fourier transformation to generate an axial scan in the OCT image.

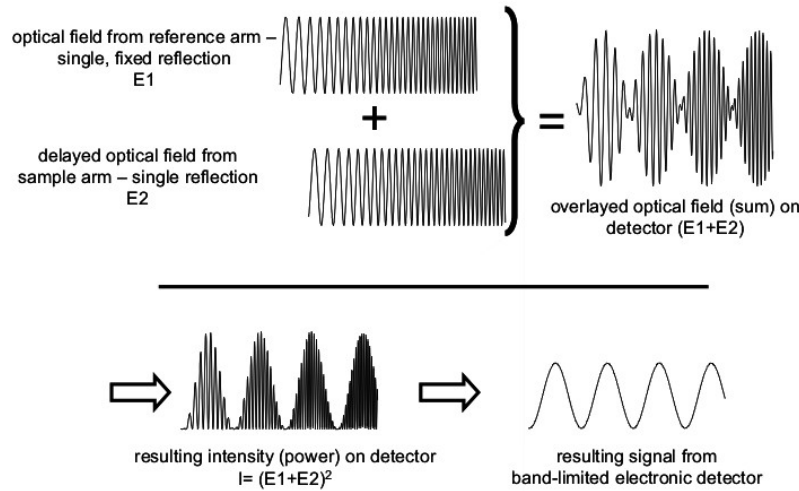


Figure 1.16. RF beat signal formation using a frequency-swept source for OCT imaging. The detector outputs only the RF modulation, which is correlated to the delay between the sample and reference beams.

As shown in Figure 1.16, the resulting interference fringes contain RF beat frequencies that correspond to the depth of each backscattering signal. For a single reflection in the sample arm, a single-frequency RF modulation will be created where the modulation frequency is directly proportional to the delay between the sample and reference beams. For a real material or biological sample, each of the numerous backscattering signals creates a unique RF modulation frequency. After Fourier transformation of the RF beat signal, a single axial scan line of an OCT image is formed.

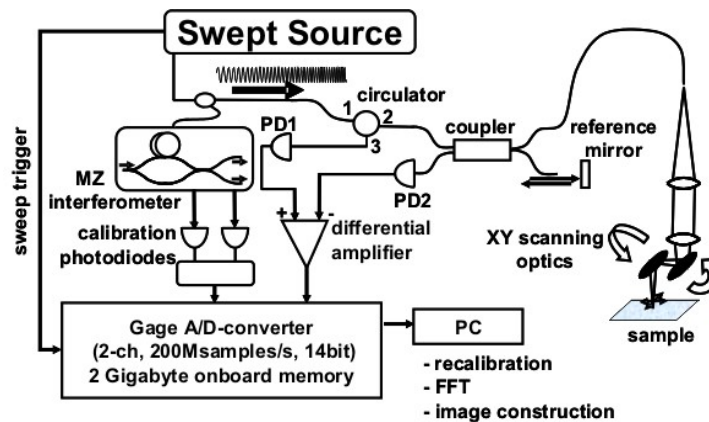


Figure 1.17. High-efficiency, dual-balanced, fiberoptic Michelson interferometer used for swept source OCT imaging.

In practice, a fiberoptic Michelson interferometer is used for OCT imaging. Figure 1.17 illustrates a typical imaging setup specific to swept source OCT systems. A small portion (~5%) of the laser output is tapped off and routed to a Mach-Zehnder interferometer, which is used for determining the instantaneous frequency of the sweep. This is necessary for resampling the OCT

interference fringes onto a uniformly-spaced frequency grid prior to Fourier transformation, since swept laser sources do not typically produce linear frequency sweeps [65, 66]. A high-efficiency, dual-balanced Michelson interferometer is used to detect the OCT signal. In this configuration, intensity noise from the laser source is cancelled out and the effective signal level is doubled by subtracting two out-of-phase interference fringes. The sample beam is scanned over the target by a pair of XY mirrors. A 200 MS/s, 2 channel, 14-bit A/D card is synchronized to the laser sweep and is used to record the calibration and OCT signals. A computer then resamples the OCT signals, carries out a Fourier transform, and produces a final image.

Several types of frequency-swept lasers have been developed for use in OCT imaging systems. Two early studies were performed by our group with bulk optic designs, one using a Cr:Forsterite laser operating at 1250 nm with a sweep rate of 10 Hz [46], and another using an external cavity diode laser operating at 800 nm with a sweep rate of 2 kHz [47]. An all-fiber ring laser employing a fiber Fabry-Perot tunable filter has been demonstrated at a sweep rate of 200 Hz [41]. Hybrid bulk optic and fiber cavity designs using a fiber-coupled semiconductor amplifier as a gain medium and a diffraction grating for wavelength selection have also been developed. For these designs, frequency sweep rates of up to 115 kHz have been achieved using a polygon rotating mirror to sweep the operating wavelength [64].

Since higher sweep rates allow correspondingly higher OCT imaging speeds, it is desirable to increase the sweep rate to the point where imaging becomes limited by detector bandwidth and A/D rates. Recently, our lab has developed a new class of frequency-swept sources called Fourier Domain Modelocked (FDML) lasers [67, 68]. These lasers synchronize the wavelength selective element, typically a fiber Fabry-Perot (FFP) filter, to the optical roundtrip time of the cavity, allowing all wavelengths in the sweep to build up and lase simultaneously within the cavity. Traditional swept sources, in comparison, require lasing to build up for each wavelength in the sweep in series, limiting the maximum achievable sweep rate. We have demonstrated FDML lasers at sweep rates of up to 370 kHz, achieving OCT imaging speeds of 370,000 A-scans per second. Sweep bandwidths are typically 100 – 145 nm (full width), giving OCT axial resolutions of 8 – 13 μm . At these extremely high sweep speeds, OCT imaging is limited by the photodetector bandwidths (350 MHz) and A/D rates (2 MS/s). For example, in order to perform true, real-time imaging at 380 kHz, it is necessary to use a digital oscilloscope with a 5 GS/s acquisition rate instead of a PC A/D card in order to capture every sweep.

Swept source OCT imaging has been performed in several applications where rapid acquisition at 1300 nm is highly desirable. Figure 1.18 shows an example of OCT imaging in highly scattering human skin at 42,000 axial scans per second and 10 frames per second [67]. Excellent penetration into the tissue is evident at depths >1 mm. Due to the high transverse line density (4096 lines per frame) and high sensitivity (96 dB) of the swept source OCT system, the image quality is very high. Rapid three dimensional imaging of epithelial tissue is also possible with FDML-based swept source OCT systems. Figure 1.19 shows two orthoslices of a 3D dataset taken from an *in vitro* sample of hamster cheek pouch fixed in formalin. This 512 x 512 x 200 pixel data was acquired at 124,000 axial scans per second, equivalent to 242 frames per second or 1.2 volumes per second [67].

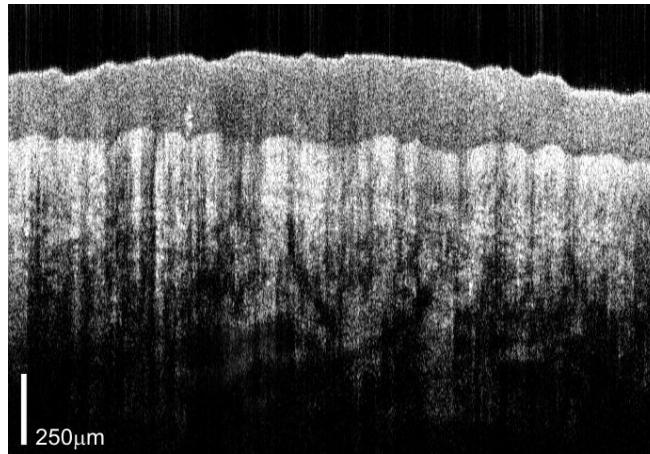


Figure 1.18. 1024 x 4096 pixel *In vivo* image of human skin acquired at 42,000 axial scans per second. Good image quality and penetration depth are observed.

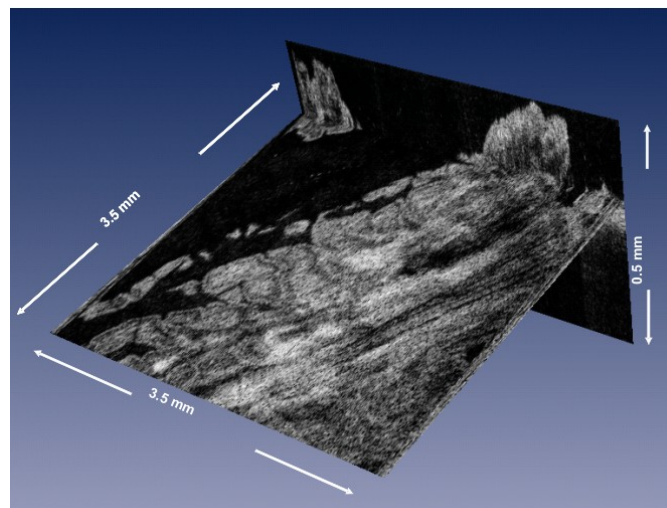


Figure 1.19. Two orthoslices of a 512 x 512 x 200 pixel 3D dataset taken from an *in vitro* sample of formalin fixed hamster cheek pouch. 3D data was acquired at 124,000 axial scans per second (1.2 volumes per second).

Another application for high speed, swept source OCT is intravascular imaging. In this application, blood flow through the vessel needs to be temporarily occluded to allow light to reach the surface of the vessel. Occlusion can be performed either by temporarily blocking the vessel with an inflatable balloon, or by flushing the vessel with a saline bolus. Both methods result in relatively short maximum imaging times, from 2-5 seconds with the saline flush to 35 seconds with balloon occlusion. High speed imaging is therefore crucial to maximize the vessel length that can be investigated during the limited occlusion time.

We have transferred FDML laser technology to LightLabs Imaging and this technology is being developed for their next generation intravascular imaging instrument. Figure 1.19 shows three dimensional images of an *ex vivo* pig artery using an FDML laser operating at 45,000 axial scans per second. The imaging catheter was pulled back through the artery at 10 mm/s as it rotated at 80 revolutions per second. The FDML laser was operated at 45,000 axial scans per second, giving 4500 OCT lines per mm in the artery. The entire 5 cm artery segment was imaged in only 5 seconds. This illustrates the potential of swept source OCT to become a powerful tool for applications which require rapid, survey imaging or large areas.

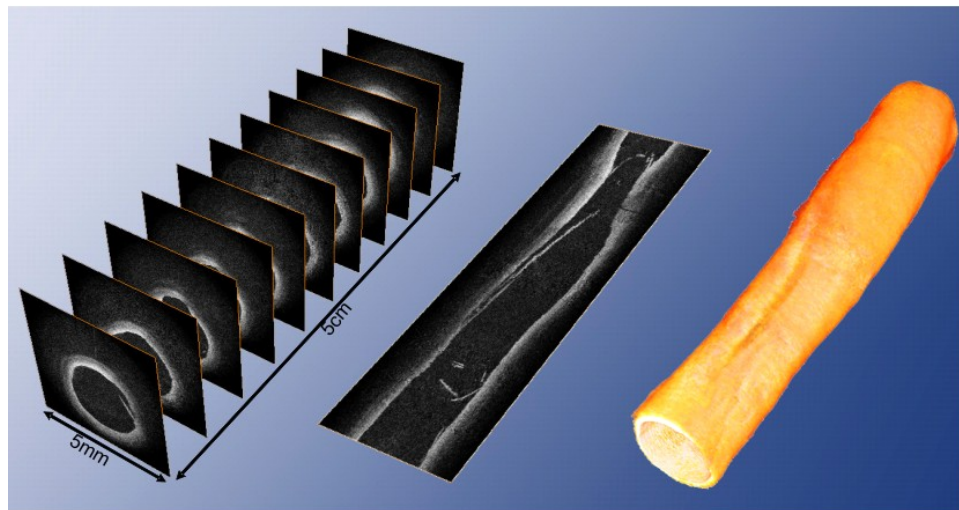


Figure 1.20. 3D OCT dataset taken from an *ex vivo* pig artery. Data was collected at 45,000 axial scans per second, giving 4500 lines per mm and covering the 5 cm artery segment in 5 seconds.

2. Ophthalmic Optical Coherence Tomography

Since its development in 1991, OCT has become a standard diagnostic technique in ophthalmology. Our group was responsible for the invention of OCT and the initial development of OCT for ophthalmology. The first report of OCT was published in *Science* in 1991 and demonstrated *in vitro* imaging of the human retina and atherosclerotic plaque [1]. With improved technology and the availability of extensive clinical data, OCT is rapidly becoming a standard of care in ophthalmology.

The current commercial OCT device (StratusOCT) has an axial resolution of 10 μm and can acquire an image in ~ 1.3 seconds. Recent research advances have enabled high-speed, ultrahigh resolution (UHR) OCT, achieving axial resolutions as fine as 2 μm and acquiring retinal images in ~ 0.02 seconds [45, 50, 69, 70]. Our current research focuses on developing high-speed, ultrahigh resolution OCT for clinical and fundamental research applications.

In many retinal diseases, clinical outcome is significantly improved by detecting disease during its early stages. Early-stage retinal disease is often characterized by small changes in architectural morphology or physiology. There is a need to comprehensively screen the retina for such changes, and quantitative, objective markers for disease progression and response to

treatment are required. Our high-speed UHR-OCT prototype enables three-dimensional imaging of the retina, acquiring comprehensive, micron-scale structural information necessary for early detection of retinal disease. We have developed a prototype instrument which is in use at the New England Eye Center for clinical studies imaging a range of retinal pathologies. In addition to performing qualitative cross-sectional studies of retinal diseases, our group is developing algorithms for quantitative analysis of OCT images and the creation of age-matched normative databases. The analysis of image information and the extraction of quantitative metrics is an important step toward developing clinically useful diagnostic protocols.

Another area of research is structural and functional OCT imaging in the murine (rat and mouse) eye. The murine eye is important due to its structural similarity to the human eye and relative ease of genetic manipulation, making it an important surrogate model for a number of retinal diseases. Our initial demonstration and subsequent investigation of *in vivo* functional imaging in the murine eye may pave the way to eventual applications of functional OCT in the human retina.

2.1 Ophthalmic ultrahigh resolution OCT instruments

The OCT instruments that we used for ophthalmic imaging are based on either time domain detection [1] (Figure 2.1 a) or spectral/Fourier domain detection [38, 39] (Figure 2.1 b). Ultrahigh resolution imaging ($\sim 2 - 3.5 \mu\text{m}$) was achieved with a femtosecond Ti:Sapphire laser light source [8, 71, 72] (bandwidth of 150 nm with central wavelength of 820 nm) or broadband superluminescent diode light source [73] (bandwidth of 90 nm centered at 840 nm). High speed data acquisition rates (up to 25,000 axial scans per second) were attained using spectral/Fourier domain detection.

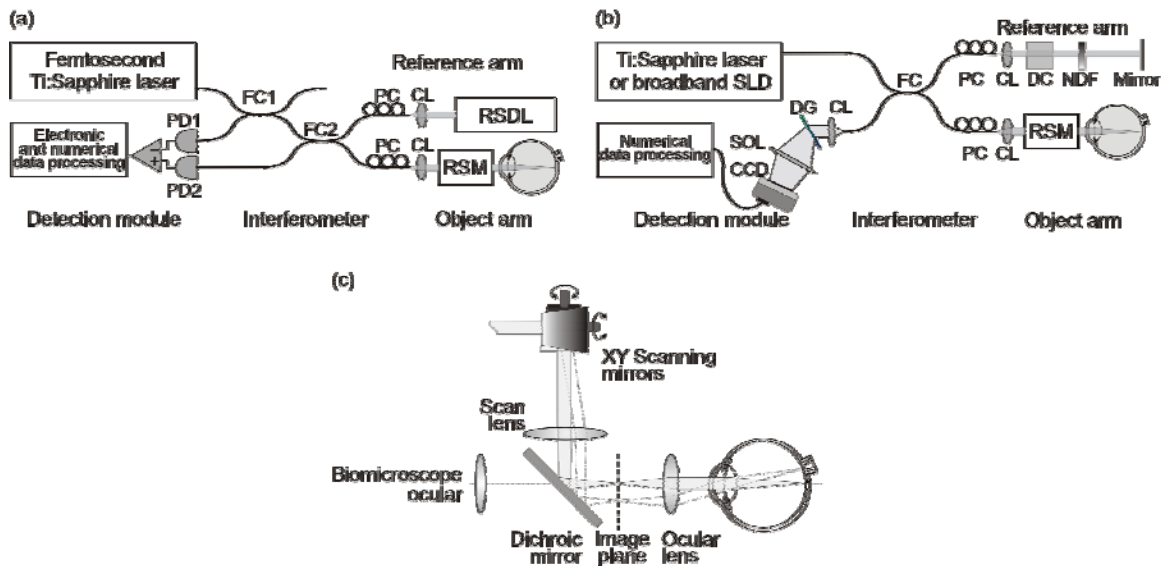


Figure 2.1. Schematics of OCT systems for ophthalmic imaging: (a) Time domain OCT system, (b) spectral/Fourier domain OCT system. (c) Retinal scanning module (RSM). FC fiber coupler, PC polarization controller, CL collimating lens, RSDL rapid scanning delay line, RSM retinal scanning module, PD photodiode, DC dispersion compensation, NDF neutral density filter, DG – diffraction grating, SOL spectrometer objective lens, CCD line scan CCD camera.

To provide the best visualization of retinal pathologies, we developed and investigated different image acquisition protocols. Imaging protocols initially proposed by our group in the mid 1990s have been implemented in commercially available devices [37, 74]. However, to take advantage of the enhanced performance of high-speed spectral/Fourier domain OCT, new imaging protocols are required [44]. One protocol acquires a small number of 6 mm high-definition images (8192 A-scans x 3 B-scans). It is especially useful for patients with opaque media or other conditions that result in a low OCT signal, as transverse pixel averaging can be used to increase the signal-to-noise ratio. A second protocol (Figure 2.2 a) acquires a series of high transverse pixel density images in a 6 mm x 6 mm raster pattern (2048 A-scans x 21 B-scans). A third protocol (Figure 2.2 b) acquires three-dimensional OCT (3D-OCT) data. It achieves comprehensive retinal coverage, taking measurements on a 6 mm x 6 mm area with a spacing of 12 μm x 33 μm between axial scans. The large set of cross-sectional images can be useful for tracking pathologies in three dimensions, or detecting small focal pathologies. A fourth protocol (Figure 2.2 c) consists of 24 radial scans with 1500 lines, centered at the fovea. This protocol can be used to map intraretinal layers and samples most densely in the fovea, the region most important for visual acuity.

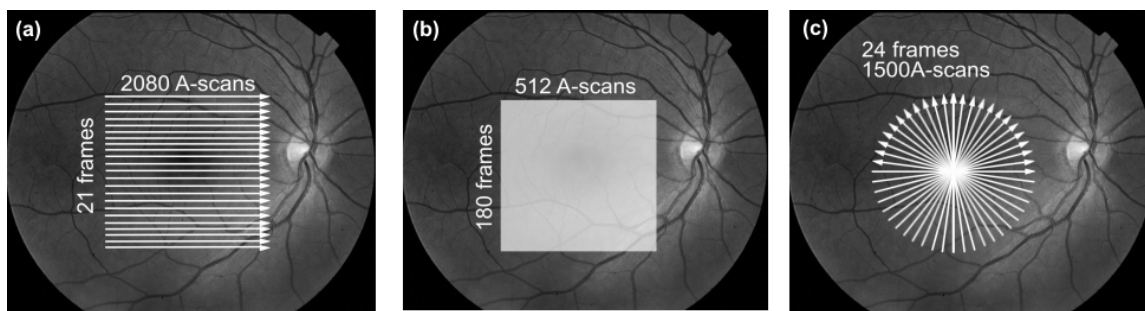


Figure 2.2. Examples of OCT scan protocols: (a) series of high transverse pixel density images in a 6 mm x 6 mm raster pattern (acquisition time: 1.8 seconds), (b) three-dimensional OCT data (acquisition time: 3.7 seconds), (c) radial scans (acquisition time: 1.4 seconds).

2.2 Studies on normal subjects

High-speed UHR-OCT has a number of advantages including improved image quality, preservation of retinal topography, improved retinal coverage. Images obtained using this technique show new features at the level of the photoreceptors and retinal pigment epithelium (RPE) which were not previously visible on slower, lower resolution systems (Figure 2.3).

The photoreceptor and RPE layers are thought to be especially vulnerable in early age-related macular degeneration, which is a major cause of vision loss in the developed world. The features in the outer retina must be quantitatively characterized in order to provide establish a definition of the “normal eye”. A normative baseline is important because it enables more accurate assessment of subtle variations from the norm, which may be early indicators of disease. The eventual goal of this work is to identify quantitative parameters that may be used to distinguish between the normal retina and early disease.

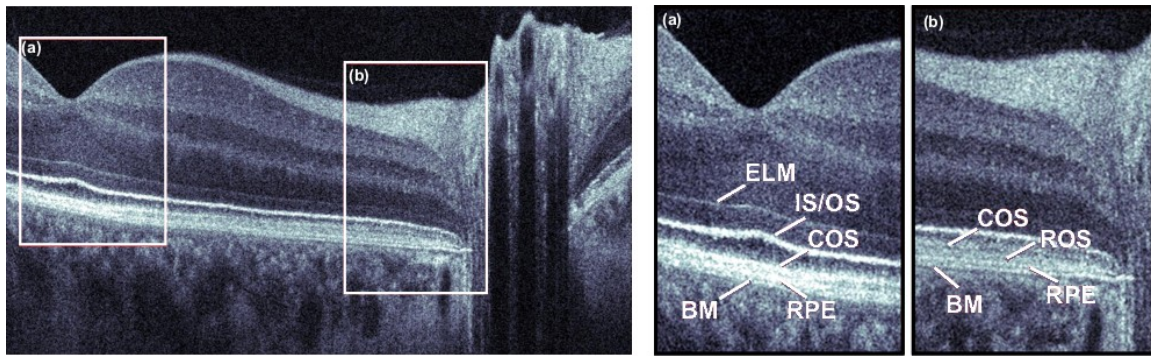


Figure 2.3. High speed UHR-OCT imaging of the normal retina. New features at the level of the photoreceptor layer and retinal pigment epithelium are visible. (a) Cone dominated foveal region of the eye. (b) Rod dominated area of the retina. ELM external limiting membrane, IS/OS inner/outer photoreceptor junction, COS cone outer segments, ROS rod outer segments, RPE retinal pigment epithelium, BM Bruch's membrane.

The distribution of thicknesses of different outer retinal layers in the macular region in a group of 48 eyes of 31 normal human subjects in the age range between 19 and 80 years was investigated. For segmentation of the outer photoreceptor layer, retinal pigment epithelium layer (RPE) as well as the whole outer retinal complex we used scanning protocol consisting of 24 radial scans (Figure 2.3 c) and segmentation software developed in our group. This software allowed us to perform thickness maps and quantitatively investigate correlation of different layers thicknesses with age. Example results of this study are shown in Figure 2.4.

2.3 Ultrahigh resolution OCT study of retinal pathologies

UHR-OCT provides new information about retinal structure that complements standard diagnostic techniques such as fluorescein angiography (FA), indocyanine green angiography (ICG) or fundus photography by providing cross-sectional images of micron-scale pathological changes. To take full advantage of this ability in ophthalmology, systematic cross-sectional and longitudinal studies of pathologies are necessary. These studies serve to illustrate features characteristic of various retinal pathologies and aid ophthalmologists in the interpretation of OCT images. Detailed qualitative and quantitative analysis of UHR-OCT images also enables characterization of early markers of pathologies and improved understanding of pathogenesis. Our group is conducting clinical investigations of different retinal disease in collaboration with New England Eye Center (NEEC) of Tufts-New England Medical Center (NEMC) and University of Pittsburgh Medical Center (UPMC). The study was approved by the IRB committees of MIT, NEMC and UPMC and is compliant with the Health Insurance Portability and Accountability Act of 1996.

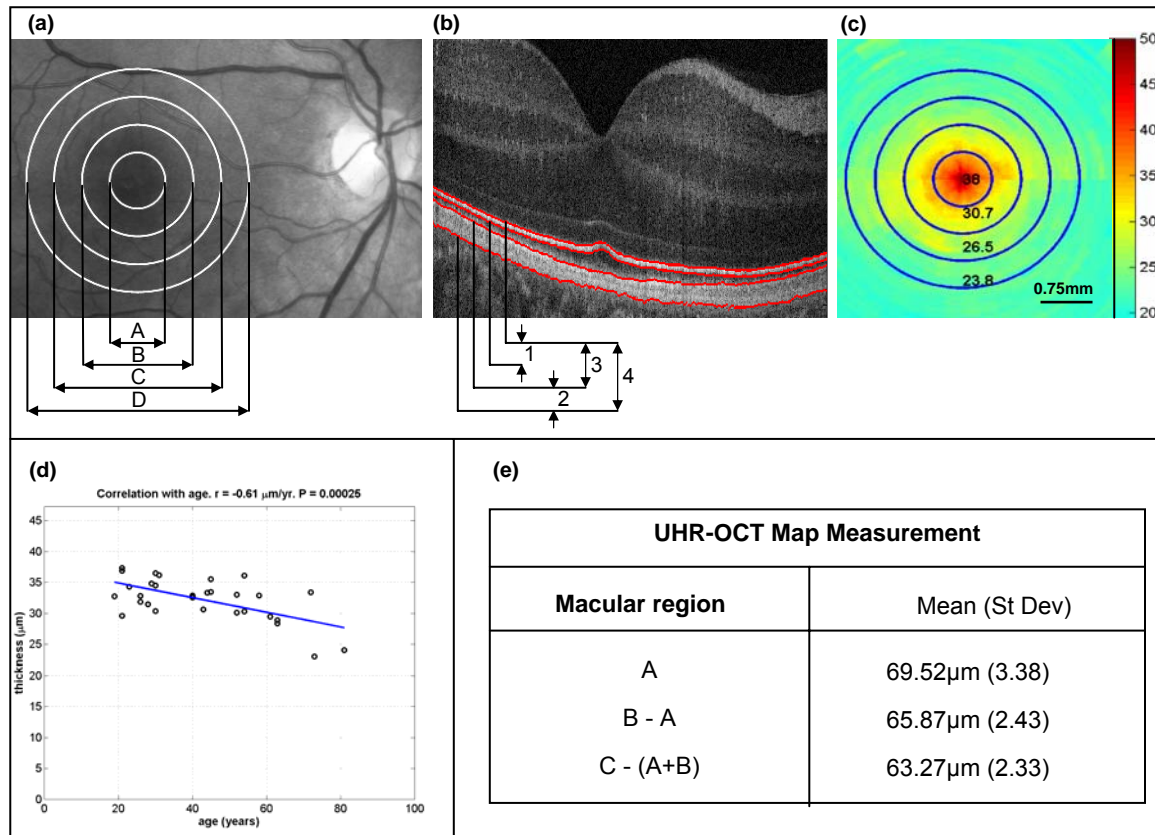


Figure 2.4. Study on normal subjects. (a) Selected macular regions within which quantitative analysis was performed: A = 0.75 mm, B=1.5 mm, C=2.25 mm, D=3.0 mm. (b) Segmentation of outer retinal layers: 1 – inner/outer photoreceptor junction, 2 – retinal pigment epithelium, 3 – photoreceptor outer segment, 4 – outer retinal complex. (c) Example thickness map of the photoreceptor outer segment (3) of normal eye. (d) Graph showing correlation within age of retinal pigment epithelium layer (2) thickness in the foveal region of the macula. (e) Table of quantitative measurements (mean values and standard deviations) of retinal outer complex (4) thickness in different macular regions.

A cross section of retinal diseases including: macular holes [72, 75-79], glaucoma [80-83], age-related macular degeneration [72, 78, 79, 84], epiretinal membranes [72, 78, 79], retinal dystrophies [85, 86], photoreceptor atrophies [87], retinal detachments [72, 88], vitreous detachments [78, 89] central serous chorioretinopathy [78, 79] retninis pigmentosa [72, 78, 90], choroidal neovascularization [78, 79], and others have been investigated to date.

2.4 Data visualization and analysis

Ultrahigh resolution OCT data should be visualized in a way that reveals all information relevant to diagnosis of retinal pathologies. In the simplest visualization method single B-scans (or OCT frames) showing the most representative cross-sections of investigated pathology are presented

using an appropriate color scale (commonly gray or false color scales representing different levels of light scattering in eye structures). Such a solution is usually utilized in standard resolution StratusOCT or ultrahigh resolution time domain OCT, where image acquisition speeds are relatively slow. However, with the advent of high-speed imaging, where as many as ~200 images are acquired at once, more advanced methods of visualization and data display are required.

Improvements in imaging speed enabled by spectral/Fourier domain OCT allow raster scan protocols (Figure 2.2 b) to obtain densely sampled three-dimensional OCT data. This data can be visualized using a range of novel visualization methods [71, 79]. For example, it can be used to create OCT fundus images by summing the three-dimensional data set along the axial direction at each transverse (*en face*) position on the retina (Figure 2.5. A, panel a). This corresponds to detecting all of the light backscattered or backreflected from each fundus position, and therefore is analogous to fundus photography or scanning laser ophthalmoscopy. Since the OCT fundus image is generated directly from the 3-D OCT data, OCT images are precisely and reproducibly registered with the fundus. The result is then displayed as a grey scale image that enables direct comparison of OCT findings with those from clinical examination, such as fundus photographs or fluorescein angiography. It is also possible to generate OCT fundus images selectively displaying specific retinal layers or specific retinal features (Figure 2.5. A, panel b).

Another set of different visualization methods is shown in Figure 2.5.B. Before visualization, individual frames from the three-dimensional data set were correlated to remove axial motion artifacts. Correlation between consecutive axial scans is unnecessary due to the fast acquisition rate. Virtual cross-sectional images, segmented, virtual perspective, and cut-away rendered views of the intraretinal layers were in this case generated using volumetric rendering software similar to that for magnetic resonance image processing.

Three dimensional data sets of radial scans densely covering the retina (Figure 2.2 c) may be used for quantitative analysis of OCT tomograms [71, 82, 91, 92]. Segmentation of different structures allows for calculation of volume of selected retinal features (Figure 2.5.B, panel f) as well as mapping intraretinal layer thicknesses. The later is especially important in quantifying macular edema which is a consequence of many pathological retinal conditions such as diabetic retinopathy, epiretinal membrane formation, ocular inflammation, retinal vascular occlusion, and cataract extraction. Macular thickness analysis is particularly helpful in guiding and assessing treatments for macular edema such as photodynamic therapy, intravitreal corticosteroids, and vitrectomy. It is also important for the detection and monitoring of glaucoma [82].

An example of retinal thickness analysis is shown in Figure 2.6. The patient had resolving central serous chorioretinopathy (CSCR) in the left eye. No pathological changes were observed in the right eye. The patient was imaged with high-speed UHR OCT using 24 radial scans (Figure 2.2 c). Figures 2.6 a show horizontal 6 mm OCT image through the macular region. The thickness of all retinal layers, outer retinal complex as well as retinal pigment epithelium (RPE) was mapped. The thickness maps of the RPE of both eyes are shown in Figures 2.6 c. Thinning of the RPE in the left eye is clearly visible.

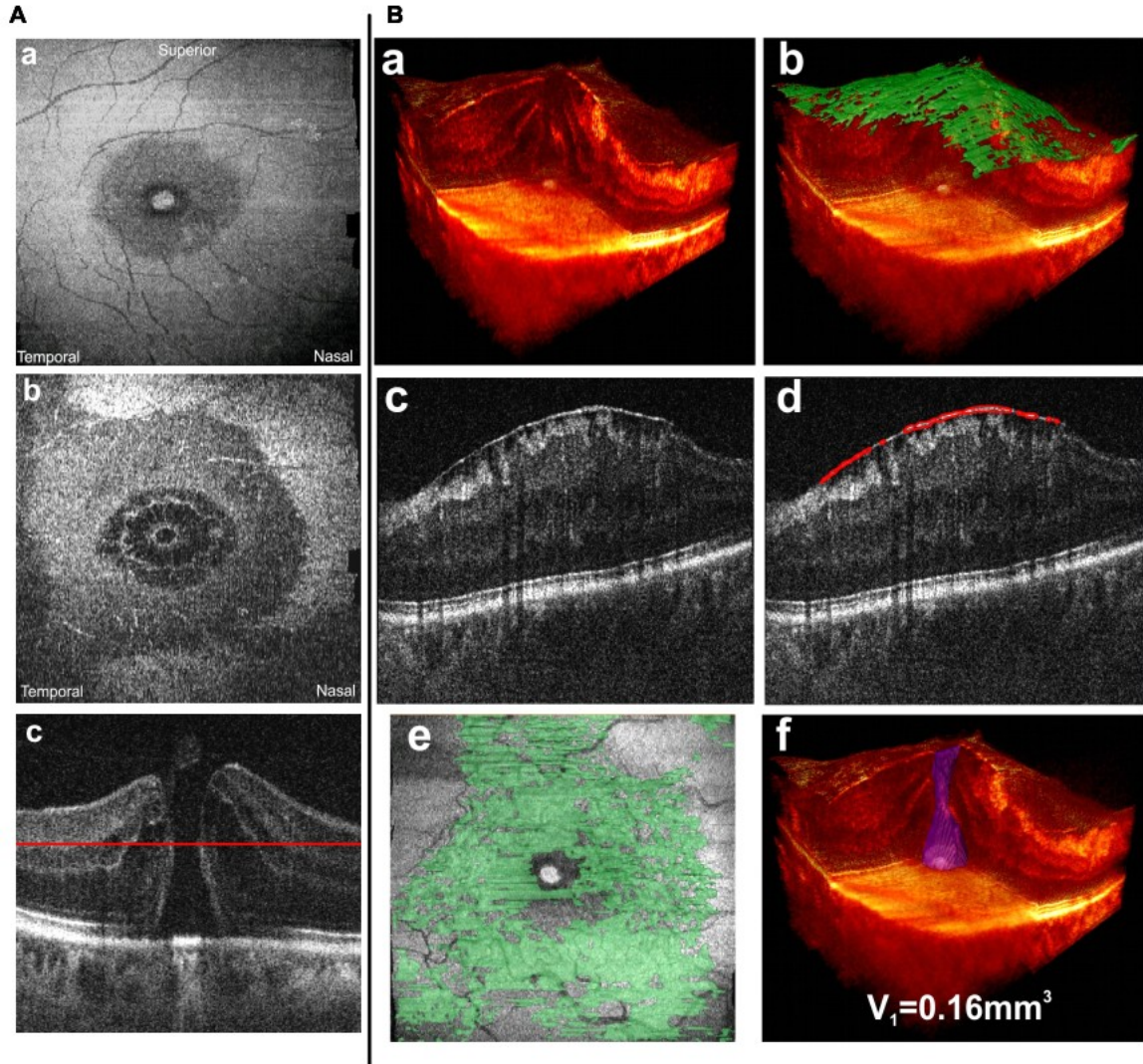


Figure 2.5. Visualization in high speed, UHR OCT imaging. (A) Full thickness macular hole: a. OCT fundus image created by summation data in the axial direction; b. Coronal section through macular hole (red line in Figure c), demonstrating "mosaic-like" cystic pattern surrounding macular hole; c. Cross-sectional view of macular hole. B. Volumetric analysis of high-speed, UHR OCT data of full thickness macular hole with epiretinal membrane. a. Volume rendering of the retina; b. Visualization of segmented epiretinal membrane along with the rendered volume; c. OCT image chosen from the three dimensional dataset showing epiretinal membrane; d. Segmentation of the epiretinal membrane in the same image; e. Map of epiretinal membrane registered to the OCT fundus image; f. Segmentation of macular hole and calculation of hole volume.

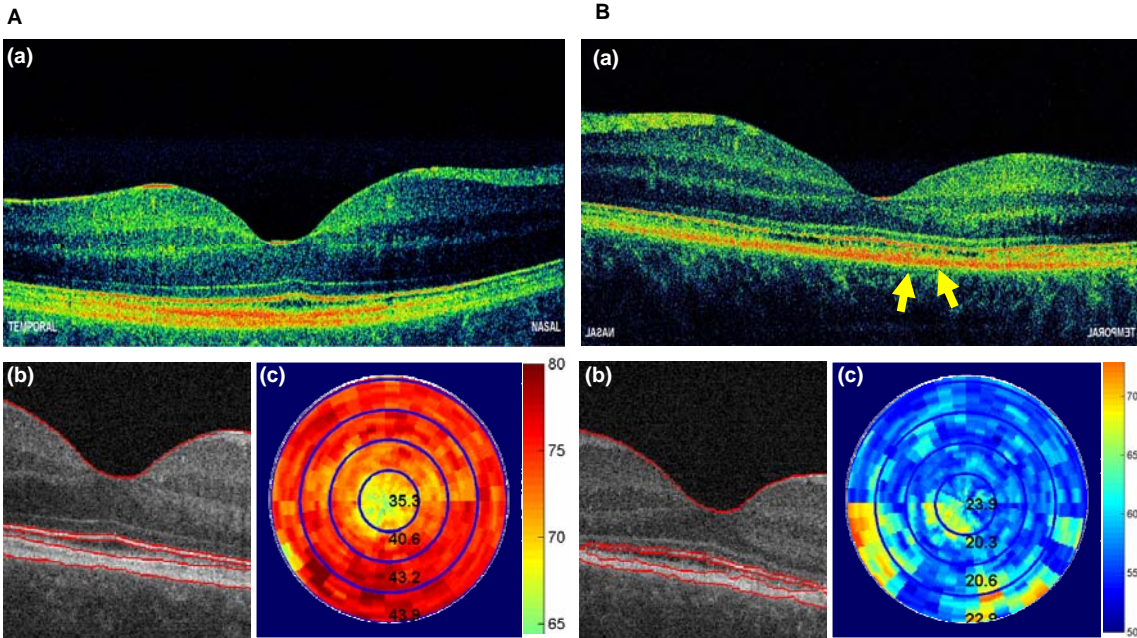


Figure 2.6. Macular thickness analysis. Example of a patient with resolving central serous chorioretinopathy in the left eye (B), and healthy right eye (A). (a) One of the OCT cross sections (horizontal) taken from the set of 24 radial scans (refer to the Figure 2.2 c). (b) Segmentation of different retinal layers in the macular region. (c) Thickness maps of the retinal pigment epithelium (RPE): thinning of the RPE in the left eye is visualized.

2.5 Small animal retinal imaging

Research on ocular diseases is limited by the restrictions on studying pathophysiologic processes in the human eye. Murine (rat and mouse) models of ocular disease therefore provide powerful tools for characterization of disease pathogenesis and response to treatment. While enucleation and histology are the gold standard for characterization of microstructural changes in animals, non-invasive structural imaging has the potential to reduce the need for sacrifice and histology in many studies. New OCT detection methods enable high-speed imaging as well as numerical dispersion compensation and spectral shaping, which are crucial for visualizing the fine structures in the retina.

A high-speed, UHR-OCT system was developed for small animal retinal imaging. This system achieves imaging speeds of 24,000 axial scans per second, an improvement of $\sim 100\times$ over previous UHR-OCT systems. Using a broadband superluminescent diode light source, an axial image resolution of $2.8\ \mu\text{m}$ is achieved. A $10\ \mu\text{m}$ transverse resolution in air is obtained using a post-objective scanning microscope. High-speed UHR-OCT enables high quality imaging of the murine retina and the visualization of all major intraretinal layers. Raster scan protocols enable volumetric imaging and comprehensive coverage of a region of the retina. An OCT fundus image, akin to a fundus photograph, can be generated by axial summation of three-dimensional OCT data, and enables precise registration of OCT measurements to retinal fundus features.

Figure 2.7 shows an example of an OCT cross sectional image (A) and a fundus image (B), which shows features such as retinal blood vessels. Three-dimensional imaging enables quantification of retinal structure, which promises to allow repeated, non-invasive measurements to track disease progression, reducing the need for sacrifice and histology. This capability can accelerate the translation from basic research studies in rats and mice into clinical care.

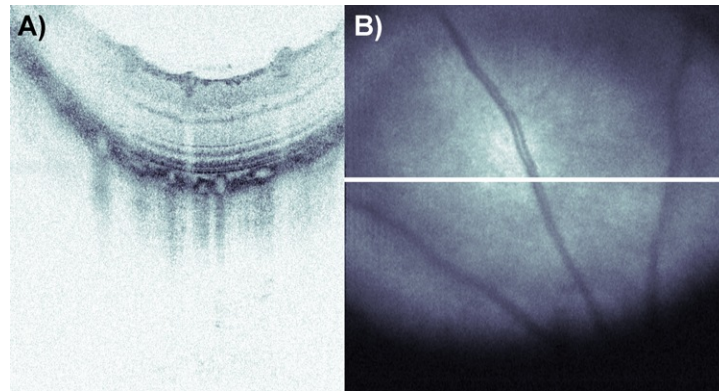


Figure 2.7. An OCT cross-sectional image of the rat retina (A) with the OCT fundus image (B), obtained by summation of 3D-OCT data. The location of the cross-sectional image on the OCT fundus image is shown by a white line.

2.6 Functional Retinal Imaging

Functional impairment may precede structural changes in a number of retinal diseases including age-related macular degeneration, glaucoma, and diabetic retinopathy. Objective methods for detecting functional impairment in the retina can improve sensitivity and reproducibility for tracking of changes over time. There are several objective methods for measuring the functional response of the retina and optic nerve including multifocal electroretinography, pattern electroretinography, multifocal visual evoked potentials, and pupil perimetry.

Recently, optical techniques have been demonstrated to provide physiological information. Small changes in optical properties caused by membrane depolarization and cell swelling have been measured in the cortex of the brain [93, 94]. Changes in oxygen saturation have been measured in response to retinal stimulation using fundus reflectometry [95]. Other studies demonstrated changes in retinal reflectance in response to a flash stimulus that correlated with multifocal ERG [96]. While these fundus imaging techniques provide good spatial resolution in the transverse direction, they do not have depth resolving capability.

OCT imaging of neural activity was demonstrated in the sea slug ganglion [97] as well as in the cat visual cortex [98, 99]. Recent work using conventional OCT demonstrated measurement of retinal functional changes in response to a flash stimulus [100, 101]. These studies showed changes in OCT signals in the photoreceptor inner and outer segments and were performed using *ex vivo* preparations. The investigators attributed the observed changes to photoreceptor disc membrane hyperpolarization in response to a strong stimulus, although this hypothesis remains to be tested.

Using high-speed, ultrahigh resolution OCT with 2.8 μm resolution and 24,000 axial scans per second, we demonstrated *in vivo* measurement of functional reflectance changes in the rat retina. The rat retinal model was chosen because of its widespread use in basic research on ocular disease. We have developed a novel measurement protocol that enables the simultaneous correction of motion artifacts and speckle averaging. This protocol enables a dramatic reduction of physiologic noise from motion and allows single shot measurements of photoreceptor function, without the need to average across multiple trials. The spatial and spectral dependence of the functional reflectance change was characterized, as well as the effect of photopigment bleaching.

For functional OCT experiments, animals are dark-adapted for 12 hours, anesthetized, and prepared under dim red light. A transient white light stimulus is delivered during the functional recording, while a selected region of the retina is repeatedly monitored for reflectance changes. The spectrum of wavelengths used in the OCT measurements was from 817-962 nm, well outside the sensitivity range of the rat retina. The stimulus duration and intensity were chosen to prevent full photoreceptor bleaching. Figure 2.8 shows the amplitude reflectance from the photoreceptor outer segments, plotted as a function of time. As shown, the stimulus induces a ~10-15% increase in the average amplitude reflectance from the photoreceptor outer segments.

OCT may eventually become a clinical tool for assessing photoreceptor health in the early stages of retinal disease. We have shown that single shot measurements can be achieved in the anesthetized rat. Our results and methodology are promising for the eventual application of these techniques in the ophthalmology clinic. OCT structural imaging can be performed to longitudinally follow areas of functional deficit for structural changes, or vice versa. The characterization of the response topography and temporal dependence in the rat model will be useful in developing protocols for functional OCT measurements in humans. Although the immediate application of functional OCT measurement technologies to humans is attractive, further systematic *in vivo* studies in a well-controlled retinal model such as the rat retina are important to characterize the observed optical changes.

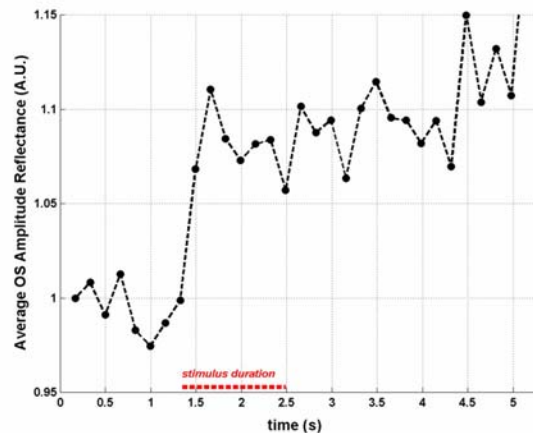


Figure 2.8. A light stimulus induces an increase in the average amplitude reflectance from the photoreceptor outer segments. Each data point in this figure corresponds to the average reflectance from the photoreceptor outer segments obtained from a small region of the retina.

3. Endoscopic OCT Studies

3.1 Endoscopic Imaging of Barrett's Esophagus

Optical coherence tomography (OCT) can generate high resolution, cross-sectional images of biological tissues *in situ* and in real time [1, 2, 102]. OCT can function as a type of optical biopsy to enable imaging of tissue microstructure with the resolution approaching that of standard excision biopsy, without the need of excising the tissue specimen [3-5]. One promising application of optical biopsy using OCT is the endoscopic imaging of the gastrointestinal (GI) tract. In contrast to conventional endoscopy, which can only visualize the surface alterations, OCT can detect changes in tissue morphology beneath the tissue surface. Therefore, endoscopic imaging with high resolution OCT could potentially improve the detection, visualization, and diagnosis of gastrointestinal diseases.

Several researchers have investigated endoscopic OCT imaging in the human gastrointestinal (GI) tract, including the esophagus and stomach, the small and large intestine, and the bile duct [103-113]. In addition to structural imaging, imaging of blood flow can also be performed using endoscopic Doppler OCT [114]. OCT imaging has demonstrated high sensitivities and specificities (100% sensitivity and 93% specificity in a retrospective study, 97% sensitivity and 92% specificity in a prospective study) for the identification of specialized intestinal metaplasia [115]. OCT imaging could also distinguish hyperplastic from adenomatous polyps in the colon [116]. Recent studies investigated the capability of OCT for detecting dysplasia in Barrett's esophagus. Evans et al. reported a sensitivity of 83% and specificity of 75% for detection of dysplasia with blinded scoring of OCT images [117]. Isenberg et al. reported an accuracy of 78% for the detection of dysplasia in patients with Barrett's esophagus [118]. However, currently almost all clinical studies have been performed using standard OCT with 10-15 μm resolution. Ultrahigh resolution OCT could enhance the imaging performance for the identification of early neoplastic changes, and could improve the sensitivity of biopsy by reducing false negative rates from sampling errors.

Our group developed a research prototype ultrahigh resolution endoscopic OCT system for use in the endoscopy suite. In order to achieve the high powers and short coherence lengths necessary for high resolution, high speed imaging, a Cr:Forsterite laser was used as the light source [25]. This laser generates broadband spectrum in the 1300 nm wavelength regime. The output bandwidth can be increased by using nonlinear effects in optical fibers to yield a coherence length of 5 μm or less. Due to the bandwidth limitations in the optical components in the sample and reference arms, the back-coupled spectrum on the detector had a bandwidth of 150 nm, which corresponds to a theoretical axial resolution of 4.6 μm in air. The width of the measured axial point spread function is 5 μm , corresponding to ~ 4 μm resolution in the tissue, which is 2-3x finer than standard OCT systems. The system sensitivity was 102 dB at 4 Hz frame rate with up to 15 mW power on the sample.

Working in collaboration with Dr. Hiroshi Mashimo, MD, PhD at the Harvard Medical School, we performed a study to investigate endoscopic OCT imaging. Ultrahigh-resolution (UHR) OCT imaging was performed in the esophagus and stomach of patients undergoing upper GI endoscopy at the Boston Veteran Affairs Medical Center (VAMC). Informed consent was

obtained from patients enrolled under a protocol approved jointly by the Institutional Review Board (IRB) of Boston VAMC, the Committee on Human Studies at Harvard Medical School and the Committee on the Use of Humans as Experimental Subjects (COUHES) of Massachusetts Institute of Technology. Imaging was performed using a 1.8 mm OCT imaging catheter which was introduced through the accessory channel of the endoscope. The OCT imaging catheter was disinfected prior to use. While in the field of view of the endoscope, the OCT imaging catheter was positioned to the areas of interest by maneuvering the tip of the endoscope.

A total of 50 patients with previous history of Barrett's esophagus were imaged. Images from both normal and abnormal areas in the upper GI tract were acquired and later classified according to the results of pinch biopsy histology. The pathologic diagnoses from biopsy specimens included: Barrett's esophagus without dysplasia (17), indefinite for dysplasia (5), low-grade dysplasia (16), high-grade dysplasia (4) and adenocarcinoma (2).

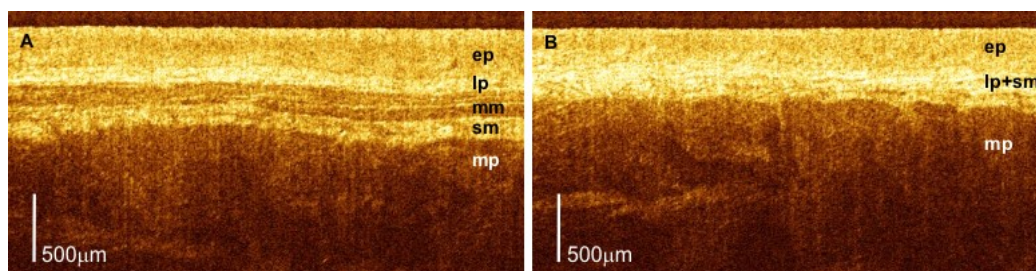


Figure 3.1. A, B: In vivo images of normal esophagus acquired using ultrahigh resolution endoscopic OCT (wavelength 1.3 μm , resolution 5 μm axial x 15 μm transverse). Layered architecture of the esophageal wall including the epithelium (ep), lamina propria (lp), muscularis mucosae (mm), submucosa (sm), muscularis propria (mp) are visualized.

Figure 3.1 shows UHR OCT images of normal esophagus with squamous epithelium. Figure 3.1A reveals the characteristic five-layer architecture of normal esophagus mucosa which has been observed in previous standard resolution OCT imaging studies. The UHR OCT images show the relatively homogeneous epithelium (ep), the high-backscattering band (brighter) of the lamina propria (lp), the low-backscattering (darker) muscularis mucosae (mm), the high-backscattering submucosa (sm), and the low-backscattering and thick muscularis propria (mp). A three-layered architecture was also identified in the same patient as shown in Figure 3.1B. The high-backscattering connective tissue layers of the lamina propria and submucosa merge without the lower back-scattering muscularis mucosae between them. This finding is consistent with the fact that the longitudinal fibers of the muscularis layer occur in bundles, and a given cross-sectional OCT image may not intercept one of these bundles. The identification of the muscularis mucosa is important for staging of esophageal cancer. Although these features have been observed in standard resolution OCT, they are sharper and easier to identify in UHR OCT images.

Representative endoscopic images with the catheter placement and resulting UHR OCT images of regions of Barrett's esophagus from different patients are presented in Figure 3.2. The UHR

OCT images demonstrated clear differences in the tissue architecture of the Barrett's region when compared to normal esophageal squamous mucosa. The horizontally layered esophageal squamous epithelium was replaced by the presence of crypt-like glandular architectures, which are more heterogeneously scattering compared to normal esophagus. Low-backscattering glands were frequently observed within Barrett's mucosa, with interlaced regions of high-backscattering connective tissue corresponding to the lamina propria. Although individual patients exhibited variation in the detailed architecture of Barrett's metaplasia as visualized with UHR OCT, the common OCT image features of crypt-like glandular architectures were present in all patients with Barrett's esophagus. The deeper horizontal stratified muscularis mucosae and submucosal layers of the normal esophagus were preserved in patients with Barrett's esophagus.

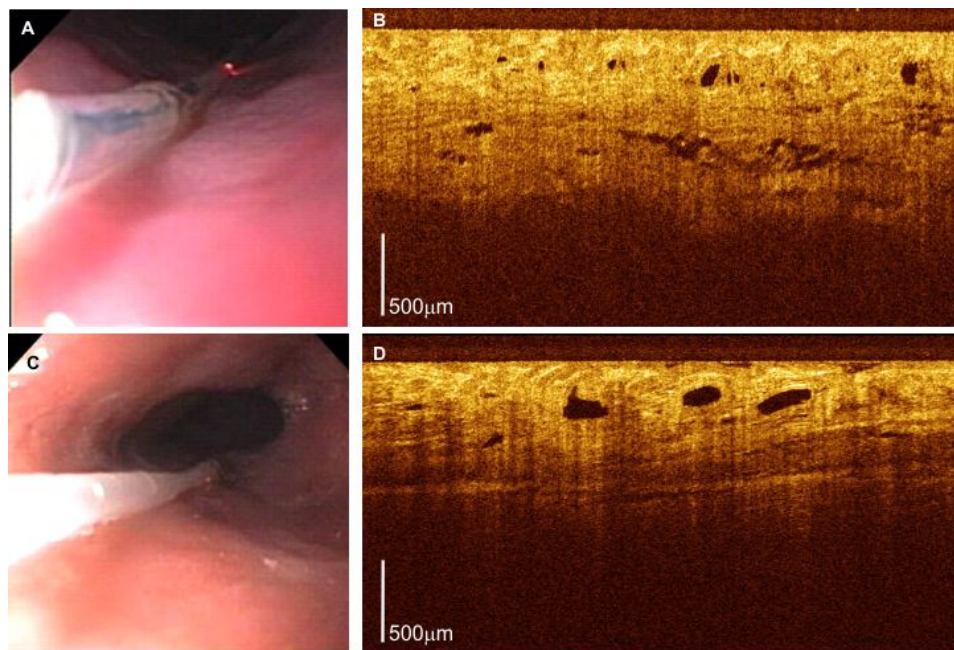


Figure 3.2. Ultrahigh resolution endoscopic OCT imaging of Barrett's esophagus from 2 patients showing variation in Barrett's morphology: A, C: Endoscopic view; B, D: OCT images (wavelength 1.3 μm , resolution 5 μm axial x 15 μm transverse). A, B are from the same subject; C, D are from the same subject.

Figure 3.3 shows a case of esophageal adenocarcinoma underneath benign squamous epithelium in a patient status post photodynamic therapy (PDT). The irregularly backscattering neoplastic mucosa of the adenocarcinoma is dramatically different from that of normal and Barrett's esophagus. OCT images of adenocarcinoma show heterogeneous scattering corresponding to prominent morphologic disorganization, irregularly shaped and crowded glandular architecture, with reduced overall back-scattering intensity. Features of esophageal adenocarcinoma visualized with UHR OCT agree with those found in previously published OCT imaging studies and are consistent with pathological findings. Qualitatively, the OCT images show progressive increase of architectural irregularity from Barrett's esophagus to high-grade dysplasia and eventually to adenocarcinoma. A comparison was also performed to investigate imaging results between endoscopic ultrasound (EUS) and UHR OCT. Figure 3.3 shows both types of images derived from the same patient. UHR OCT demonstrates higher imaging resolution for epithelial

architecture than standard radial EUS. However, EUS has higher image penetration than OCT, enabling the depth of the tumor invasion to be assessed. This result suggests that these two imaging modalities might provide complementary information for the detection and staging of esophageal adenocarcinoma.

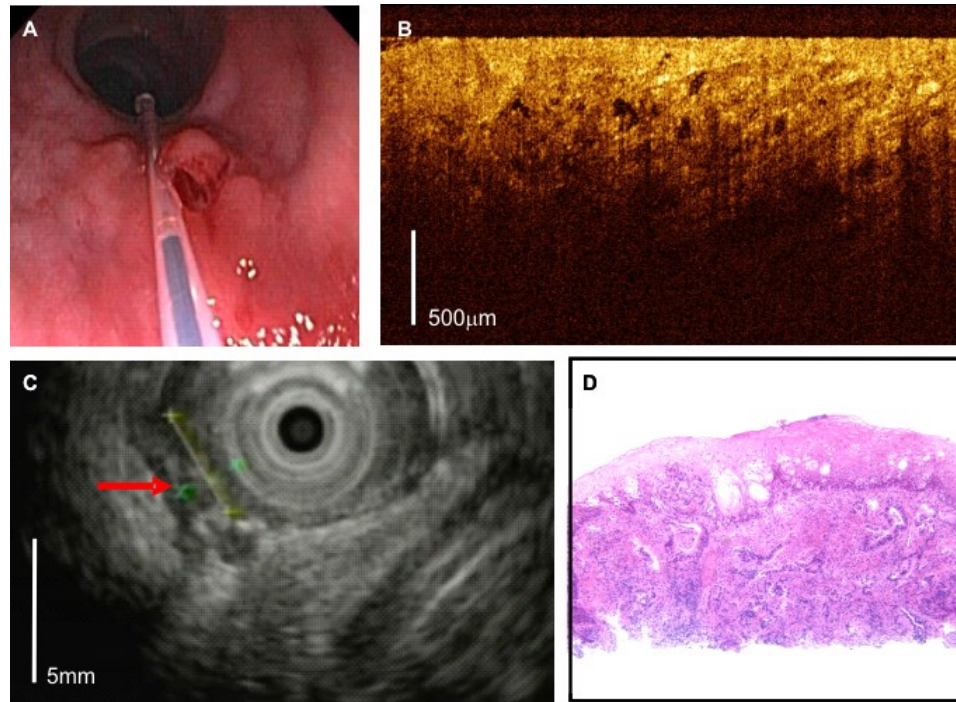


Figure 3.3. Ultrahigh resolution endoscopic OCT imaging of adenocarcinoma from a patient status post PDT. A, Endoscopic view; B, OCT image (wavelength 1.3 μm , resolution 5 μm axial x 15 μm transverse); C, Endoscopic ultrasound images of the same area; D, Corresponding histology (H&E, ori. mag. x40).

These studies demonstrate the ability of UHR OCT to differentiate normal and pathologic tissue. The improved image resolution of OCT enabled the visualization of architectural morphology features such as the normal layered structure of the epithelium versus glandular and columnar structures associated with Barrett's esophagus more clearly. Further and more detailed investigations using ultrahigh resolution OCT imaging in clinical endoscopic studies will be necessary to evaluate the ultimate impact of improved resolution on the diagnostic capabilities for detecting Barrett's esophagus associated high-grade dysplasia and carcinoma. In the context of surveillance of patients with Barrett's for high grade dysplasia and adenocarcinoma, the most intriguing application of OCT would be to direct excisional biopsy to reduce sampling errors. One can envision new OCT imaging probes which integrate OCT imaging with pinch biopsy to provide a real time "first look" at pathology prior to excision and processing of a specimen. If successful, this technology could be used to help guide excision biopsy to reduce sampling errors and false negative rates. This could improve sensitivity of diagnosis, reduce the cost of surveillance and provide enhanced diagnosis and treatment decisions.

3.2. Image Analysis Methods

Image analysis has been extensively applied in various biomedical imaging technologies, such as ultrasound, magnetic resonance imaging (MRI), and computerized tomography (CT), to assist in the diagnosis of diseases. Previous studies have demonstrated the diagnostic capability of endoscopic OCT in Barrett's esophagus [115], esophageal dysplasia [117, 118] and colon dysplasia [116] by assessment of tissue morphological disorganization. However, such human-based diagnosis approaches would require the special training in interpreting the OCT images, might result in the intra- and inter-observer variations, and potentially become time-consuming if the number of images is large. Recently, computer-based image analysis approaches have been applied to OCT images for classification and diagnosis [119, 120]. Preliminary studies have demonstrated the promise of diagnosis of dysplasia from Barrett's esophagus using texture analysis on standard resolution OCT images (15 μm axial resolution) [120]. This approach will potentially minimize the intra- and inter-observer variations, and enable automatic analysis of large volume of data sets through computer aided diagnosis (CAD).

We have investigated the capability of automatic tissue characterization and diagnosis using texture analysis for both standard-resolution (SDR-OCT) and ultrahigh-resolution OCT (UHR-OCT) in detection of Barrett's esophagus (BE). Image features such as coarseness, contrast, periodicity, and orientation can be quantified using texture analysis. Features of 50 endoscopic OCT images (25 normal and 25 Barrett's esophagus) were extracted through computational metrics including the spatial frequency analysis using two-dimensional Fourier transform (2D FFT), and statistical texture analysis using center symmetric auto-correlation [121] (see Equation 3.1). These features were further processed using principle component analysis (PCA) to reduce the variable dimensions and increase the discriminative power.

$$\begin{aligned} \text{SCOV} &= 1/4 \sum (g_i - u)(g_i' - u) \\ \text{VAR} &= 1/8 \sum (g_i^2 - g_i'^2) - u^2 \\ \text{BVAR} &= 1/16 \sum (g_i + g_i')^2 - u^2 \\ \text{WVAR} &= 1/16 \sum (g_i - g_i')^2 \\ \text{SVR} &= \text{WVAR} / \text{BVAR} \\ \text{SAC} &= \text{SCOV} / \text{VAR} \\ *u: &\text{local mean value} \end{aligned}$$

| | | |
|--------|--------|--------|
| g_2 | g_3 | g_4 |
| g_1 | | g_1' |
| g_4' | g_3' | g_2' |

Equation 3.1. Algorithm for calculating the image features through center symmetric auto-correlation. SCOV gray scale texture covariance, SAC normalized SCOV, BVAR between-pair variance, WVAR within-pair variance, VAR: local variance, SVR variance ratio.

Figure 3.4 plots the first two principle components (T1 and T2) from PCA for normal and Barrett's esophagus image features. T1 and T2 are linear combinations of original variables, including 2D FFT features and statistical texture features. The quantitative metrics are: 1) the variable reduction; 2) separation capability. Variable reduction is estimated by the variances of

first two principle components (T1 and T2). UHR-OCT shows more distinct difference in T1 and T2, suggesting data are more spread out in one dimension therefore facilitates the further discrimination (see Table 3.1). The discrimination capability for normal and BE groups is estimated by t-statistic which is the ratio of the distance between the centroid of two groups (between-group) divided by the weighted standard error of each group (within-group). UHR shows larger ratio of between-group variance to within-group variance than SDR (Table 3.2), suggesting the normal and Barrett's esophagus data are further separated in UHR OCT images. These results suggest that the improved axial resolution will enhance the capability in discerning the fine features in OCT images, which could be useful in diseases diagnosis. The enhanced classification abilities using UHR OCT would help in the computer aided diagnosis of GI diseases. This work demonstrates enhanced discrimination of Barrett's esophagus from normal esophagus, but these results may also prove important in the discrimination of dysplasia from Barrett's tissues. Similar analysis algorithms have been applied to high-grade dysplasia images and the analysis is undergoing.

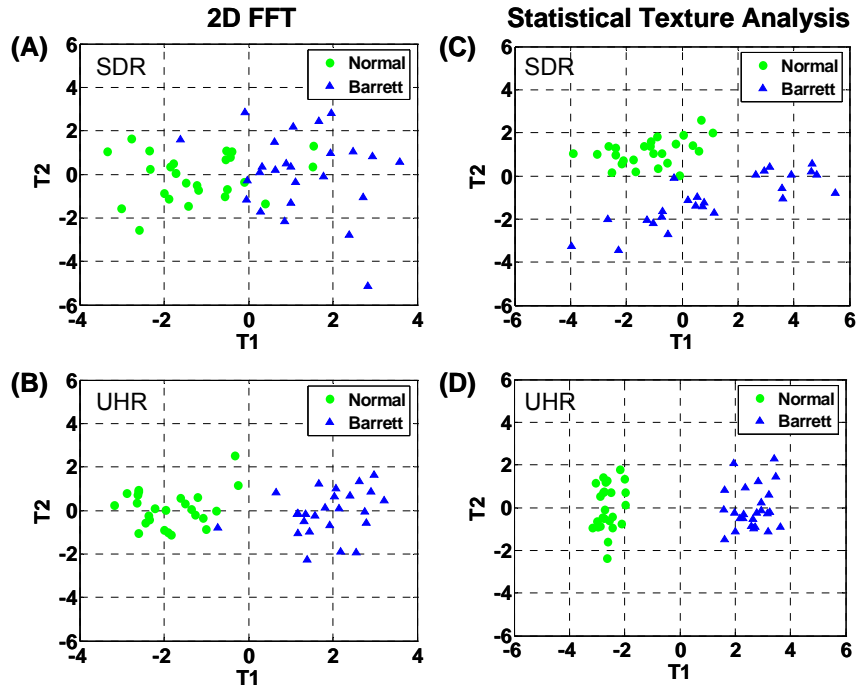


Figure 3.4. Scatter plots of first two principle components (T1 and T2) from PCA for normal and Barrett's esophagus. T1 and T2 are linear combinations of original variables, including 2D FFT features (A,B) and statistical texture features (C,D). A: Plots of T1 and T2 from 2D FFT features of SDR images; B: Plots of T1 and T2 from 2D FFT features of UHR images. The UHR features shows more condensed along T1 axis (more variance in T1 and less variance in T2 compared to SDR features, see values in Table 3.1). BE and normal groups are further separated in UHR (see values in Table 3.2). C: Plots of T1 and T2 from texture features of SDR images; D: Plots of T1 and T2 from texture features of UHR images. Similarly, the UHR features shows more concentrated along T1 axis and further separated for BE and normal groups.

Table 3.1. Comparison of Variable Reduction

| Variance | SDR (FFT) | UHR (FFT) | SDR (Texture) | UHR (Texture) |
|----------|--------------|-----------|------------------|------------------|
| T1 | 3.02 | 4.23 | 5.57 | 7.21 |
| T2 | 2.23 | 0.88 | 2.10 | 1.06 |

Table 3.2. Comparison of Discrimination

| t-Statistics | SDR | UHR |
|--------------|-------|-------|
| FFT | 7.07 | 16.05 |
| Texture | 10.40 | 37.77 |

4. Optical Coherence Microscopy

4.1 Introduction

Ultrahigh resolution Optical Coherence Tomography (OCT) can achieve 1-2 μm axial resolution in tissue, but is limited in transverse resolution due to the low numerical aperture (NA) focusing to maintain a sufficient depth of field over the range of the cross-sectional image [8]. The relatively low lateral resolution achievable with cross-sectional OCT is generally insufficient for imaging of cellular features and therefore limits the utility of OCT in applications requiring cellular level diagnostics. To extend the imaging power of OCT to very high transverse resolution, we are developing a technology known as Optical Coherence Microscopy (OCM), which combines OCT with confocal microscopy. Figure 4.1 compares the image penetration depth and resolution of OCM with that of OCT and confocal microscopy. OCM can provide enhanced penetration depth compared to standard confocal microscopy while dramatically improving the resolution over typical cross-sectional OCT imaging methods.

Optical Coherence Microscopy overcomes the depth of field limitation present in traditional OCT imaging by imaging in the *en face* plane rather than the cross-sectional plane. To image *en face*, the optical path length of the reference arm is matched exactly to the focus of the sample arm microscope while scanning a transverse raster pattern on the tissue. This eliminates the need for path length scanning to generate an axial depth map and allows the use of high NA lenses to provide very small spot sizes. Because of the high NA focusing used in OCM, the field of view in the images is necessarily smaller than in OCT. OCT images architectural features over a field of view of 3-6 mm square while OCM can image down to the cellular level but with reduced field of view of 100-500 μm square.

OCM has the unique advantage of using two distinct optical sectioning techniques – confocal gating and coherence gating. The multiplicative effect of the two sectioning methods strengthens the overall optical sectioning power, allowing increased rejection of unwanted, out of focus

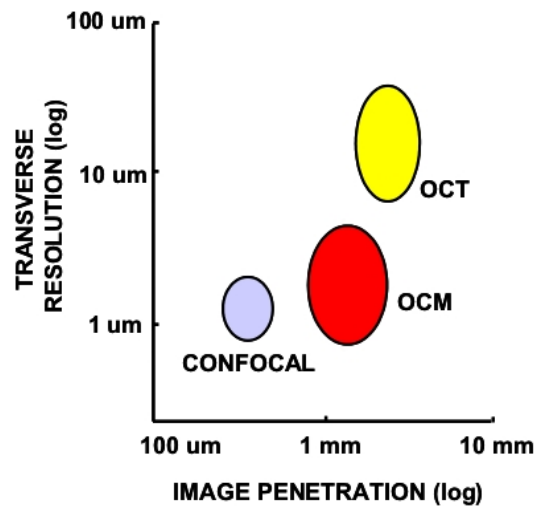


Figure 4.1. Transverse resolution and image penetration in optical coherence microscopy (OCM). OCM can enhance image penetration compared to confocal microscopy alone while significantly improving transverse resolution in OCT to enable cellular level imaging.

scattered light. Studies from our group as well as others have demonstrated that combined confocal and coherence gating can provide improved imaging depth compared to confocal alone [122, 123]. The addition of high sensitivity coherence gated detection to confocal detection extends the imaging depth in scattering media to the shot noise quantum limit, providing a factor of 2-3 increase over standard confocal microscopy.

The use of multiple optical sectioning techniques also allows considerable flexibility in system design for achieving high-resolution cellular images. Broad bandwidth light sources as used in ultrahigh resolution OCT can provide thin optical sectioning via coherence gating, and the confocal sectioning can be relaxed to facilitate development of miniaturized imaging devices.

Figure 4.2 compares the confocal axial and transverse imaging resolution as a function of the numerical aperture of the probe optics to demonstrate this operating limit for OCM. The axial section thickness degrades much more quickly than the transverse resolution, and there exists a region where the transverse resolution is sufficient for cellular imaging but the axial resolution is not. Addition of a short coherence gate to provide tissue sectioning can therefore make cellular imaging possible with much lower NA than is sufficient for confocal microscopy alone. This operating regime for OCM imaging has very important clinical implications, since it promises to allow cellular imaging with small diameter probes compatible with standard endoscopic and laparoscopic procedures.

We have developed a high speed OCM system capable of imaging with broadband femtosecond laser sources as used in ultrahigh resolution OCT. The system used a femtosecond Ti:Sapphire laser and a novel broadband optical phase modulator to provide high resolution imaging at 800 nm wavelength. Figure 4.3 presents key results. A short coherence gate of $\sim 3 \mu\text{m}$ was combined

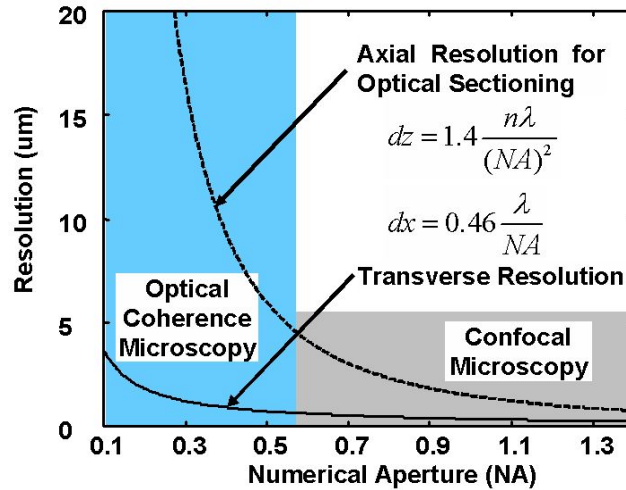


Figure 4.2. Numerical aperture requirement for OCM compared to confocal microscopy. OCM can image with high transverse resolution at much lower numerical aperture than confocal microscopy because it does not depend on high axial resolution for optical sectioning.

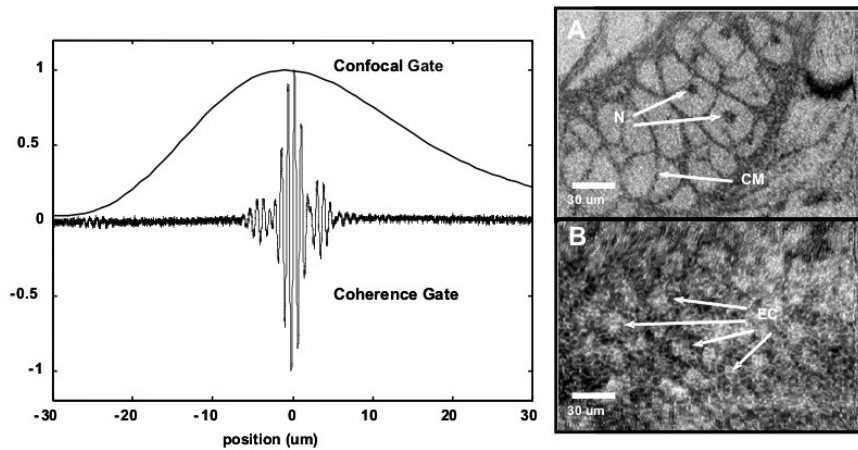


Figure 4.3. OCM can perform cellular imaging with lower NA than confocal microscopy. (Left) A short coherence gate is used to compensate a longer confocal gate, which will relax probe design constraints for endoscopic imaging. (Right) High transverse resolution cellular imaging can be achieved despite weaker confocal sectioning. *In vivo* OCM cellular imaging was performed in *Xenopus laevis* tadpole (A) and human skin (B). Nuclei (N), cell membranes (CM) are visible in the tadpole images, and epidermal cells (EC) can be seen in the skin images. Images were acquired at 800 nm wavelength at 4 frames per second.

with a confocal gate of $\sim 30 \mu\text{m}$. While this confocal section thickness is nearly 6 times that of standard histology, a high transverse resolution of $< 2 \mu\text{m}$ can still be maintained. Together the combined gating effects are sufficient for high-resolution *in vivo* imaging of cellular features in various tissues, demonstrated in *Xenopus laevis* tadpole and in human skin. In both *Xenopus* tadpole and in human skin, cellular features were clearly visualized.

4.1 OCM Imaging of Pathology

Pilot ex vivo imaging studies were conducted in the clinical pathology laboratory to assess the feasibility for cellular resolution imaging in endoscopy. These studies were performed in collaboration with Dr. James Connolly, M.D., Chief of Anatomic Pathology, from the Beth Israel Deaconess Medical Center in Boston. A total of 75 samples from 39 patients were imaged. Normal specimen subtypes included squamous esophagus (10), stomach (3), small intestine (5), colon (11), and pancreas (2). Pathology specimen subtypes included columnar-lined esophagus (11), esophageal adenocarcinoma (1), celiac disease (1), inflammatory bowel disease (3), acute inflammation (2), chronic colitis (2), melanosis coli (1), tubular adenoma (11), hyperplastic polyp (5), colorectal adenocarcinoma (4), cholecystitis (2), and chronic pancreatitis (1). Figures 4.4 and 31 present sample data from this study. Figure 4.4 a illustrates the characteristic pattern of squamous cells in the esophagus. Corresponding histology is shown in Figure 4.4 b. In the OCM images as well as histology, cell nuclei can be clearly differentiated from the surrounding cytoplasm and individual membranes delineate cell boundaries. Figures 4.4 c and 4.4 d show an example of Barrett's esophagus. Barrett's esophagus is a condition in which chronic gastrointestinal reflux leads to a metaplastic change in the esophageal mucosa from the normal squamous pattern to a columnar pattern with similar features to colonic mucosa. The presence of Barrett's metaplasia is a predisposing risk factor for the development of dysplasia and adenocarcinoma of the esophagus. The hallmark histopathologic feature of Barrett's esophagus is the barrel-shaped goblet cell. OCM identifies the glandular architecture of the Barrett's mucosa as well as the presence of goblet cells in the columnar epithelium.

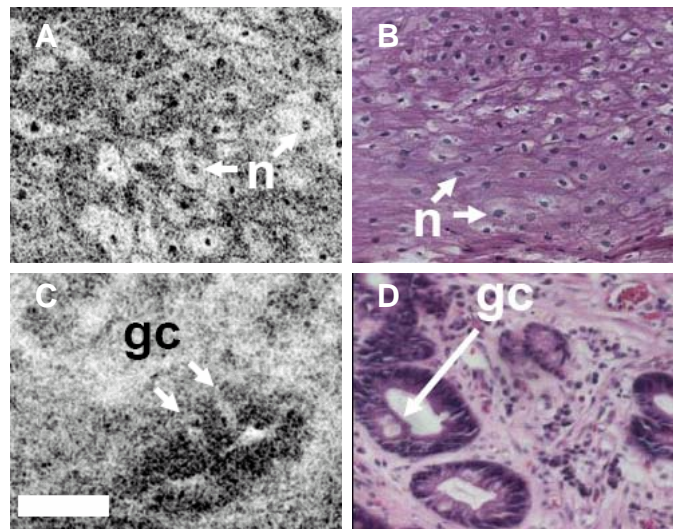


Figure 4.4. OCM images and histology of normal esophagus (A,B) and Barrett's esophagus (C,D) *in vitro*. Normal squamous mucosa has squamous cells with centrally-located, highly scattering nuclei (n). Barrett's epithelium has intestinalized glands with barrel-shaped goblet cells (gc).

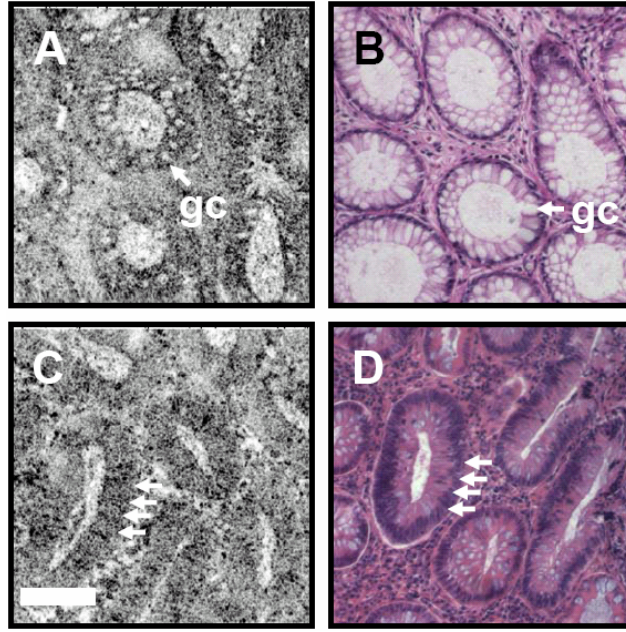


Figure 4.5. OCM and histology of normal (A,B) and dysplastic (C,D) colon *in vitro*. Normal colonic mucosa has round crypts with goblet cells (gc) and basally situated nuclei. Adenomatous dysplastic crypts have more eccentricity and cigar-shaped nuclei.

Figure 4.5 shows a comparison of OCM images of normal and dysplastic colonic mucosa. The normal colonic mucosa shown in the OCM images and histology of Figures 4.5 a and 4.5 b, respectively, illustrates a regular pattern of round crypts with numerous goblet cells and nuclei restricted to the basal aspect of the columnar epithelium. In contrast, Figures 4.5 c and 4.5 d present images and histology from a tubular adenoma with low grade dysplasia. Glands in the adenoma are larger and exhibit significant eccentricity compared to the small round crypts of the normal mucosa. In addition, the adenomatous glands show the presence of cigar-shaped nuclei extending beyond the basal third of the columnar epithelium. OCM images correlate well with histology and demonstrate the ability to identify key histologic features of normal and pathologic tissues.

4.3 Line Scan Full-field OCM

In addition to continuing research on OCM using standard methods, we are exploring new techniques which can enable *in vivo* cellular level imaging. OCM is typically implemented by scanning a tightly focused beam in a raster pattern across the sample to generate an en face image at constant depth [122, 124]. *In vivo* OCM imaging on biological samples usually requires the imaging speed larger than several frames per second to minimize the motion artifacts. Therefore, the typical raster scanning design utilizes fast scanning (\sim kHz) in one dimension (X) and slow scanning (\sim Hz) in the other dimension (Y). A significant research effort, including the work described in the above section, has been invested on developing miniaturized fast scanning devices for XY scanning [125-127], but it is challenging to obtain a precise beam steering and small device sizes. Alternative full-field illumination and detection approaches have also been

developed with Linnik type interference microscopes which eliminate the need of beam scanning, and therefore enable rapid and high quality image acquisition [128-134]. However, the sensitivity of the full-field imaging is lower compared with point scanning [135].

We developed a novel, line illumination and detection scheme to perform high-resolution OCM. Line scanning removes the need for fast raster scanning on one axis (X), therefore allowing the use of only a single axis slow scanner (Y) in the sample arm. The line scan OCM system is based on a Linnik type interference microscope with two identical microscope objectives placed in both the sample and reference arms, as shown in Figure 4.10 a. A compact, commercially-available broadband Ti:Sapphire laser was used to generate a broadband spectrum around 800 nm. Line illumination was achieved by using the combination of a spherical focusing lens and a plano-concave cylindrical lens. The light from the sample and reference arms are recombined with the beam splitter and imaged onto the CCD line scan camera. The signal was modulated by moving the reference mirror with a piezoelectric transducer (PZT) and a conventional four-phase demodulation was employed to extract the interference component [129, 130]. *En face* images were generated by transversely scanning the sample along the direction orthogonal to the illumination line with a precision translation stage, and a series of *en face* images at different depths were acquired by translating the sample along the axial direction.

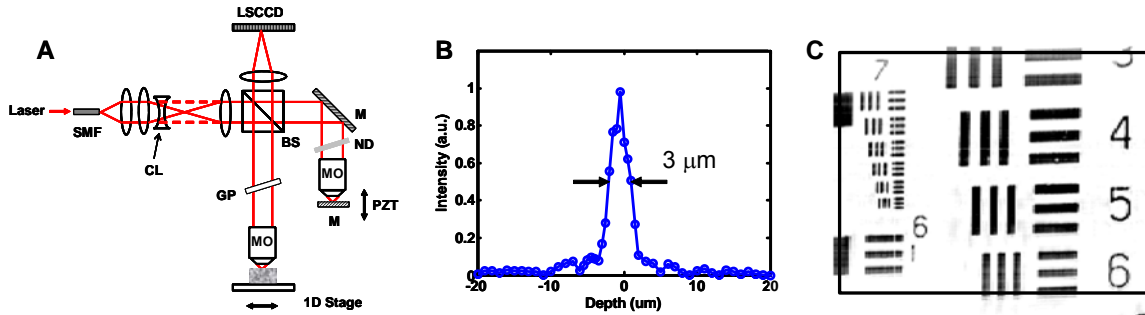


Figure 4.10. A. Schematic of line scan OCM system. B. Point spread function using Ti:Sapphire laser light source. C. Image of resolution chart. Line scan is a new approach which promises higher speeds and reduced scattering compared with full field OCT techniques.

In the preliminary study, the line scan camera was operated at 8 kHz line scan acquisition rate, and the PZT was sinusoidally actuated at 2 kHz and synchronized by the camera. 10 lines from each of the four-quadrant phases were accumulated to increase the signal-to-noise ratio and resulted in an imaging speed of 200 transverse lines/second. Each image consisted of 400 transverse lines and was acquired in 2 seconds. The field of view (FOV) on the camera is 400 pixels, therefore the image was composed of 400 by 400 pixels with the size of 400 μm x 400 μm. Figure 4.10 b shows the axial resolution of the system measured by translating the mirror along the sample arm, and a ~3 μm coherent gate is achieved. Figure 4.10 c demonstrates the coherence gated image of a USAF target on the sample arm. The smallest Group 7, Element 6 bars were able to be resolved, which shows a ~2 μm transverse resolution. The system sensitivity was measured to be 83 dB, which is consistent with previous publications on full-field imaging [135].

Line scan is interesting because it has advantages for endoscopic applications. Although, transmission of the line information through the endoscope would require a fiber optic ribbon, a single axis slow scanning device is easier to implement than a two axis device. Line illumination can reduce the amount of incoherent scattered light and pixel cross-talk compared to full-field illumination, therefore would improve the detection sensitivity. Furthermore, the use of line illumination and line scan cameras promises to enable reduced sensitivity to sample motion compared to full-field detection because the phase sensitive information is acquired more rapidly before phase averaging effects can occur.

5. Functional Brain Imaging with OCT

Brain neural response to cognitive and sensory stimuli is an active area of research. Several imaging techniques have been applied to noninvasively probe neural response to external stimuli. Optical imaging is uniquely sensitive to neuronal and vascular responses to brain activation, both invasively [93, 136] and non-invasively [94], and can contribute to understanding the neuro-vascular relationship [137]. Currently most of the optical imaging presents the two-dimensional en face maps of brain activation [138]. Depth-resolved images can be achieved by optical tomography, but the depth resolution is limited to $\sim 100\ \mu\text{m}$ [139]. OCT can provide depth-resolved, micron-resolution images in vivo and in real time. OCT can also provide three-dimensional volumetric imaging with high spatial resolution.

Several studies exist to date which use OCT to study functional activation in neuronal tissues. Maheswari, et al. showed depth resolved stimulus specific profiles of slow processes during functional activation in the cat visual cortex [99]. They attributed these signals to variation in scattering due to localized structural changes such as capillary dilation and cell swelling. Lazebnik, et al. subsequently performed a simple measurement of scattering changes corresponding to fast and slow signals triggered by action potential propagation in the sea slug abdominal ganglion [97]. Satomura et al. observed the delayed swelling of the cortical surface in the somatosensory cortex following the electrical stimulation of the rat hind paw [140], and Seki, et al. measured the cross-sectional profiles of blood flow velocity in the rat pial microvessels and their temporal changes [141]. Ooi, et al. examined the neural plasticity in response to peripheral neuropathic pain in mice in vivo using OCT [142]. Other studies have also investigated precise measurement of nerve axon displacement using low coherence interferometry methods [143].

Our collaborative group is investigating OCT to measure subsurface scattering changes due to functional activation in the rat somatosensory cortex. Simultaneous OCT and video microscopy imaging were performed and the system diagram is shown in Figure 5.1. The OCT system operates at 1060 nm center wavelength using an Nd:Glass laser generating ~ 100 fs pulses. The laser output is coupled into a standard HI-1060 single mode fiber and the nonlinear effects in the single mode optical fiber broaden the optical spectrum to ~ 40 nm, which results in an axial resolution of $\sim 18\ \mu\text{m}$ in air (corresponding to $13\ \mu\text{m}$ in tissue). In the reference arm, a delay scanning at ~ 1150 Hz is performed and images of ~ 380 transverse pixels are acquired at 3 frames per second. The sample beam is focused to a spot size of $\sim 40\ \mu\text{m}$ and positioned on the rat cortex using an XY scanning pair of galvanometers. The system allows simultaneous imaging with the video microscopy system. The measured system sensitivity from a single high reflector was >95 dB with ~ 14 mW illumination on the sample.

The video microscopy technique illuminates the cortex at 570 nm and images scattered light onto a two-dimensional CCD camera. Changes in cortical reflectivity are measured in response to functional activation. The reflectivity changes at this wavelength are primarily due to change in the total hemoglobin concentration. The video microscopy method is used in this experiment to localize and characterize the functional activation region for placement of the OCT beam.

Forepaw stimulation is performed using 20 second stimulation blocks. Each block consists of 1 second of pre-stimulus period followed by 4 seconds of stimulation with ~1.8 mA pulses at 3 Hz. A 15 second post-stimulus period is then provided to allow full recovery of the excitable tissues to baseline. The stimulus block is repeated 60 times during data acquisition over a 20 minute period. Block averaged signals are then computed to reduce the effects of physiologic noise in the measurements. For data processing, digitized OCT images are converted from log to linear.

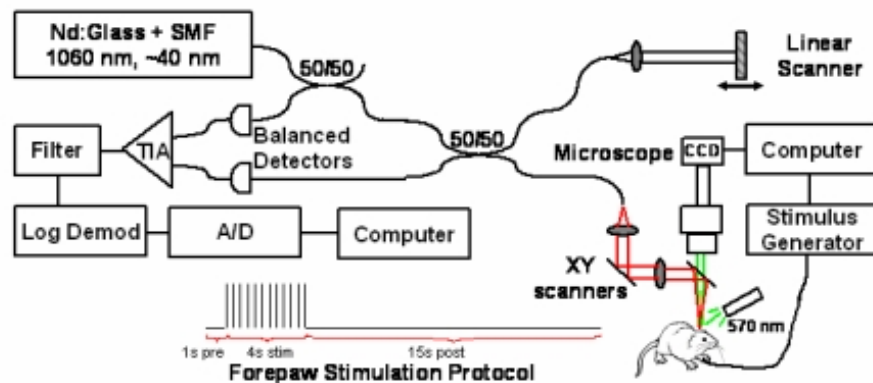


Figure 5.1. Schematic diagram of simultaneous OCT and video microscopy system for measuring functional activation in the rat cortex. The forepaw stimulation protocol used in the experiments is also shown here.

All experiments were conducted according to protocols approved by the Committee on Animal Care at the Massachusetts Institute of Technology and the Animal Care Committee at the Massachusetts General Hospital. Rats were anesthetized with urethane and immobilized in a stereotaxis before beginning the cranial window preparation. An area of skull overlying the primary somatosensory cortex on the contralateral side of the stimulated forepaw was thinned with a dental burr until transparent. Thickness was measured with OCT to be 100-200 μm .

Figure 5.2 shows representative OCT imaging of rat brain structures. OCT cross-sectional images are exactly co-registered to the en face images provided by video microscopy. The structures in rat brain including the skull (S), dura (D), cortex (C), and subsurface vessels (V) are discernable. The skull appears patchy with a highly scattering layer thought to be the dura separating it from the subarachnoid space and the cortex. Large surface cortical vessels can be seen clearly.

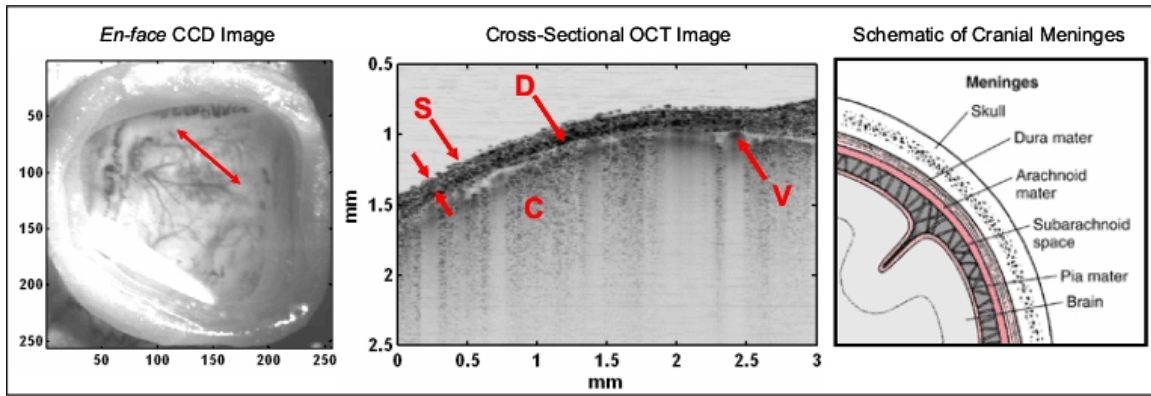


Figure 5.2. Left: *en-face* CCD view of rat brain and vascular pattern through cranial window. Red arrow denotes the OCT imaging plane. Middle: cross-sectional OCT image of rat brain showing detailed structures including skull (S), dura (D), cortex (C), and subsurface vessels (V). Right: schematics of brain anatomy.

The OCT functional signal is shown in Figure 5.3. The signal is computed by dividing each time point in the stimulus and post-stimulus periods by the mean of the pre-stimulus period. The signal is then averaged over all 60 blocks in the data collection period. The time window chosen for plotting Figure 5.3C corresponds to mean of the stimulus period. Several local regions of interest are chosen from the images and the corresponding time courses are plotted in Figure 3D. The time courses stay at baseline during the pre-stimulus period, begin rising ~1 second after the onset of stimulus, and continue to rise until 1-2 seconds after the cessation of the stimulus. The time course returns to baseline after reaching its maximum. The response time course varies in amplitude from region to region. For the most part, the trend of the response is uniform with slight variation in time to peak response. The time course of the response is similar to the response observed with the video microscopy suggesting that the OCT signal change may arise from changes in total hemoglobin concentration.

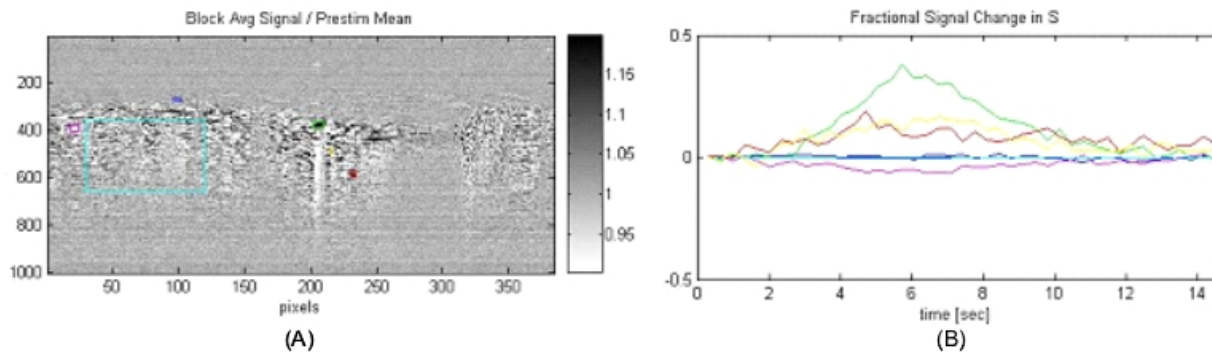


Figure 5.3. Representative OCT imaging results of functional activation in the rat brain. (A) OCT functional activation image. (B) Functional signal time course in region of interests denoted by different colors.

We demonstrated that OCT can image the neuro-vascular response to somatosensory stimulation in the rat. The dominant signal grows over the 4 seconds of the fore-paw electrical stimulus and then requires ~5 seconds to recover to the baseline. The time course of the OCT response correlates well with video microscopy suggesting that this OCT signal may reflect changes in red blood cell density, although neuronal swelling can not be ruled out at this point. Localized regions of strong signal increases were identified that are characteristic of blood vessels. In the parenchyma, smaller signal increases and decreases were observed. This is consistent with previous observations of increases and decreases in red blood cell density in the capillaries during brain activation. Further work is necessary to confirm the origin of this functional signal. These results suggest that OCT could have an important role in future studies of the functional neurovascular response. In a more general context, the integration of structural and functional imaging in ophthalmology and brain sciences promises to enhance fundamental understanding of diseases pathogenesis as well as develop more sensitive markers for early diagnosis and assessment of disease progression.

Publications supported by AFOSR Contract No. FA-9550-04-1-0046

1. D.C. Adler, T.H. Ko, and J.G. Fujimoto, Speckle reduction in optical coherence tomography images by use of a spatially adaptive wavelet filter. *Optics Letters*, 29(24), 2878-80, 2004.
2. A. Chan, J.S. Duker, J.S. Schuman, and J.G. Fujimoto, Stage 0 macular holes: Observations by optical coherence tomography. *Ophthalmology*, 111(11), 2027-32, 2004.
3. P.R. Herz, Y. Chen, A.D. Aguirre, J.G. Fujimoto, H. Mashimo, J. Schmitt, A. Koski, J. Goodnow, and C. Petersen, Ultrahigh resolution optical biopsy with endoscopic optical coherence tomography. *Optics Express*, 12(15), 3532-3542, 2004.
4. P.R. Herz, Y. Chen, A.D. Aguirre, K. Schneider, P. Hsiung, J.G. Fujimoto, K. Madden, J. Schmitt, J. Goodnow, and C. Petersen, Micromotor endoscope catheter for in vivo, ultrahigh-resolution optical coherence tomography. *Optics Letters*, 29(19), 2261-3, 2004.
5. P.L. Hsiung, Y. Chen, T.H. Ko, J.G. Fujimoto, C.J.S. de Matos, S.V. Popov, J.R. Taylor, and V.P. Gapontsev, Optical coherence tomography using a continuous-wave, high-power, raman continuum light source. *Optics Express*, 12(22), 5287-5295, 2004.
6. T.H. Ko, D.C. Adler, J.G. Fujimoto, D. Mamedov, V. Prokhorov, V. Shidlovski, and S. Yakubovich, Ultrahigh resolution optical coherence tomography imaging with a broadband superluminescent diode light source. *Optics Express*, 12(10), 2004.
7. T.H. Ko, J.G. Fujimoto, J.S. Duker, L.A. Paunescu, W. Drexler, C.R. Bauman, C.A. Puliafito, E. Reichel, A.H. Rogers, and J.S. Schuman, Comparison of ultrahigh- and standard-resolution optical coherence tomography for imaging macular hole pathology and repair. *Ophthalmology*, 111(11), 2033-43, 2004.
8. N. Nishizawa, Y. Chen, P. Hsiung, E.P. Ippen, and J.G. Fujimoto, Real-time, ultrahigh-resolution, optical coherence tomography with an all-fiber, femtosecond fiber laser continuum at 1.5 microm. *Opt Lett*, 29(24), 2846-8, 2004.
9. L. Pantanowitz, P.L. Hsiung, T.H. Ko, K. Schneider, P.R. Herz, J.G. Fujimoto, S. Raza, and J.L. Connolly, High-resolution imaging of the thyroid gland using optical coherence tomography. *Head Neck*, 26(5), 425-34, 2004.

10. L.A. Paunescu, J.S. Schuman, L.L. Price, P.C. Stark, S. Beaton, H. Ishikawa, G. Wollstein, and J.G. Fujimoto, Reproducibility of nerve fiber thickness, macular thickness, and optic nerve head measurements using stratusoct. *Invest Ophthalmol Vis Sci*, 45(6), 1716-24, 2004.
11. W.P. Roach, C.P. Cain, D.G. Narayan, G.D. Noojin, S.A. Boppart, R. Birngruber, J.G. Fujimoto, and C.A. Toth, Retinal response of macaca mulatta to picosecond laser pulses of varying energy and spot size. *J Biomed Opt*, 9(6), 1288-96, 2004.
12. J. Rogowska, N.A. Patel, J.G. Fujimoto, and M.E. Brezinski, Optical coherence tomographic elastography technique for measuring deformation and strain of atherosclerotic tissues. *Heart*, 90(5), 556-62, 2004.
13. S.G. Schuman, E. Hertzmark, J.G. Fujimoto, and J.S. Schuman, Wavelength independence and interdevice variability of optical coherence tomography. *Ophthalmic Surg Lasers Imaging*, 35(4), 316-20, 2004.
14. P.C. Wagenblast, T.H. Ko, J.G. Fujimoto, and F.X. Kaertner, Ultrahigh-resolution optical coherence tomography with a diode-pumped broadband cr^{3+} :LiCaF laser. *Optics Express*, 12(14), 2004.
15. M. Wojtkowski, V.J. Srinivasan, T.H. Ko, J.G. Fujimoto, A. Kowalczyk, and J.S. Duker, Ultrahigh-resolution, high-speed, fourier domain optical coherence tomography and methods for dispersion compensation. *Optics Express*, 12(11), 2004.
16. G. Wollstein, J.S. Schuman, L.L. Price, A. Aydin, S.A. Beaton, P.C. Stark, J.G. Fujimoto, and H. Ishikawa, Optical coherence tomography (oct) macular and peripapillary retinal nerve fiber layer measurements and automated visual fields. *Am J Ophthalmol*, 138(2), 218-25, 2004.
17. X. Li, S. Martin, C. Pitris, R. Ghanta, D.L. Stamper, M. Harman, J.G. Fujimoto, and M.E. Brezinski, "High-resolution optical coherence tomographic imaging of osteoarthritic cartilage during open knee surgery," *Arthritis Res. Ther.* **7**, R318-R328, January 2005.
18. E. Ergun, B. Hermann, M. Wirtisch, A. Unterhuber, T.H. Ko, H. Sattmann, C. Scholda, J.G. Fujimoto, M. Stur, and W. Drexler, "Assessment of central visual function in Stargardt's Disease/Fundus flavimaculatus with ultrahigh-resolution optical coherence tomography," *Invest. Ophthalmol. and Vis. Sci.* **46**, 310-316, January 2005.
19. N.A. Patel, J. Zoeller, D.L. Stamper, J.G. Fujimoto, and M.E. Brezinski, "Monitoring osteoarthritis in the rat model using optical coherence tomography," *IEEE Trans. Med. Imaging* **24**, 155-159, February 2005.
20. G. Wollstein, L.A. Paunescu, T.H. Ko, J.G. Fujimoto, A. Kowalewicz, I. Hartl, S. Beaton, H. Ishikawa, C. Mattox, O. Singh, J. Duker, W. Drexler, and J.S. Schuman, "Ultrahigh-resolution optical coherence tomography in glaucoma," *Ophthalmology* **112**, 229-237, February 2005.
21. N. Patel, X. Li, D.L. Stamper, J.G. Fujimoto, and M.E. Brezinski, "Using optical coherence tomography to guide articular cartilage ablation," *Am. J. Orthop.* **34** 111-115, March 2005.
22. G. Wollstein, J.S. Schuman, L.L. Price, A. Aydin, P.C. Stark, E. Hertzmark, E. Lai, H. Ishikawa, C. Mattox, J.G. Fujimoto, and L.A. Paunescu, "Optical coherence tomography longitudinal evaluation of retinal nerve fiber layer thickness in glaucoma," *Arch. Ophthalmol.* **123**, 464-470, April 2005.

23. R. Huber, M. Wojtkowski, K. Taira, J.G. Fujimoto, and K. Hsu, "Amplified, frequency swept lasers for frequency domain reflectometry and OCT imaging: design and scaling principles," *Opt. Exp.* **13**, 3513-3528, May 2005.
24. H. Ishikawa, D.M. Stein, G. Wollstein, S. Beaton, J.G. Fujimoto, and J.S. Schuman, "Macular segmentation with optical coherence tomography," *Invest. Ophthalmol. Vis. Sci.* **46**, 2012-2017, June 2005.
25. M. Wojtkowski, P.I. Lapin, D.S. Mamedov, J.G. Fujimoto, and S.D. Yakubovich, "Multichannel extremely broadband near-IR radiation sources for optical coherence tomography," *Kvantovaya Elektronika, Moskva* **35**, 667-669, July 2005.
26. M. Wojtkowski, V. Srinivasan, J.G. Fujimoto, T. Ko, J.S. Schuman, A. Kowalczyk, and J.S. Duker, "Three-dimensional retinal imaging with high-speed ultrahigh-resolution optical coherence tomography," *Ophthalmology* **112**, 1734-1746, October 2005.
27. P.L. Hsiung, L. Pantanowitz, A.D. Aguirre, Y. Chen, D. Phatak, T.H. Ko, S. Bourquin, S.J. Schmitt, S. Raza, J.L. Connolly, H. Mashimo, and J.G. Fujimoto, "Ultrahigh resolution and three-dimensional optical coherence tomography ex vivo imaging of the large and small intestines," *Gastrointest. Endosc.* **62**, 561-574, October 2005.
28. T.H. Ko, J.G. Fujimoto, J.S. Schuman, L.A. Paunescu, A.M. Kowalevich, I. Hartl, W. Drexler, G. Wollstein, H. Ishikawa, and J.S. Duker, "Comparison of ultrahigh and standard resolution optical coherence tomography for imaging macular pathology," *Ophthalmology* **112**, 1922-1935, November 2005.
29. A.J. Witkin, T.H. Ko, J.G. Fujimoto, J.S. Schuman, and J.S. Duker, "Ultrahigh resolution optical coherence tomography of birdshot retinochoroidopathy," *Br. J. Ophthalmol.* **89**, 1660-1661, December 2005.
30. P.L. Hsiung, P.R. Nambiar, and J.G. Fujimoto, "Effect of tissue preservation on imaging using ultrahigh resolution optical coherence tomography," *J. Biomed. Opt.* **10**, 064033-1 – 064033-9, November/December 2005.
31. T.A. Scheufile, A.J. Witkin, L.S. Schocket, A.H. Rogers, J.S. Schuman, T.H. Ko, J.G. Fujimoto, E. Reichel, and J.S. Duker, "Photoreceptor atrophy in acute posterior multifocal placoid pigment epitheliopathy demonstrated by optical coherence tomography," *Retina* **25**, 1109-1112, December 2005.
32. M.G. Wirtitsch, E. Ergun, B. Hermann, A. Unterhuber, M. Stur, C. Scholda, H. Sattmann, T.H. Ko, J.G. Fujimoto, and W. Drexler, "Ultrahigh resolution optical coherence tomography in macular dystrophy," *Am. J. Ophthalmol.* **140**, 976-983, December 2005.
33. R. Huber, M. Wojtkowski, J.G. Fujimoto, J.Y. Jiang, and A.E. Cable, "Three-dimensional and C-mode OCT imaging with a compact, frequency swept laser source at 1300 nm," *Optics Exp.* **13**, 10523-10538, December 2005.
34. L.A. Paunescu, T.H. Ko, J.S. Duker, A. Chan, W. Drexler, J.S. Schuman, and J.G. Fujimoto, "Idiopathic juxtafoveal retinal telangiectasis: New findings by ultrahigh-resolution optical coherence tomography," *Ophthalmology* **113**, 48-57, January 2006.
35. A. Chan, J.S. Duker, T.H. Ko, J.S. Schuman, and J.G. Fujimoto, "Ultrahigh resolution optical coherence tomography of retinal pigment epithelial tear following blunt trauma," *Arch. Ophthalmol.* **124**, 281-283, February 2006.
36. C.G. Pieroni, A.J. Witkin, T.H. Ko, J.G. Fujimoto, A. Chan, J.S. Schuman, H. Ishikawa, E. Reichel, and J.S. Duker, "Ultrahigh resolution optical coherence tomography in non-exudative age related macular degeneration," *Br. J. Ophthalmol.* **90**, 191-197, February 2006.

37. A. Chan, J.S. Duker, T.H. Ko, J.G. Fujimoto, and J.S. Schuman, "Normal macular thickness measurements in healthy eyes using Stratus optical coherence tomography," *Arch. Ophthalmol.* **124**, 193-198, February 2006.
38. D.M. Stein, H. Ishikawa, R. Hariprasad, G. Wollstein, R.J. Noecker, J.G. Fujimoto, and J.S. Schuman, "A new quality assessment parameter for optical coherence tomography," *Br. J. Ophthalmol.* **90**, 186-190, February 2006.
39. A.D. Aguirre, N. Nishizawa, J.G. Fujimoto, W. Seitz, M. Lederer, and D. Kopf, "Continuum generation in a novel photonic crystal for ultrahigh resolution optical coherence tomography at 800 nm and 1300 nm," *Opt. Exp.* **14**, 1145-1160, February 2006.
40. A.J. Witkin, T.H. Ko, J.G. Fujimoto, J.S. Schuman, C.R. Bauman, A.H. Rogers, E. Reichel, and J.S. Duker, "Redefining lamellar holes and the vitreomacular interface: An ultrahigh-resolution optical coherence tomography study," *Ophthalmology* **113**, 388-397, March 2006.
41. S.D. Giattina, B.K. Courtney, P.R. Herz, M. Harman, S. Shortkroff, D.L. Stamper, B. Lui, J.G. Fujimoto, and M.E. Brezinski, "Assessment of coronary plaque collagen with polarization sensitive optical coherence tomography (PS-OCT)," *Intl. J. Cardiol.* **107**, 400-409, March 2006.
42. R. Huber, M. Wojtkowski, and J.G. Fujimoto, "Fourier domain mode locking (FDML): A new laser operating regime and applications for optical coherence tomography," *Opt. Exp.* **14**, 3225-3237, April 2006.
43. S.B. Adams, Jr., P.R. Herz, D.L. Stamper, M.J. Roberts, S. Bourquin, N.A. Patel, K. Schneider, S.D. Martin, S. Shortkroff, J.G. Fujimoto, and M.E. Brezinski, "High-resolution imaging of progressive articular cartilage degeneration," *J. Orthop. Res.* **24**, 708-715, April 2006.
44. L.S. Schocket, A.J. Witkin, J.G. Fujimoto, T.H. Ko, J.S. Schuman, A.H. Rogers, C. Bauman, E. Reichel, and J.S. Duker, "Ultrahigh-resolution optical coherence tomography in patients with decreased visual acuity after retinal detachment repair," *Ophthalmology* **113**, 666-672, April 2006.
45. A.J. Witkin, A.H. Rogers, T.H. Ko, J.G. Fujimoto, J.S. Schuman, and J.S. Duker, "Optical coherence tomography demonstration of macular infarction in sickle cell retinopathy," *Arch. Ophthalmol.* **124**, 746-747, May 2006.
46. T.H. Ko, A.J. Witkin, J.G. Fujimoto, A. Chan, A.H. Rogers, C.R. Bauman, J.S. Schuman, W. Drexler, E. Reichel, and J.S. Duker, "Ultrahigh-resolution optical coherence tomography of surgically closed macular holes," *Arch. Ophthalmol.* **124**, 827-836, June 2006.
47. A. Chan, J.S. Duker, H. Ishikawa, T.H. Ko, J.S. Schuman, and J.G. Fujimoto, "Quantification of photoreceptor layer thickness in normal eyes using optical coherence tomography," *Retina* **26**, 655-60, July-August 2006.
48. V.J. Srinivasan, M. Wojtkowski, J.G. Fujimoto, and J.S. Duker, "In vivo measurement of retinal physiology with high-speed ultrahigh resolution optical coherence tomography," *Opt. Lett.*, **31**, 2308-2310, August 2006.
49. R. Huber, D.C. Adler, and J.G. Fujimoto, "Buffered Fourier domain mode locking: unidirectional swept laser sources for optical coherence tomography imaging at 370,000 lines/s," *Opt. Lett.*, **31**, 2975-2977, October 2006.
50. V.J. Srinivasan, M. Wojtkowski, A.J. Witkin, T.H. Ko, M. Carvalho, J.S. Schuman, A. Kowalczyk, J.S. Duker, and J.G. Fujimoto, "High-definition and three-dimensional

- imaging of macular pathologies with high-speed, ultrahigh resolution optical coherence tomography,” *Ophthalmology*, **113**, 2054.e1-e14, November 2006.
51. L. Kagemann, G. Wollstein, H. Ishikawa, M.L. Gabrielle, V.J. Srinivasan, M. Wojtkowski, J.S. Duker, J.G. Fujimoto, and J.S. Schuman, “Persistence of Cloquet’s canal in normal healthy eyes,” *Am. J. Ophthalmol.* **142**, 862-864, November 2006.
 52. C. Scholda, M. Wirtitsch, B. Hermann, A. Unterhuber, E. Ergun, H. Sattmann, T.H. Ko, J.G. Fujimoto, A.F. Fercher, M. Stur, U. Schmidt-Erfuth, and W. Drexler, “Ultrahigh resolution optical coherence tomography of macular holes,” *Retina* **26**, 1034-1041, November-December 2006.
 53. A.J. Witkin, T.H. Ko, J.G. Fujimoto, J.S. Schuman, E. Reichel, and J.S. Duker, “Vitreofoveal attachment causing metamorphopsia: An ultrahigh-resolution optical coherence tomography finding,” *Retina* **26**, 1085-1087, November-December 2006.
 54. V.J. Srinivasan, T.H. Ko, M. Wojtkowski, M. Carvalho, A. Clermont, S.-E. Bursell, Q.H. Song, J. Lem, J.S. Duker, J.S. Schuman, and J.G. Fujimoto, “Noninvasive volumetric imaging and morphometry of the rodent retina with high-speed, ultrahigh resolution OCT,” *Invest. Ophthalmol. and Vis. Sci.* **47**, 5522-5528, December 2006.
 55. A.J. Witkin, T.H. Ko, J.G. Fujimoto, A. Chan, W. Drexler, J.S. Schuman, E. Reichel, and J.S. Duker, “Ultrahigh-resolution optical coherence tomography assessment of photoreceptors in retinitis pigmentosa and related diseases,” *Am. J. Ophthalmol.* **142**, 945-952, December 2006.
 56. A.D. Aguirre, Y. Chen, J.G. Fujimoto, L. Ruvinskaya, A. Devor, and D.A. Boas, “Depth-resolved imaging of functional activation in the rat cerebral cortex using optical coherence tomography,” *Opt. Lett.* **31**, 3459-3461, December 2006.
 57. B.K. Monson, P.B. Greenberg, E. Greenberg, J.G. Fujimoto, V.J. Srinivasan, and J.S. Duker, “High-speed, ultra-high-resolution optical coherence tomography of acute macular neuroretinopathy,” *Br. J. Ophthalmol.* **91**, 119-120, January 2007.
 58. B.-B. Gao, A. Clermont, S. Rook, S.J. Fonda, V.J. Srinivasan, M. Wojtkowski, J.G. Fujimoto, R.L. Avery, P.G. Arrigg, S.-E. Bursell, L.P. Aiello, and E.P. Feener, “Extracellular carbonic anhydrase mediates hemorrhagic retinal and cerebral vascular permeability through prekallikrein activation,” *Nature Med.*, **13**, 181-188, February 2007.
 59. V.J. Srinivasan, R. Huber, I. Gorczynska, J.G. Fujimoto, J.Y. Jiang, P. Riesen, and A.E. Cable, “High-speed, high-resolution optical coherence tomography retinal imaging with a frequency-swept laser at 850nm,” *Opt. Lett.* **32**, 361-363, February 2007.
 60. D.C. Adler, R. Huber, and J.G. Fujimoto, “Phase sensitive optical coherence tomography at up to 370,000 lines per second using buffered Fourier domain mode-locked lasers,” *Opt. Lett.* **32**, 626-628, March 2007.
 61. A.D. Aguirre, P.R. Herz, Y. Chen, J.G. Fujimoto, W. Piyawattanametha, L. Fan, and M.C. Wu, “Two-axis MEMS scanning catheter for ultrahigh resolution three-dimensional and *en face* imaging,” *Opt. Exp.* **15**, 2445-2451, March 2007.
 62. M.Y. Kahook, R.J. Noecker, H. Ishikawa, G. Wollstein, L. Kagemann, M. Wojtkowski, J.S. Duker, V.J. Srinivasan, J.G. Fujimoto, and J.S. Schuman, “Peripapillary schisis in glaucoma patients with narrow angles and increased intraocular pressure,” *Am. J. Ophthalmol.* **143**, 697-699, April 2007.
 63. M.W. Jenkins, D.C. Adler, M. Gargasha, R. Huber, F. Rothenberg, J. Belding, M. Watanabe, D.L. Wilson, J.G. Fujimoto, and A.M. Rollins, “Ultrahigh-speed optical

- coherence tomography imaging and visualization of the embryonic avian heart using a buffered Fourier domain mode locked laser,” *Opt. Exp.* **15**, 6251-6267, May 2007.
64. S.-W. Huang, A.D. Aguirre, R.A. Huber, D.C. Adler, and J.G. Fujimoto, “Swept source optical coherence microscopy using Fourier domain mode-locked laser,” *Opt. Exp.* **15**, 6210-6217, May 2007.
 65. M.H. Nguyen, A.J. Witkin, E. Reichel, T.H. Ko, J.G. Fujimoto, J.S. Schuman, and J.S. Duker, “Microstructural abnormalities in MEWDS demonstrated by ultrahigh resolution optical coherence tomography,” *Retina* **27**, 414-418, April-May 2007.
 66. Y. Chen, P.M. Andrews, A.D. Aguirre, J.M. Schmitt, and J.G. Fujimoto, “High-resolution three-dimensional optical coherence tomography imaging of kidney microanatomy ex vivo,” *J. Biomed. Opt.* **12**, 034008-1—034008-7, May/June, 2007.
 67. J.A. Rodriguez-Padilla, T.R. Hedges, III, B. Monson, V. Srinivasan, M. Wojtkowski, E. Reichel, J.S. Duker, J.S. Schuman, and J.G. Fujimoto, “High-speed, ultra-high-resolution optical coherence tomography findings in hydroxychloroquine retinopathy,” *Arch. Ophthalmol.* **125**, 775-780, June 2007.
 68. M.L. Gabriele, H. Ishikawa, G. Wollstein, R.A. Bilonick, L. Kagemann, M. Wojtkowski, V.J. Srinivasan, J.G. Fujimoto, J.S. Duker, and J.S. Schuman, “Peripapillary nerve fiber layer thickness profile determined with high speed, ultrahigh resolution optical coherence tomography high-density scanning,” *Invest. Ophthalmol. Vis. Sci.* **48**, 3154-3160, July 2007.
 69. R. Huber, D.C. Adler, V.J. Srinivasan, I. Gorczynska, and J.G. Fujimoto, “Fourier domain mode locking at 1050 nm for ultra-high-speed optical coherence tomography of the human retina at 236,000 axial scans per second,” *Opt. Lett.* **32**, 2049-2051, July 2007.
 70. Y. Chen, S.-W. Huang, A.D. Aguirre, and J.G. Fujimoto, “High-resolution line-scanning optical coherence microscopy,” *Opt. Lett.* **32**, 1971-1973, July 2007.
 71. J.S. Schuman, T. Pedut-Kloizman, H. Pakter, N. Wang, V. Guedes, L. Huang, L. Pieroth, W. Scott, M.R. Hee, J.G. Fujimoto, H. Ishikawa, R.A. Bilonick, L. Kagemann, and G. Wollstein, “Optical coherence tomography and histological measurements of nerve fiber layer thickness in normal and glaucomatous monkey eyes,” *Invest. Ophthalmol. and Vis. Sci.* **48**, 3645-3654, August 2007.
 72. M. Szkulmowski, M. Wojtkowski, B. Sikorski, T. Bajraszewski, V.J. Srinivasan, A. Szkulmoska, J.J. Kaluzny, J.G. Fujimoto, and A. Kowalczyk, “Analysis of posterior retinal layers in spectral optical coherence tomography images of the normal retina and retinal pathologies,” *J. Biomed. Opt.* **12**, 041207-1 – 11, July/August 2007.
 73. L. Kagemann, G. Wollstein, M. Wojtkowski, H. Ishikawa, K.A. Townsend, M.L. Gabriele, V.J. Srinivasan, J.G. Fujimoto, and J.S. Schuman, “Spectral oximetry assessed with high-speed ultra-high-resolution optical coherence tomography,” *J. Biomed. Opt.* **12**, 04212-1—8, July/August 2007.
 74. V. Christopoulos, L. Kagemann, G. Wollstein, H. Ishikawa, M.L. Gabriele, M. Wojtkowski, V. Srinivasan, J.G. Fujimoto, J.S. Duker, D.K. Dhaliwal, and J.S. Schuman, “In vivo corneal high-speed, ultra-high-resolution optical coherence tomography,” *Arch. Ophthalmol.* **125**, 1027-1035, August 2007.
 75. P.L. Hsiung, D.R. Phatak, Y.Chen, A.D. Aguirre, J.G. Fujimoto, and J.L. Connolly, “Benign and malignant lesions in the human breast depicted with ultrahigh resolution and three-dimensional optical coherence tomography,” *Radiology* **244**, 865-874, September 2007.

76. M.K. Yoon, R.W. Chen, T.R. Hedges, III, V.J. Srinivasan, I. Gorczynska, J.G. Fujimoto, M. Wojtkowski, J.S. Schuman, and J.S. Duker, "High-speed, ultrahigh resolution optical coherence tomography of the retina in Hunter syndrome," *Ophthalmic Surg. Lasers Imaging* **38**, 423-428, September/October 2007.
77. L.A. Kranendonk, X. An, A. Caswell, R.E. Herold, S.T. Sanders, R. Huber, J.G. Fujimoto, Y. Okura, and Y. Urata, "High speed engine gas thermometry by Fourier-domain mode-locked laser absorption spectroscopy," *Opt. Exp.* **15**, 15115-15128, October 2007.
78. A.J. Witkin, M. Wojtkowski, E. Reichel, V.J. Srinivasan, J.G. Fujimoto, J.S. Schuman, and J.S. Duker, "Photoreceptor disruption secondary to posterior vitreous detachment as visualized using high-speed ultrahigh-resolution optical coherence tomography," *Arch. Ophthalmol* **125**, 1579-1580, November 2007.
79. D.C. Adler, J. Stenger, I. Gorczynska, H. Lie, T. Hensick, R. Spronk, S. Wolohojian, N. Khandekar, J.Y. Jiang, S. Barry, A.E. Cable, R. Huber, and J.G. Fujimoto, "Comparison of three-dimensional optical coherence tomography and high resolution photography for art conservation studies," *Opt. Exp.* **15**, 15972-15986, November 2007.
80. Y. Chen, A.D. Aguirre, P.-L. Hsiung, S. Desai, P.R. Herz, M. Pedrosa, Q. Huang, M. Figueiredo, S.-W. Huang, A. Koski, J.M. Schmitt, J.G. Fujimoto, and H. Mashimo, "Ultrahigh resolution optical coherence tomography of Barrett's esophagus: preliminary descriptive clinical study correlating images with histology," *Endoscopy* **39**, 599-605, 2007.
81. L.A. Kranendonk, R. Huber, J.G. Fujimoto, and S.T. Sanders, "Wavelength-agile H₂O absorption spectrometer for thermometry of general combustion gases," *Proc. Comb. Inst.* **31**, 783-790, 2007.
82. D.C. Adler, Y. Chen, R. Huber, J. Schmitt, J. Connolly, and J.G. Fujimoto, "Three-dimensional endoscopy using optical coherence tomography," *Nat. Photon.* **1**, 709-716, December 2007.
83. W. Drexler and J.G. Fujimoto, "State-of-the-art retinal optical coherence tomography," *Prog. Retin. Eye Res.* **27**, 45-88, January 2008.
84. P.M. Andrews, Y. Chen, M.L. Onozato, S.-W. Huang, D.C. Adler, R.A. Huber, J. Jiang, S.E. Barry, A.E. Cable, and J.G. Fujimoto, "High-resolution optical coherence tomography imaging of the living kidney," *Lab. Invest.*, epub February 11, 2008.
85. Y. Chen, A.D. Aguirre, P.-L. Hsiung, S.-W. Huang, H. Mashimo, J.M. Schmitt, and J.G. Fujimoto, "Effects of axial resolution improvement on optical coherence tomography (OCT) imaging of gastrointestinal tissues," *Opt. Exp.* **16**, 2469-2485, February 18, 2008.
86. D.C. Adler, S.-W. Huang, R. Huber, and J.G. Fujimoto, "Photothermal detection of gold nanoparticles using phase-sensitive optical coherence tomography," *Opt. Exp.* **16**, 4376-4393, March 17, 2008.
87. V.J. Srinivasan, B.K. Monson, M. Wojtkowski, I. Gorczynska, R. Chen, J.S. Duker, J.S. Schuman, and J.G. Fujimoto, "Characterization of outer retinal morphology with high-speed, ultrahigh resolution optical coherence tomography," *Invest. Ophthalmol. and Vis. Sci.*, forthcoming.

References

- [1] D. Huang, E. A. Swanson, C. P. Lin, J. S. Schuman, W. G. Stinson, W. Chang, M. R. Hee, T. Flotte, K. Gregory, C. A. Puliafito, and J. G. Fujimoto, "Optical coherence tomography," *Science*, vol. 254, pp. 1178-1181, 1991/11/22 1991.
- [2] J. G. Fujimoto, "Optical coherence tomography for ultrahigh resolution in vivo imaging," *Nature Biotechnology*, vol. 21, pp. 1361-1367, Nov 2003.
- [3] J. G. Fujimoto, M. E. Brezinski, G. J. Tearney, S. A. Boppart, B. Bouma, M. R. Hee, J. F. Southern, and E. A. Swanson, "Optical biopsy and imaging using optical coherence tomography," *Nature Medicine*, vol. 1, pp. 970-972, Sep 1995.
- [4] M. E. Brezinski, G. J. Tearney, B. E. Bouma, J. A. Izatt, M. R. Hee, E. A. Swanson, J. F. Southern, and J. G. Fujimoto, "Optical coherence tomography for optical biopsy. Properties and demonstration of vascular pathology," *Circulation*, vol. 93, pp. 1206-13, Mar 15 1996.
- [5] J. G. Fujimoto, C. Pitris, S. A. Boppart, and M. E. Brezinski, "Optical coherence tomography: an emerging technology for biomedical imaging and optical biopsy," *Neoplasia*, vol. 2, pp. 9-25, Jan-Apr 2000.
- [6] W. Drexler, D. Stamper, C. Jesser, X. Li, C. Pitris, K. Saunders, S. Martin, M. B. Lodge, J. G. Fujimoto, and M. E. Brezinski, "Correlation of collagen organization with polarization sensitive imaging of in vitro cartilage: implications for osteoarthritis," *The Journal of rheumatology*, vol. 28, pp. 1311-8, Jun 2001.
- [7] W. Drexler, U. Morgner, R. K. Ghanta, F. X. Kärtner, J. S. Schuman, and J. G. Fujimoto, "Ultrahigh-resolution ophthalmic optical coherence tomography," *Nature Medicine*, vol. 7, pp. 502-507, Apr 2001.
- [8] W. Drexler, U. Morgner, F. X. Kartner, C. Pitris, S. A. Boppart, X. D. Li, E. P. Ippen, and J. G. Fujimoto, "In vivo ultrahigh-resolution optical coherence tomography," *Optics Letters*, vol. 24, pp. 1221-1223, 1 Sept. 1999 1999.
- [9] W. Drexler, H. Sattmann, B. Hermann, T. H. Ko, M. Stur, A. Unterhuber, C. Scholda, O. Findl, M. Wirtitsch, J. G. Fujimoto, and A. F. Fercher, "Enhanced visualization of macular pathology with the use of ultrahigh-resolution optical coherence tomography," *Archives of Ophthalmology*, vol. 121, pp. 695-706, May 2003.
- [10] W. Drexler, "Ultrahigh-resolution optical coherence tomography," *Journal of Biomedical Optics*, vol. 9, pp. 47-74, 2004/01/ 2004.
- [11] U. Morgner, W. Drexler, F. X. Kartner, X. D. Li, C. Pitris, E. P. Ippen, and J. G. Fujimoto, "Spectroscopic optical coherence tomography," *Optics Letters*, vol. 25, pp. 111-113, 2000/01/15 2000.
- [12] B. Bouma, G. J. Tearney, S. A. Boppart, M. R. Hee, M. E. Brezinski, and J. G. Fujimoto, "High-resolution optical coherence tomographic imaging using a mode-locked Ti:Al₂O₃ laser source," *Optics Letters*, vol. 20, pp. 1486-1488, 1995/07/01 1995.
- [13] I. Hartl, X. D. Li, C. Chudoba, R. K. Hganta, T. H. Ko, J. G. Fujimoto, J. K. Ranka, and R. S. Windeler, "Ultrahigh-resolution optical coherence tomography using continuum generation in an air-silica microstructure optical fiber," *Optics Letters*, vol. 26, pp. 608-610, 2001/05/01 2001.
- [14] A. D. Aguirre, N. Nishizawa, J. G. Fujimoto, W. Seitz, M. Lederer, and D. Kopf, "Continuum generation in a novel photonic crystal fiber for ultrahigh resolution optical coherence tomography at 800 nm and 1300 nm," *Optics Express*, vol. 14, pp. 1145-1160, Feb 6 2006.

- [15] D. E. Spence, P. N. Kean, and W. Sibbett, "60-Fsec Pulse Generation from a Self-Mode-Locked Ti-Sapphire Laser," *Optics Letters*, vol. 16, pp. 42-44, JAN 1 1991.
- [16] J. P. Zhou, G. Taft, C. P. Huang, M. M. Murnane, H. C. Kapteyn, and I. P. Christov, "Pulse Evolution in a Broad-Bandwidth Ti-Sapphire Laser," *Optics Letters*, vol. 19, pp. 1149-1151, AUG 1 1994.
- [17] A. M. Kowalevich, T. R. Schibli, F. X. Kartner, and J. G. Fujimoto, "Ultralow-threshold Kerr-lens mode-locked Ti:Al₂O₃ laser," *Optics Letters*, vol. 27, pp. 2037-2039, 2002.
- [18] B. Cense, N. A. Nassif, T. C. Chen, M. C. Pierce, S.-H. Yun, B. H. Park, B. E. Bouma, G. J. Tearney, and J. F. de Boer, "Ultrahigh-resolution high-speed retinal imaging using spectral-domain optical coherence tomography," *Optics Express*, vol. 12, 2004/05/31 2004.
- [19] T. H. Ko, D. C. Adler, J. G. Fujimoto, D. Mamedov, V. Prokhorov, V. Shidlovski, and S. Yakubovich, "Ultrahigh resolution optical coherence tomography imaging with a broadband superluminescent diode light source," *Optics Express*, vol. 12, pp. 2112-2119, MAY 17 2004.
- [20] A. T. Semenov, V. R. Shidlovski, D. A. Jackson, R. Willsch, and W. Ecke, "Spectral control in multisection AlGaAs SQW superluminescent diodes at 800 nm," *Electronics Letters*, vol. 32, pp. 255-256, FEB 1 1996.
- [21] D. S. Mamedov, V. V. Prokhorov, and S. D. Yakubovich, "Superbroadband high-power superluminescent diode emitting at 920 nm," *Quantum Electronics*, vol. 33, pp. 471-473, JUN 2003.
- [22] B. E. Bouma, G. J. Tearney, I. P. Bilinsky, B. Golubovic, and J. G. Fujimoto, "Self-phase-modulated Kerr-lens mode-locked Cr:forsterite laser source for optical coherence tomography," *Optics Letters*, vol. 21, pp. 1839-1841, 1996/11/15 1996.
- [23] C. Chudoba, J. G. Fujimoto, E. P. Ippen, H. A. Haus, U. Morgner, F. X. Kärtner, V. Scheuer, G. Angelow, and T. Tschudi, "All-solid-state Cr:forsterite laser generating 14 fs pulses at 1.3 μ m," *Optics Letters*, vol. 26, pp. 292-294, 2001.
- [24] F. X. Kärtner, N. Matuschek, T. Schibli, U. Keller, H. A. Haus, C. Heine, R. Morf, V. Scheuer, M. Tilsch, and T. Tschudi, "Design and fabrication of double-chirped mirrors," *Opt. Lett.*, vol. 22, pp. 831-833, 1997.
- [25] P. R. Herz, Y. Chen, A. D. Aguirre, J. G. Fujimoto, H. Mashimo, J. Schmitt, A. Koski, J. Goodnow, and C. Petersen, "Ultrahigh resolution optical biopsy with endoscopic optical coherence tomography," *Optics Express*, vol. 12, pp. 3532-3542, JUL 26 2004.
- [26] P.-L. Hsiung, Y. Chen, T. H. Ko, J. G. Fujimoto, C. J. S. de Matos, S. V. Popov, J. R. Taylor, and V. P. Gapontsev, "Optical coherence tomography using a continuous-wave, high-power, Raman continuum light source," *Optics Express*, vol. 12, 2004/11/01 2004.
- [27] K. L. Corwin, N. R. Newbury, J. M. Dudley, S. Coen, S. A. Diddams, B. R. Washburn, K. Weber, and R. S. Windeler, "Fundamental amplitude noise limitations to supercontinuum spectra generated in a microstructured fiber (vol B 77, pg 269, 2003)," *Applied Physics B-Lasers and Optics*, vol. 77, pp. 467-468, OCT 2003.
- [28] L. Provino, J. M. Dudley, H. Maillotte, N. Grossard, R. S. Windeler, and B. J. Eggleton, "Compact broadband continuum source based on microchip laser pumped microstructured fibre," *Electronics Letters*, vol. 37, pp. 558-560, APR 26 2001.
- [29] A. V. Avdokhin, S. V. Popov, and J. R. Taylor, "Continuous-wave, high-power, in Raman continuum generation holey fibers," *Optics Letters*, vol. 28, pp. 1353-1355, AUG 1 2003.

- [30] T. A. Birks, W. J. Wadsworth, and P. S. Russell, "Supercontinuum generation in tapered fibers," *Optics Letters*, vol. 25, pp. 1415-1417, OCT 1 2000.
- [31] Y. Wang, Y. Zhao, J. S. Nelson, Z. Chen, and R. S. Windeler, "Ultrahigh-resolution optical coherence tomography by broadband continuum generation from a photonic crystal fiber," *Optics Letters*, vol. 28, pp. 182-4, 2003/02/01 2003.
- [32] B. Povazay, K. Bizheva, A. Unterhuber, B. Hermann, H. Sattmann, A. F. Fercher, W. Drexler, A. Apolonski, W. J. Wadsworth, J. C. Knight, P. S. J. Russell, M. Vetterlein, and E. Scherzer, "Submicrometer axial resolution optical coherence tomography," *Optics Letters*, vol. 27, pp. 1800-2, 2002/10/15 2002.
- [33] S. Bourquin, A. D. Aguirre, I. Hartl, P. Hsiung, T. H. Ko, J. G. Fujimoto, T. A. Birks, W. J. Wadsworth, U. Bunting, and D. Kopf, "Ultrahigh resolution real time OCT imaging using a compact femtosecond Nd : Glass laser and nonlinear fiber," *Optics Express*, vol. 11, pp. 3290-3297, DEC 1 2003.
- [34] Y. Wang, J. S. Nelson, Z. Chen, B. J. Reiser, R. S. Chuck, and R. S. Windeler, "Optimal wavelength for ultrahigh-resolution optical coherence tomography," *Optics Express*, vol. 11, 2003/06/16 2003.
- [35] N. Nishizawa, Y. Chen, P. Hsiung, E. P. Ippen, and J. G. Fujimoto, "Real-time, ultrahigh-resolution, optical coherence tomography with an all-fiber, femtosecond fiber laser continuum at 1.5 microm," *Opt Lett*, vol. 29, pp. 2846-8, Dec 15 2004.
- [36] E. A. Swanson, J. A. Izatt, M. R. Hee, D. Huang, C. P. Lin, J. S. Schuman, C. A. Puliafito, and J. G. Fujimoto, "In vivo retinal imaging by optical coherence tomography," *Optics Letters*, vol. 18, pp. 1864-1866, 1993/11/01 1993.
- [37] M. R. Hee, J. A. Izatt, E. A. Swanson, D. Huang, J. S. Schuman, C. P. Lin, C. A. Puliafito, and J. G. Fujimoto, "Optical coherence tomography of the human retina," *Archives of Ophthalmology*, vol. 113, pp. 325-332, Mar 1995.
- [38] A. F. Fercher, C. K. Hitzenberger, G. Kamp, and S. Y. Elzaiat, "Measurement of Intraocular Distances by Backscattering Spectral Interferometry," *Optics Communications*, vol. 117, pp. 43-48, MAY 15 1995.
- [39] G. Hausler and M. W. Lindner, "'Coherence radar" and "spectral radar"-new tools for dermatological diagnosis," *Journal of Biomedical Optics*, vol. 3, pp. 21-31, 1998/01/ 1998.
- [40] R. Leitgeb, C. K. Hitzenberger, and A. F. Fercher, "Performance of Fourier domain vs. time domain optical coherence tomography," *Optics Express*, vol. 11, pp. 889-894, 2003/04/21 2003.
- [41] M. A. Choma, M. V. Sarunic, C. H. Yang, and J. A. Izatt, "Sensitivity advantage of swept source and Fourier domain optical coherence tomography," *Optics Express*, vol. 11, pp. 2183-2189, SEP 8 2003.
- [42] J. F. de Boer, B. Cense, B. H. Park, M. C. Pierce, G. J. Tearney, and B. E. Bouma, "Improved signal-to-noise ratio in spectral-domain compared with time-domain optical coherence tomography," *Optics Letters*, vol. 28, pp. 2067-2069, Nov 1 2003.
- [43] M. Wojtkowski, R. Leitgeb, A. Kowalczyk, T. Bajraszewski, and A. F. Fercher, "In vivo human retinal imaging by Fourier domain optical coherence tomography," *Journal of Biomedical Optics*, vol. 7, pp. 457-463, 2002/07/ 2002.
- [44] M. Wojtkowski, T. Bajraszewski, P. Targowski, and A. Kowalczyk, "Real-time in vivo imaging by high-speed spectral optical coherence tomography," *Optics Letters*, vol. 28, pp. 1745-1747, 2003/10/01 2003.

- [45] M. Wojtkowski, T. Bajraszewski, I. Gorczynska, P. Targowski, A. Kowalczyk, W. Wasilewski, and C. Radzewicz, "Ophthalmic imaging by spectral optical coherence tomography," *Am J Ophthalmol*, vol. 138, pp. 412-9, Sep 2004.
- [46] S. R. Chinn, E. A. Swanson, and J. G. Fujimoto, "Optical coherence tomography using a frequency-tunable optical source," *Optics Letters*, vol. 22, pp. 340-2, 1997/03/01 1997.
- [47] B. Golubovic, B. E. Bouma, G. J. Tearney, and J. G. Fujimoto, "Optical frequency-domain reflectometry using rapid wavelength tuning of a Cr⁴⁺:forsterite laser," *Optics Letters*, vol. 22, pp. 1704-1706, Nov 15 1997.
- [48] S. H. Yun, C. Boudoux, M. C. Pierce, J. F. de Boer, G. J. Tearney, and B. E. Bouma, "Extended-cavity semiconductor wavelength-swept laser for biomedical imaging," *IEEE Photonics Technology Letters*, vol. 16, pp. 293-5, 2004/01/ 2004.
- [49] S. H. Yun, C. Boudoux, G. J. Tearney, and B. E. Bouma, "High-speed wavelength-swept semiconductor laser with a polygon-scanner-based wavelength filter," *Optics Letters*, vol. 28, pp. 1981-1983, OCT 15 2003.
- [50] N. A. Nassif, B. Cense, B. H. Park, M. C. Pierce, S. H. Yun, B. E. Bouma, G. J. Tearney, T. C. Chen, and J. F. de Boer, "In vivo high-resolution video-rate spectral-domain optical coherence tomography of the human retina and optic nerve," *Optics Express*, vol. 12, 2004/02/09 2004.
- [51] R. Leitgeb, M. Wojtkowski, A. Kowalczyk, C. K. Hitzenberger, M. Sticker, and A. F. Fercher, "Spectral measurement of absorption by spectroscopic frequency-domain optical coherence tomography," *Optics Letters*, vol. 25, pp. 820-2, 2000/06/01 2000.
- [52] B. R. White, M. C. Pierce, N. Nassif, B. Cense, B. H. Park, G. J. Tearney, B. E. Bouma, T. C. Chen, and J. F. de Boer, "In vivo dynamic human retinal blood flow imaging using ultra-high-speed spectral domain optical Doppler tomography," *Optics Express*, vol. 11, pp. 3490-3497, DEC 15 2003.
- [53] R. A. Leitgeb, L. Schmetterer, W. Drexler, A. F. Fercher, R. J. Zawadzki, and T. Bajraszewski, "Real-time assessment of retinal blood flow with ultrafast acquisition by color Doppler Fourier domain optical coherence tomography," *Optics Express*, vol. 11, pp. 3116-3121, NOV 17 2003.
- [54] M. Wojtkowski, A. Kowalczyk, R. Leitgeb, and A. F. Fercher, "Full range complex spectral optical coherence tomography technique in eye imaging," *Optics Letters*, vol. 27, pp. 1415-17, 2002/08/15 2002.
- [55] P. Targowski, M. Wojtkowski, A. Kowalczyk, T. Bajraszewski, M. Szkulmowski, and W. Gorczynska, "Complex spectral OCT in human eye imaging in vivo," *Optics Communications*, vol. 229, pp. 79-84, JAN 2 2004.
- [56] M. Wojtkowski, A. Kowalczyk, P. Targowski, and I. Gorczynska, "Frequency domain optical coherence tomography techniques in eye imaging," *Acta Physica Polonica A*, vol. 102, pp. 739-46, 2002/12/ 2002.
- [57] S. H. Yun, G. J. Tearney, B. E. Bouma, B. H. Park, and J. F. de Boer, "High-speed spectral-domain optical coherence tomography at 1.3 μ m wavelength," *Optics Express*, vol. 11, pp. 3598-3604, DEC 29 2003.
- [58] S. H. Yun, G. J. Tearney, J. F. de Boer, N. Iftimia, and B. E. Bouma, "High-speed optical frequency-domain imaging," *Optics Express*, vol. 11, pp. 2953-2963, Nov 3 2003.
- [59] M. A. Choma, K. Hsu, and J. Izatt, "Swept source optical coherence tomography using an all-fiber 1300-nm ring laser source," *Journal of Biomedical Optics*, vol. 10, p. #044009, 2005.

- [60] R. Huber, M. Wojtkowski, K. Taira, J. G. Fujimoto, and K. Hsu, "Amplified, frequency swept lasers for frequency domain reflectometry and OCT imaging: design and scaling principles," *Optics Express*, vol. 13, pp. 3513-3528, 2005.
- [61] J. Zhang and Z. P. Chen, "In vivo blood flow imaging by a swept laser source based Fourier domain optical Doppler tomography," *Optics Express*, vol. 13, pp. 7449-7457, Sep 19 2005.
- [62] R. Huber, M. Wojtkowski, J. G. Fujimoto, J. Y. Jiang, and A. E. Cable, "Three-dimensional and C-mode OCT imaging with a compact, frequency swept laser source at 1300 nm," *Optics Express*, vol. 13, pp. 10523-10538, Dec 22 2005.
- [63] Y. Yasuno, V. D. Madjarova, S. Makita, M. Akiba, A. Morosawa, C. Chong, T. Sakai, K. P. Chan, M. Itoh, and T. Yatagai, "Three-dimensional and high-speed swept-source optical coherence tomography for in vivo investigation of human anterior eye segments," *Optics Express*, vol. 13, pp. 10652-10664, Dec 22 2005.
- [64] W. Y. Oh, S. H. Yun, B. J. Vakoc, G. J. Tearney, and B. E. Bouma, "Ultrahigh-speed optical frequency domain imaging and application to laser ablation monitoring," *Applied Physics Letters*, vol. 88, p. no.103902, Mar 6 2006.
- [65] M. A. Choma, C. H. Yang, and J. A. Izatt, "Instantaneous quadrature low-coherence interferometry with 3 x 3 fiber-optic couplers," *Optics Letters*, vol. 28, pp. 2162-2164, NOV 15 2003.
- [66] J. Zhang, W. Jung, J. S. Nelson, and Z. Chen, "Full range polarization-sensitive Fourier domain optical coherence tomography," *Optics Express*, vol. 12, pp. 6033-6039, 2004/11/29 2004.
- [67] R. Huber, M. Wojtkowski, and J. G. Fujimoto, "Fourier Domain Mode Locking (FDML): A new laser operating regime and applications for optical coherence tomography," *Optics Express*, vol. 14, pp. 3225-3237, Apr 17 2006.
- [68] R. Huber, K. Taira, M. Wojtkowski, and J. G. Fujimoto, "Fourier Domain Mode Locked Lasers for OCT imaging at up to 290kHz sweep rates," in *Optical Coherence Tomography and Coherence Techniques II*, Munich, Germany, 2005, pp. 245-250.
- [69] R. A. Leitgeb, W. Drexler, A. Unterhuber, B. Hermann, T. Bajraszewski, T. Le, A. Stingl, and A. F. Fercher, "Ultrahigh resolution Fourier domain optical coherence tomography," *Optics Express*, vol. 12, pp. 2156-2165, MAY 17 2004.
- [70] M. Wojtkowski, V. J. Srinivasan, T. H. Ko, J. G. Fujimoto, A. Kowalevich, and J. S. Duker, "Ultrahigh resolution, high speed, Fourier domain optical coherence tomography and methods for dispersion compensation," *Optics Express*, vol. 12, pp. 2404-2422, May 2004 2004.
- [71] M. Wojtkowski, V. Srinivasan, J. G. Fujimoto, T. Ko, J. S. Schuman, A. Kowalczyk, and J. S. Duker, "Three-dimensional retinal imaging with high-speed ultrahigh-resolution optical coherence tomography," *Ophthalmology*, vol. 112, pp. 1734-46, Oct 2005.
- [72] T. H. Ko, J. G. Fujimoto, J. S. Schuman, L. A. Paunescu, A. M. Kowalevich, I. Hartl, W. Drexler, G. Wollstein, H. Ishikawa, and J. S. Duker, "Comparison of Ultrahigh- and Standard-Resolution Optical Coherence Tomography for Imaging Macular Pathology," *Ophthalmology*, Sep 22 2005.
- [73] M. Wojtkowski, P. I. Lapin, D. S. Mamedov, J. G. Fujimoto, and S. D. Yakubovich, "Multichannel extremely broadband near-IR radiation sources for optical coherence tomography," *Quantum Electronics*, vol. 35, pp. 667-9, 2005.

- [74] M. R. Hee, C. A. Puliafito, J. S. Duker, E. Reichel, J. G. Coker, J. R. Wilkins, J. S. Schuman, E. A. Swanson, and J. G. Fujimoto, "Topography of diabetic macular edema with optical coherence tomography," *Ophthalmology*, vol. 105, pp. 360-370, Feb 1998.
- [75] A. J. Witkin, T. H. Ko, J. G. Fujimoto, J. S. Schuman, C. R. Bauman, A. H. Rogers, E. Reichel, and J. S. Duker, "Redefining lamellar holes and the vitreomacular interface: An ultrahigh-resolution optical coherence tomography study," *Ophthalmology*, vol. 113, pp. 388-397, Mar 2006.
- [76] T. H. Ko, A. J. Witkin, J. G. Fujimoto, A. Chan, A. H. Rogers, C. R. Bauman, J. S. Schuman, W. Drexler, E. Reichel, and J. S. Duker, "Ultrahigh-resolution optical coherence tomography of surgically closed macular holes," *Archives of Ophthalmology*, vol. 124, pp. 827-836, Jun 2006.
- [77] C. Scholda, M. Wirtitsch, B. Hermann, A. Unterhuber, E. Ergun, H. Sattmann, T. H. Ko, J. G. Fujimoto, A. F. Fercher, M. Stur, and W. Drexler, "Imaging of Macular Holes with Ultrahigh Resolution Optical Coherence Tomography," *Retina*, forthcoming.
- [78] V. J. Srinivasan, M. Wojtkowski, A. J. Witkin, T. Ko, M. Carvalho, J. S. Schuman, A. Kowalczyk, J. S. Duker, and J. G. Fujimoto, "High-definition and three-dimensional imaging of macular pathologies with high-speed, ultrahigh resolution optical coherence tomography," *Ophthalmology*, submitted.
- [79] A. J. Witkin, M. Wojtkowski, V. J. Srinivasan, M. Carvalho, J. S. Schuman, J. S. Duker, and J. G. Fujimoto, "Volumetric rendering of intraretinal features and macular pathology with high-speed ultrahigh resolution optical coherence tomography," *Retina*, submitted.
- [80] G. Wollstein, L. A. Paunescu, T. H. Ko, J. G. Fujimoto, A. Kowalewicz, I. Hartl, S. Beaton, H. Ishikawa, C. Mattox, O. Singh, J. Duker, W. Drexler, and J. S. Schuman, "Ultrahigh-resolution optical coherence tomography in glaucoma," *Ophthalmology*, vol. 112, pp. 229-37, Feb 2005.
- [81] G. Wollstein, J. S. Schuman, L. L. Price, A. Aydin, P. C. Stark, E. Hertzmark, E. Lai, H. Ishikawa, C. Mattox, J. G. Fujimoto, and L. A. Paunescu, "Optical coherence tomography longitudinal evaluation of retinal nerve fiber layer thickness in glaucoma," *Arch Ophthalmol*, vol. 123, pp. 464-70, Apr 2005.
- [82] H. Ishikawa, D. M. Stein, G. Wollstein, S. Beaton, J. G. Fujimoto, and J. S. Schuman, "Macular segmentation with optical coherence tomography," *Invest Ophthalmol Vis Sci*, vol. 46, pp. 2012-7, Jun 2005.
- [83] M. Y. Kahook, R. J. Noecker, H. Ishikawa, G. Wollstein, L. Kagemann, M. Wojtkowski, J. G. Fujimoto, and J. S. Schuman, "Peripapillary schisis in glaucoma patients with narrow angles and elevated intraocular pressure," *Ophthalmology*, submitted.
- [84] C. G. Pieroni, A. J. Witkin, T. H. Ko, J. G. Fujimoto, A. Chan, J. S. Schuman, H. Ishikawa, E. Reichel, and J. S. Duker, "Ultrahigh resolution optical coherence tomography in non-exudative age related macular degeneration," *British Journal of Ophthalmology*, vol. 90, pp. 191-197, Feb 2006.
- [85] M. G. Wirtitsch, E. Ergun, B. Hermann, A. Unterhuber, M. Stur, C. Scholda, H. Sattmann, T. H. Ko, J. G. Fujimoto, and W. Drexler, "Ultrahigh resolution optical coherence tomography in macular dystrophy," *American Journal of Ophthalmology*, vol. 140, pp. 976-983, Dec 2005.
- [86] B. K. Monson, M. Wojtkowski, V. J. Srinivasan, T. Ko, J. S. Schuman, J. G. Fujimoto, and J. S. Duker, "Ultrahigh resolution optical coherence tomography of adult vitelliform macular dystrophy," *Ophthalmology*, submitted.

- [87] T. A. Scheufole, A. J. Witkin, L. S. Schocket, A. H. Rogers, J. S. Schuman, T. H. Ko, J. G. Fujimoto, E. Reichel, and J. S. Duker, "Photoreceptor atrophy in acute posterior multifocal placoid pigment epitheliopathy demonstrated by optical coherence tomography," *Retina*, vol. 25, pp. 1109-1112, 2005.
- [88] L. S. Schocket, A. J. Witkin, J. G. Fujimoto, T. H. Ko, J. S. Schuman, A. H. Rogers, C. Bauman, E. Reichel, and J. S. Duker, "Ultrahigh-resolution optical coherence tomography in patients with decreased visual acuity after retinal detachment repair," *Ophthalmology*, vol. 113, pp. 666-672, Apr 2006.
- [89] A. J. Witkin, M. Wojtkowski, E. Reichel, V. J. Srinivasan, J. G. Fujimoto, J. S. Schuman, and J. S. Duker, "Photoreceptor disruption secondary to posterior vitreous detachment as visualized with optical coherence tomography," *Arch. Ophthalmol.*, submitted.
- [90] A. J. Witkin, T. Ko, J. G. Fujimoto, A. Chan, W. Drexler, J. S. Schuman, E. Reichel, and J. S. Duker, "Ultrahigh-resolution optical coherence tomography assessment of photoreceptors in retinis pigmentosa and related diseases," *American Journal of Ophthalmology*, forthcoming.
- [91] A. Chan, J. S. Duker, T. H. Ko, J. G. Fujimoto, and J. S. Schuman, "Normal macular thickness measurements in healthy eyes using stratus optical coherence tomography," *Archives of Ophthalmology*, vol. 124, pp. 193-198, Feb 2006.
- [92] H. Ishikawa, G. Wollstein, L. A. Paunescu, S. Beaton, J. G. Fujimoto, and J. S. Schuman, "Detailed retinal layer segmentation with optical coherence tomography: A pilot study," *Ophthalmology*, submitted.
- [93] A. Grinvald, R. D. Frostig, E. Lieke, and R. Hildesheim, "Optical Imaging of Neuronal Activity," *Physiological Reviews*, vol. 68, pp. 1285-1366, Oct 1988.
- [94] A. Villringer and B. Chance, "Non-invasive optical spectroscopy and imaging of human brain function," *Trends in Neurosciences*, vol. 20, pp. 435-442, Oct 1997.
- [95] D. Y. Tso, H. Li, Y. Kwon, R. Koardon, P. Truit, and P. Soliz, "Intrinsic Signal Optical Imaging of Retinal Response to Patterned Stimuli," *presented at Association for Research in Vision and Ophthalmology, Fort Lauderdale, FL*, 2003.
- [96] K. Tsunoda, Y. Oguchi, G. Hanazono, and M. Tanifuji, "Mapping cone- and rod-induced retinal responsiveness in macaque retina by optical imaging," *Invest Ophthalmol Vis Sci*, vol. 45, pp. 3820-6, Oct 2004.
- [97] M. Lazebnik, D. L. Marks, K. Potgieter, R. Gillette, and S. A. Boppart, "Functional optical coherence tomography for detecting neural activity through scattering changes," *Optics Letters*, vol. 28, pp. 1218-20, 2003/07/15 2003.
- [98] R. U. Maheswari, H. Takaoka, R. Homma, H. Kadono, and M. Tanifuji, "Implementation of optical coherence tomography (OCT) in visualization of functional structures of cat visual cortex," *Optics Communications*, vol. 202, pp. 47-54, 2002/02/01 2002.
- [99] R. U. Maheswari, H. Takaoka, H. Kadono, R. Homma, and M. Tanifuji, "Novel functional imaging technique from brain surface with optical coherence tomography enabling visualization of depth resolved functional structure in vivo," *Journal of neuroscience methods*, vol. 124, pp. 83-92, Mar 30 2003.
- [100] X. C. Yao, A. Yamauchi, B. Perry, and J. S. George, "Rapid optical coherence tomography and recording functional scattering changes from activated frog retina," *Appl. Opt.*, vol. 44, pp. 2019-2023, Apr 10 2005.
- [101] K. Bizheva, R. Pflug, B. Hermann, B. Povazay, H. Sattmann, P. Qiu, E. Anger, H. Reitsamer, S. Popov, J. R. Taylor, A. Unterhuber, P. Ahnelt, and W. Drexler,

- "Optophysiology: depth-resolved probing of retinal physiology with functional ultrahigh-resolution optical coherence tomography," *Proc Natl Acad Sci U S A*, vol. 103, pp. 5066-71, Mar 28 2006.
- [102] J. M. Schmitt, "Optical coherence tomography (OCT): a review," *IEEE Journal of Selected Topics in Quantum Electronics*, vol. 5, pp. 1205-15, 1999/07/ 1999.
 - [103] A. M. Sergeev, V. M. Gelikonov, G. V. Gelikonov, F. I. Feldchtein, R. V. Kuranov, N. D. Gladkova, N. M. Shakhova, L. B. Suopova, A. V. Shakhov, I. A. Kuznetzova, A. N. Denisenko, V. V. Pochinko, Y. P. Chumakov, and O. S. Streltzova, "In vivo endoscopic OCT imaging of precancer and cancer states of human mucosa," *Optics Express*, vol. 1, 1997/12/22 1997.
 - [104] B. E. Bouma, G. J. Tearney, C. C. Compton, and N. S. Nishioka, "High-resolution imaging of the human esophagus and stomach in vivo using optical coherence tomography," *Gastrointestinal endoscopy*, vol. 51(4) Pt 1, pp. 467-74, Apr 2000.
 - [105] M. V. Sivak, Jr., K. Kobayashi, J. A. Izatt, A. M. Rollins, R. Ung-Runyawee, A. Chak, R. C. Wong, G. A. Isenberg, and J. Willis, "High-resolution endoscopic imaging of the GI tract using optical coherence tomography," *Gastrointestinal endoscopy*, vol. 51(4) Pt 1, pp. 474-9, Apr 2000.
 - [106] S. Jäckle, N. Gladkova, F. Feldchtein, A. Terentieva, B. Brand, G. Gelikonov, V. Gelikonov, A. Sergeev, A. Fritscher-Ravens, J. Freund, U. Seitz, S. Schröder, and N. Soehendra, "In vivo endoscopic optical coherence tomography of esophagitis, Barrett's esophagus, and adenocarcinoma of the esophagus," *Endoscopy*, vol. 32, pp. 750-5, Oct 2000.
 - [107] S. Jäckle, N. Gladkova, F. Feldchtein, A. Terentieva, B. Brand, G. Gelikonov, V. Gelikonov, A. Sergeev, A. Fritscher-Ravens, J. Freund, U. Seitz, S. Soehendra, and N. Schröder, "In vivo endoscopic optical coherence tomography of the human gastrointestinal tract--toward optical biopsy," *Endoscopy*, vol. 32, pp. 743-9, Oct 2000.
 - [108] S. Brand, J. M. Poneros, B. E. Bouma, G. J. Tearney, C. C. Compton, and N. S. Nishioka, "Optical coherence tomography in the gastrointestinal tract," *Endoscopy*, vol. 32, pp. 796-803, Oct 2000.
 - [109] X. D. Li, S. A. Boppart, J. Van Dam, H. Mashimo, M. Mutinga, W. Drexler, M. Klein, C. Pitris, M. L. Krinsky, M. E. Brezinski, and J. G. Fujimoto, "Optical coherence tomography: advanced technology for the endoscopic imaging of Barrett's esophagus," *Endoscopy*, vol. 32, pp. 921-30, Dec 2000.
 - [110] G. Zuccaro, N. Gladkova, J. Vargo, F. Feldchtein, E. Zagaynova, D. Conwell, G. Falk, J. Goldblum, J. Dumot, J. Ponsky, G. Gelikonov, B. Davros, E. Donchenko, and J. Richter, "Optical coherence tomography of the esophagus and proximal stomach in health and disease," *The American journal of gastroenterology*, vol. 96, pp. 2633-9, Sep 2001.
 - [111] B. Shen, G. Zuccaro, Jr., T. L. Gramlich, N. Gladkova, P. Trolli, M. Kareta, C. P. Delaney, J. T. Connor, B. A. Lashner, C. L. Bevins, F. Feldchtein, F. H. Remzi, M. L. Bambrick, and V. W. Fazio, "In vivo colonoscopic optical coherence tomography for transmural inflammation in inflammatory bowel disease," *Clin Gastroenterol Hepatol*, vol. 2, pp. 1080-7, Dec 2004.
 - [112] U. Seitz, J. Freund, S. Jäckle, F. Feldchtein, S. Bohnacker, F. Thonke, N. Gladkova, B. Brand, S. Schröder, and N. Soehendra, "First in vivo optical coherence tomography in the human bile duct," *Endoscopy*, vol. 33, pp. 1018-21, Dec 2001.

- [113] J. M. Ponomarev, G. J. Tearney, M. Shishkov, P. B. Kelsey, G. Y. Lauwers, N. S. Nishioka, and B. E. Bouma, "Optical coherence tomography of the biliary tree during ERCP," *Gastrointestinal endoscopy*, vol. 55, pp. 84-8, Jan 2002.
- [114] V. X. Yang, S. J. Tang, M. L. Gordon, B. Qi, G. Gardiner, M. Cirocco, P. Kortan, G. B. Haber, G. Kandel, I. A. Vitkin, B. C. Wilson, and N. E. Marcon, "Endoscopic Doppler optical coherence tomography in the human GI tract: initial experience," *Gastrointest Endosc*, vol. 61, pp. 879-90, Jun 2005.
- [115] J. M. Ponomarev, S. Brand, B. E. Bouma, G. J. Tearney, C. C. Compton, and N. S. Nishioka, "Diagnosis of specialized intestinal metaplasia by optical coherence tomography," *Gastroenterology*, vol. 120, pp. 7-12, Jan 2001.
- [116] P. R. Pfau, M. V. Sivak, Jr., A. Chak, M. Kinnard, R. C. Wong, G. A. Isenberg, J. A. Izatt, A. Rollins, and V. Westphal, "Criteria for the diagnosis of dysplasia by endoscopic optical coherence tomography," *Gastrointest Endosc*, vol. 58, pp. 196-202, Aug 2003.
- [117] J. A. Evans, J. M. Ponomarev, B. E. Bouma, J. Bressner, E. F. Halpern, M. Shishkov, G. Y. Lauwers, M. Mino-Kenudson, N. S. Nishioka, and G. J. Tearney, "Optical coherence tomography to identify intramucosal carcinoma and high-grade dysplasia in Barrett's esophagus," *Clinical Gastroenterology and Hepatology*, vol. 4, pp. 38-43, Jan 2006.
- [118] G. Isenberg, M. V. Sivak, A. Chak, R. C. K. Wong, J. E. Willis, B. Wolf, D. Y. Rowland, A. Das, and A. Rollins, "Accuracy of endoscopic optical coherence tomography in the detection of dysplasia in Barrett's esophagus: a prospective, double-blinded study," *Gastrointestinal Endoscopy*, vol. 62, pp. 825-831, Dec 2005.
- [119] K. W. Gossage, T. S. Tkaczyk, J. J. Rodriguez, and J. K. Barton, "Texture analysis of optical coherence tomography images: feasibility for tissue classification," *Journal of Biomedical Optics*, vol. 8, pp. 570-5, 2003/07/ 2003.
- [120] X. Qi, M. V. Sivak, D. L. Wilson, and A. M. Rollins, "Computer aided diagnosis (CAD) of dysplasia in Barrett's esophagus (BE) using endoscopic optical coherence tomography (EOCT)," *Gastroenterology*, vol. 126, pp. A351-A351, APR 2004.
- [121] D. Harwood, T. Ojala, M. Pietikainen, S. Kelman, and L. Davis, "Texture Classification by Center-Symmetrical Autocorrelation, Using Kullback Discrimination of Distributions," *Pattern Recognition Letters*, vol. 16, pp. 1-10, Jan 1995.
- [122] J. A. Izatt, M. R. Hee, G. M. Owen, E. A. Swanson, and J. G. Fujimoto, "Optical coherence microscopy in scattering media," *Optics Letters*, vol. 19, pp. 590-2, 1994/04/15 1994.
- [123] J. A. Izatt, M. D. Kulkarni, H.-W. Wang, K. Kobayashi, and M. V. Sivak, Jr., "Optical coherence tomography and microscopy in gastrointestinal tissues," *IEEE Journal of Selected Topics in Quantum Electronics*, vol. 2, pp. 1017-28, 1996/12/ 1996.
- [124] A. D. Aguirre, P. Hsiung, T. H. Ko, I. Hartl, and J. G. Fujimoto, "High-resolution optical coherence microscopy for high-speed, in vivo cellular imaging," *Optics Letters*, vol. 28, pp. 2064-6, 2003/11/01 2003.
- [125] J. T. W. Yeow, V. X. D. Yang, A. Chahwan, M. L. Gordon, B. Qi, I. A. Vitkin, B. C. Wilson, and A. A. Goldenberg, "Micromachined 2-D scanner for 3-D optical coherence tomography," *Sensors and Actuators a-Physical*, vol. 117, pp. 331-340, JAN 14 2005.
- [126] A. Jain, A. Kopa, Y. T. Pan, G. K. Fedder, and H. K. Xie, "A two-axis electrothermal micromirror for endoscopic optical coherence tomography," *Ieee Journal of Selected Topics in Quantum Electronics*, vol. 10, pp. 636-642, MAY-JUN 2004.

- [127] X. Liu, M. J. Cobb, and Y. Chen, "Rapid-scanning forward-imaging miniature endoscope for real-time optical coherence tomography," *Optics Letters*, vol. 29, pp. 1763-5, 2004/08/01 2004.
- [128] A. Dubois, G. Moneron, K. Grieve, and A. C. Boccara, "Three-dimensional cellular-level imaging using full-field optical coherence tomography," *Phys Med Biol*, vol. 49, pp. 1227-34, Apr 7 2004.
- [129] A. Dubois, L. Vabre, A.-C. Boccara, and E. Beaurepaire, "High-resolution full-field optical coherence tomography with a Linnik microscope," *Applied Optics*, vol. 41, pp. 805-12, 2002/02/01 2002.
- [130] L. Vabre, A. Dubois, and A. C. Boccara, "Thermal-light full-field optical coherence tomography," *Optics Letters*, vol. 27, pp. 530-2, 2002/04/01 2002.
- [131] B. Laude, A. De Martino, B. Drevillon, L. Benattar, and L. Schwartz, "Full-field optical coherence tomography with thermal light," *Applied Optics*, vol. 41, pp. 6637-45, 2002/11/01 2002.
- [132] Y. Watanabe, Y. Hayasaka, M. Sato, and N. Tanno, "Full-field optical coherence tomography by achromatic phase shifting with a rotating polarizer," *Applied Optics*, vol. 44, pp. 1387-92, 2005/03/10 2005.
- [133] K. Grieve, G. Moneron, A. Dubois, J.-F. Le Gargasson, and C. Boccara, "Ultrahigh resolution ex vivo ocular imaging using ultrashort acquisition time en face optical coherence tomography," *Journal of Optics A: Pure and Applied Optics*, vol. 7, pp. 368-73, 2005/08/ 2005.
- [134] G. Moneron, A. C. Boccara, and A. Dubois, "Stroboscopic ultrahigh-resolution full-field optical coherence tomography," *Optics Letters*, vol. 30, pp. 1351-3, 2005/06/01 2005.
- [135] A. Dubois, K. Grieve, G. Moneron, R. Lecaque, L. Vabre, and C. Boccara, "Ultrahigh-resolution full-field optical coherence tomography," *Appl Opt*, vol. 43, pp. 2874-83, May 10 2004.
- [136] H. S. Orbach, L. B. Cohen, and A. Grinvald, "Optical Mapping of Electrical-Activity in Rat Somatosensory and Visual-Cortex," *Journal of Neuroscience*, vol. 5, pp. 1886-1895, 1985.
- [137] A. Devor, I. Ulbert, A. K. Dunn, S. N. Narayanan, S. R. Jones, M. L. Andermann, D. A. Boas, and A. M. Dale, "Coupling of the cortical hemodynamic response to cortical and thalamic neuronal activity," *Proceedings of the National Academy of Sciences of the United States of America*, vol. 102, pp. 3822-3827, Mar 8 2005.
- [138] A. K. Dunn, A. Devor, H. Bolay, M. L. Andermann, M. A. Moskowitz, A. M. Dale, and D. A. Boas, "Simultaneous imaging of total cerebral hemoglobin concentration, oxygenation, and blood flow during functional activation," *Optics Letters*, vol. 28, pp. 28-30, Jan 1 2003.
- [139] E. M. G. Hillman, D. A. Boas, A. M. Dale, and A. K. Dunn, "Laminar optical tomography: Demonstration of millimeter-scale depth-resolved imaging in turbid media," *Optics Letters*, vol. 29, pp. 1650-1652, 2004.
- [140] Y. Satomura, J. Seki, Y. Ooi, T. Yanagida, and A. Seiyama, "In vivo imaging of the rat cerebral microvessels with optical coherence tomography," *Clinical Hemorheology and Microcirculation*, vol. 31, pp. 31-40, 2004.
- [141] J. Seki, Y. Satomura, Y. Ooi, T. Yanagida, and A. Seiyama, "Velocity profiles in the rat cerebral microvessels measured by optical coherence tomography," *Clinical Hemorheology and Microcirculation*, vol. 34, pp. 233-239, 2006.

- [142] Y. Ooi, Y. Satomura, J. Seki, T. Yanagida, and A. Seiyama, "Optical coherence tomography reveals in vivo cortical plasticity of adult mice in response to peripheral neuropathic pain," *Neuroscience Letters*, vol. 397, pp. 35-39, Apr 10 2006.
- [143] C. Fang-Yen, M. C. Chu, H. S. Seung, R. R. Dasari, and M. S. Feld, "Noncontact measurement of nerve displacement during action potential with a dual-beam low-coherence interferometer," *Optics Letters*, vol. 29, pp. 2028-2030, 2004.